A Numerical Investigation on the Influence of Engine Shape and Mixing Processes on Wave Engine Performance

A Thesis
Presented to
The Academic Faculty

by

Robert R. Erickson

In Partial Fulfillment
of the Requirements for the Degree
Doctor of Philosophy

School of Aerospace Engineering
Georgia Institute of Technology
December 2004

A Numerical Investigation on the Influence of Engine Shape and Mixing Processes on Wave Engine Performance

Approved by:

Professor Ben T. Zinn
School of Aerospace Engineering
Georgia Institute of Technology, Adviser

Professor Tim Lieuwen
School of Aerospace Engineering
Georgia Institute of Technology

Professor Jeff Jagoda
School of Aerospace Engineering
Georgia Institute of Technology

Dr. Richard Gaeta
Advanced Transportation and Advanced Systems (ATAS) Laboratory
Georgia Tech Research Institute

Professor Suresh Menon
School of Aerospace Engineering
Georgia Institute of Technology

Date Approved: 16 December 2004

ACKNOWLEDGEMENTS

First of all, I would like to acknowledge my thesis advisor, Ben Zinn, for his continued support of this project. I recognize that under the circumstances, he displayed a large amount of patience and always provided very helpful advice and guidance. I also appreciate his flexibility with my employment situation and his willingness to work with me on all issues, both personal and related to this research. Thanks.

I also would like to acknowledge the assistance and guidance from Tim Lieuwen, Nikos Markopolous, and Yedidia Neumeier towards my initial and continued progress with this work.

Next, I would like to acknowledge Chris Stone for his significant and often time consuming assistance with computational/modeling issues as well as Suresh Menon for computational combustion group resources.

Additionally, I also acknowledge certain graduate students and friends including Nate Weiland, Akiva Sklar, Brian Ritchie, and all of the aerospace combustion lab students and employees for very helpful discussions and time.

Finally, I would like to acknowledge the support of my family and Kelli McNeill. The support from my family began long before I entered graduate school, and I sincerely believe that I would not be the person I am today without the positive influence from both Kelli and my family.

TABLE OF CONTENTS

ACKNOWLEDGEMENTS . . . . . **iii**

LIST OF TABLES . . . . . **vi**

LIST OF FIGURES . . . . . **vii**

SUMMARY . . . . . **xv**

I BACKGROUND AND MOTIVATION **1**

1.1 Pre World War II 2

1.2 World War II and the Luftwaffe 4

1.3 Post War Research and Development 7

1.4 Fundamental Wave Engine Operating Principles 12

II PRELIMINARY DUCT SHAPE INVESTIGATION **18**

2.1 Model Equations 19

2.2 Solution Technique 21

2.3 Trial Functions 22

2.4 Results 24

III WAVE ENGINE MODEL DEVELOPMENT AND NUMERICAL IMPLEMENTATION **36**

3.1 Detailed Wave Engine Operation 37

3.2 Formulation 39

3.2.1 Model Equations 40

3.2.2 Boundary Conditions 41

3.2.3 Mixing Model 44

3.2.4 Heat Release Models 47

3.2.5 Numerical Implementation 48

IV INITIAL NON-REACTING AND REACTING FLOW WAVE ENGINE SIMULATIONS **55**

4.1 Non-Reacting Simulations 56

4.1.1 Closed/Closed Systems 56

4.1.2 Closed/Open Systems 58

4.2 Reacting Flow Results . . . 62
4.2.1 Detailed Chemical Kinetics Simulation Results . . . 63
4.2.2 Comparison of Heat Release Models . . . 71
4.2.3 Simplified Heat Release Model Validation . . . 72
4.3 Calculation of Thrust and Specific Fuel Consumption . . . 78
4.3.1 Thrust Calculation Formulation . . . 78
4.3.2 Positive Exhaust Outflow . . . 80
4.3.3 Backflow . . . 81
4.3.4 Example . . . 81
4.4 Exhaust Boundary Condition Investigation . . . 81

V WAVE ENGINE PERFORMANCE AS A FUNCTION OF INLET VALVE RESISTANCE AND MIXING CHARACTERISTICS . . . 89

5.1 Inlet Valve Resistance . . . 90
5.2 Mixing and Unsteady Heat Release Rates . . . 95
5.2.1 Large Scale Mixing Event Size . . . 97
5.2.2 Small Scale Mixing RMS velocity . . . 101
5.2.3 Turbulent Mixing Event Size . . . 113

VI WAVE ENGINE PERFORMANCE AS A FUNCTION OF ENGINE SHAPE . . . 116

6.1 Tailpipe Diameter . . . 117
6.1.1 Harmonic Content of Unsteady Heat Release Rates and Wave Engine Oscillations . . . 121
6.2 Exhaust Nozzle/Flare Study . . . 133

VII CONCLUSIONS AND RECOMMENDATIONS FOR FUTURE STUDIES . . . 140

7.1 Conclusions . . . 140
7.2 Recommendations for Future Studies . . . 143
7.2.1 Model Improvements . . . 143

REFERENCES . . . 147

VITA . . . 151

LIST OF TABLES

Table 1 Calculation of natural acoustic mode frequencies for straight and horn shaped ducts based on Eq. 21. Assumed sound speed and flare constant of 330m/s and 5.75, respectively. 24

Table 2 Summary of engine performance as a function of inflow resistance in terms of maximum average thrust. The time lag refers to the start of mixing in terms of the fraction of a period after the start of injection of reactants (i.e. the opening of the inlet valves). 92

Table 3 Summary of engine performance as a function of rms velocity of small scale mixing in terms of maximum average thrust. The time lag refers to the start of mixing in terms of the fraction of a period after the start of injection of reactants (i.e. the opening of the inlet valves). 103

Table 4 Amplitudes and phase coefficients for the Fourier reconstruction of the log normal energy addition function using five modes. 126

Table 5 Natural acoustic mode frequencies for the investigated wave engines with spatially uniform mean temperature of 2100K. 131

Table 6 Natural acoustic mode frequencies for the investigated engine geometries with a mean flow of 20 g/s and a non-uniform mean temperature field. . 133

Table 7 Shift of natural acoustic mode frequencies away from harmonics of fundamental corresponding to values in Table 6. 133

LIST OF FIGURES

Figure 1 Karavodine gas turbine combustor. (1908) 3

Figure 2 Marconnet valveless pulsejet design. (1908-09) 3

Figure 3 Argus valveless pulsejet burner. (1940) 5

Figure 4 The first V-1 prototype developed by Argus Aeroengines with Paul Schmidt. (1940) 5

Figure 5 V-1 Thrust as a function of ram pressure. Lettered curves represent design iterations. 6

Figure 6 (a): Schematic of SNECMA Escopette along with particle location vs time figure. (b): Figure from U.S. patent of combined cycle pulsejet ramjet by J. Bertin of SNECMA motors. 8

Figure 7 Schematic of different engine geometries experimentally examined by Logan and co-workers[34]. 9

Figure 8 Specific impulse vs. tailpipe length for methane and propane fuels and combustion chamber diameters of 3.0 in (a) and 3.5 in (b). Taken from [34]. 10

Figure 9 Valveless pulsejet described in Lockwood U.S. patent 3,462,955. 12

Figure 10 (a) Simplified wave engine schematic, and (b) qualitative time dependence of inlet pressure, inlet velocity, and total heat release rate. 14

Figure 11 Large vortex formation as a result of impulsive injection[24].Top row: results from vortex dynamics model. Black indicates reactants. Bottom row: Schlieren data with particle path indicators. Left: Peak of injection. Middle: Onset of reaction. Right: Peak of reaction. 17

Figure 12 Illustration of forced acoustic resontor used in this investigation. 19

Figure 13 Comparison of driven pressure oscillations within straight ducts using the Galerkin method with two other published results. Results from Galerkin method for comparison with Ilinskii et al.[21] data correspond to larger forcing amplitude than that of the Chun and Kim[9] study. 26

Figure 14 (a): Time evolution of pressure at a closed end of a cylindrical duct forced at the fundamental natural frequency starting from rest. (b): Enlarged view of the limit cycle behavior. 27

Figure 15 (a) Time dependence of finite amplitude, limit cycle pressure oscillations driven in a straight duct ($F_0 = 5e-4$, $\Omega = 1.0$, $c_0 = 330m/s$, $\mathcal{L} = 0.165m$), and (b), the corresponding FFT. Duct shape is shown in the upper right portion of (b). Note that the power in the FFT is normalized with respect to the power in the fundamental mode. 28

Figure 16 Frequency dependence of limit cycle pressure oscillations for different forcing amplitudes in a straight duct. 29

Figure 17 Time dependence (a) and frequency content (b) of driven oscillations at the small end of horn shaped duct ($\alpha = 5.75$, $F_0 = 5E-4$, $\Omega = 1.36$, $c_0 = 330m/s$, $\mathcal{L} = 0.224m$). The frequency content in (b) corresponds to the calculations including 20 modes (solid line in (a)). 30

Figure 18 Pressure oscillations excited in straight and horn shaped closed ducts of equal volume using single frequency sinusoidal forcing. 31

Figure 19 Dependence of compression ratio on flare constant for exponential horn shaped acoustic resonators. 32

Figure 20 Pressure oscillations at an end of three different duct shapes motivated by study of Hamilton et al[19]. For duct shapes displayed on the right, the top, middle, and lower ducts correspond to $a_2 = 0$, $a_3 = -0.5$, $a_2 = -0.5$, $a_3 = -0.5$, and $a_2 = -0.5$, $a_3 = 0$, respectively. 34

Figure 21 Illustration of important physical processes occurring each cycle accompanied by axial pressure and velocity profiles. 38

Figure 22 Block inversion of a scalar field with event center located at l_0 and size l. 45

Figure 23 Illustration of two length scale mixing using the LEM model. 46

Figure 24 Temperature dependence of simplified consumption model and Arrhenius fuel consumption rates. 49

Figure 25 Temperature dependence of constant pressure specific heats for major species. 51

Figure 26 Illustration of grid transformation. 54

Figure 27 Piston forced oscillation within a closed 0.3m long straight duct. (a) details three limit cycle oscillations extracted from (b). 57

Figure 28 Piston forced oscillation within a closed 0.5m long straight duct with open pressure release boundary condition. (a) shows detailed limit cycle oscillations extracted from (b). 59

Figure 29 FFT of limit cycle pressure oscillations at the piston face for the straight duct Closed/Open system. 60

Figure 30 Inlet pressure and velocity traces for nonreacting cold flow conditions and several values of the flapper valve parameter ξ. 61

Figure 31 Inlet pressure and velocity for a reacting flow wave engine simulation using a detailed chemical kinetic mechanism. 64

Figure 32 Experimental Schlieren image of large vortex formed during the unsteady injection of premixed reactants into a dump combustor. Taken from Poinsot et al.[42] 65

Figure 33 Pressure time history inside combustor (at 0.25*L) in addition to spatially integrated heat release. 67

Figure 34 Inlet pressure and velocity values for a reacting flow condition. No large scale mixing event included, therefore vertical lines represent start of small scale mixing. 68

Figure 35 Pressure time history inside combustor (at 0.25*L) in addition to spatial integral of heat release in the absence of a large scale mixing event. Decreasing upstream pressure amplitude suggests that unsteady heat release not large enough to overcome damping processes. 70

Figure 36 Comparison of inlet conditions and total instantaneous heat release rate using chemical kinetic model and simplified consumption model. 73

Figure 37 Equilibrium and kinetic carbon monoxide mole fraction as a function of time for a typical spark ignition engine cycle. Taken from Heywood[20] . 74

Figure 38 Spatial heat release distribution from chemical kinetic model and simplified consumption model. 75

Figure 39 Comparison of model results with experimental pulse combustor data reported in Keller et al.[25]. - - - Experimental results; — Model prediction. No acoustic radiation from open exhaust end. $\xi = 2800$. 76

Figure 40 Comparison of model results with experimental pulse combustor data reported in Keller et al.[25]. - - - Experimental results; — Model prediction. 6% acoustic radiation from open exhaust end. $\xi = 2500$. 77

Figure 41 Stationary wave engine with control volume used to calculate thrust. . . . 79

Figure 42 Time dependence of the terms in the instantaneous thrust equation. . . . 82

Figure 43 Illustration of a) ejected combustion products mixing with ambient air and b) backflow of resultant mixture back into wave engine. 83

Figure 44 Schematic of engine geometry used in backflow temperature study. 84

Figure 45 Typical exhaust conditions in terms of velocity, mass flow, and density. Backflow temperature for this case was 550K. 85

Figure 46 Timing sweeps for different backflow temperatures. 86

Figure 47 Maximum thrust and corresponding specific fuel consumption for different bacflow temperatures. 87

Figure 48 Spatial distribution of heat release for three inflow resistance parameters. 91

Figure 49 Dependence of average thrust on time lag for three inflow resistance values. 93

Figure 50 Dependence of average SFC on time lag for three inflow resistance values. 94

Figure 51 Experimental visualization of a vortex ring created by the impulsive injection of water from a tube. Taken from [16]. 96

Figure 52 Wave engine schematic with ineffective large scale mixing event location. 97

Figure 53 Engine geometry and spatial distribution of heat release for different large scale event sizes. 99

Figure 54 Average thrust and SFC vs. time lag from start of injection to start of mixing for three large scale mixing event sizes. Solid lines represent thrust calculations, with scale on the left axis and dashed lines represent SFC, with scale on the right axis. 100

Figure 55 Engine geometry and spatial distribution of heat release within the combustion chamber for three small scale turbulent mixing intensities. 102

Figure 56 Time dependence of total heat release for turbulent rms velocities of 10, 20, and 30 percent of the maximum inlet velocity. 104

Figure 57 Inlet pressure vs. time for rms velocity of 10, 20, and 30 percent of maximum inlet velocity. 105

Figure 58 (a) Velocity in middle of the combustion chamber vs. time for rms velocities of 10, 30, and 50 percent of maximum inlet velocity. (b) Windowed FFT of velocity traces in (a) 106

Figure 59 Average thrust vs. time lag from the start of injection to the start of mixing. 108

Figure 60 Specific fuel consumption vs. time lag from the start of injection to the start of mixing. 109

Figure 61 Sinusoidal flow field oscillation and two heat addition functions with $\sigma = 0.1$ and $\sigma = 0.25$ for five phase values. 111

Figure 62 Dependence of Rayleigh integral on phase between heat addition and flow field oscillation for two log normal heat addition functions, $\sigma = 0.1$ and $\sigma = 0.25$. 112

Figure 63 Average thrust as a function of timing for small scale eddy sizes ranging from five to twenty five percent of the large scale event size. Engine geometry shown in upper right corner(all units meters). 114

Figure 64 Dependence of SFC on time lag for turbulent mixing event sizes of 5-20% of the large scale mixing event size. 115

Figure 65 Configurations of the three investigated wave engines having different tailpipe diameters. Tailpipe cross sectional area of a) is approximately 20% less than combustion chamber, b) is a straight duct, and c) is approximately 20% greater than combustion chamber. 118

Figure 66 Average thrust vs. time lag for three engine shapes featuring different tailpipe diameters. 119

Figure 67 Average SFC vs. time lag for three engine shapes featuring different tailpipe diameters. 120

Figure 68 Time dependence of heat release and corresponding FFT at one location in combustion chamber. 122

Figure 69 Time dependence of pressure and corresponding FFT at one location in the combustion for the straight duct and smaller diameter tailpipe wave engine. The FFT amplitude has been normalized by the amplitude of the fundamental natural acoustic mode, and the vertical axis is truncated in order to improve resolution of harmonic energy content. 123

Figure 70 Comparison of the log normal energy addition function and the Fourier reconstruction of this function using five modes. 125

Figure 71 Frequency response of harmonic (a) and anharmonic (b) systems. Detuning factor, Υ_m, is 1.0 for all modes of harmonic system, and 1.5 for all modes of anharmonic system 127

Figure 72 Time dependent output of harmonic (a) and anharmonic (b) systems. . . 128

Figure 73 Time dependence of pressure and corresponding FFT at one location in the combustion for the straight duct and larger diameter tailpipe wave engine. The FFT amplitude has been normalized by the amplitude of the fundamental natural acoustic mode, and the vertical axis is truncated in order to improve resolution of harmonic energy content. 130

Figure 74 Sectored representation of wave engine. Axial temperature gradients represented by colored sectors; red - hot ($\tilde{2}$000K) through blue - cold($\tilde{3}$00K). 132

Figure 75 Axial mean temperature profile for three engine shapes. 132

Figure 76 Exhaust velocity vs. time for straight engine and larger tailpipe diameter engine. 134

Figure 77 Engine shape with metric dimensions for exhaust nozzle and flare investigation. 136

Figure 78 Dependence of average thrust of the wave engines upon the time lag for three engine shapes featuring a linear flare, straight extension, and linear nozzle shown in Fig. 77. 138

Figure 79 Dependence of average SFC of the wave engines upon the time lag for three engine shapes featuring a linear flare, straight extension, and linear nozzle shown in Fig. 77. 139

LIST OF SYMBOLS

a - dimensional forcing amplitude

$\mathcal{T}$ - Normalized time

$S, \mathcal{A}$ - Normalized cross sectional area

X - Normalized axial distance

x - Dimensional axial distance

u - Dimensional velocity

$\mathcal{L}$ - Dimensional length

A - Dimensional cross sectional area

F - Normalized forcing function

$\mathcal{D}$ - Normalized dissipation parameter

R - Residual function

W - Modal weighting functions

G - Linear oscillator terms (time dependent)

$\mathcal{R}$ - Linear oscillator terms (spatially dependent)

Z - Nonlinear coupling oscillator terms

E - Forcing oscillator terms

P - pressure

$\mathcal{K}$ - Natural acoustic wave number

c - Sound speed

Y - Species mass fraction

T - Temperature

E - Total energy per unit volume

h - Enthalpy of formation

e - Internal energy

c_v - Constant volume specific heat

k - Coefficient of thermal conductivity

D - Species Diffusivity

Pr - Prandtl number

Le - Lewis number

Re - Reynolds number

$\dot{m}'''$ - Reaction rate

l - Block inversion event size

L - Mixing length scale

$\mathbf{U}$ - Conserved variable vector

$\mathbf{F}$ - Flux vector

$\mathfrak{l}$ - Linear second order loss factor

$\mathfrak{K}$ - Linear second order amplitude coefficient

H - Linear second order transfer function

Ang - Linear second order transfer function phase

Greek Symbols

Φ - Normalized velocity potential

Ω - Normalized forcing frequency

ω - Dimensional forcing frequency

γ - Ratio of specific heats

Γ - Normalized forcing term

ζ - Viscous damping oscillator terms

Ξ - Normalized dissipation term

Ψ - Normalized mode shape function

η - Normalized time dependent modal amplitude function

α - Horn flare constant

τ - Viscous stress tensor

ρ - Density

μ - Dynamic viscosity

ς - Sutherland viscosity constant

ξ - Valve resistance parameter

λ - Event frequency per unit length θ - Arbitrary scalar

ν - Kinematic viscosity

κ - Simplified reaction rate constant

φ - Fourth order numerical smoothing constant

Υ - Detuning coefficient

SUMMARY

This thesis describes an investigation of the influence of engine shape and mixing processes on the overall performance of air-breathing wave engines. The first portion of this investigation examines the influence of duct shape on driven oscillations in acoustic compression devices, which represent a simplified physical system closely related in several ways to the wave engine. A numerical model based on an application of the Galerkin method was developed to simulate large amplitude, one-dimensional acoustic waves driven in closed ducts. Results from this portion of the investigation show that gas-dynamic nonlinearities significantly influence the properties of driven oscillations by transferring acoustic energy from the fundamental driven mode into higher harmonic modes. Furthermore, it is shown in this part of the thesis that duct shaping can be used to dramatically decrease the amount of acoustic energy transferred out of the fundamental mode, leading to more continuous waveforms of significantly larger amplitude.

The second portion of the thesis describes the development of an additional numerical model based on the finite differencing of the quasi one-dimensional conservation equations of mass, momentum, energy, and species. This numerical model includes sub-models that simulate mechanical inlet flapper valves, coherent and turbulent mixing processes, and unsteady heat release due to the combustion of premixed reactants. A comparison of simulation results with experimental measurements presented in this section shows the ability of this numerical model to simulate the essential physical processes necessary for wave engine operation.

The third portion of this investigation presents and analyzes results from parametric studies of the characteristics of mixing and engine shape. The two objectives of these studies are to determine the influence of mixing characteristics and engine shape on overall wave engine performance and to develop insight into the physical processes controlling the performance trends. Results show that, given the characteristics of mixing assumed in this

study, the unsteady heat release driving oscillations in the wave engine contains significant harmonic content. It is also shown that the natural acoustic mode frequencies of the wave engine are strong functions of both the engine shape and the mean temperature gradients within the engine. Finally, simulation results show that average thrust generation decreases dramatically when the natural acoustic mode frequencies of the engine and the frequency content of the unsteady heat release are not aligned. Hence, wave engine performance can be significantly improved by aligning the natural acoustic mode frequencies of the engine and the frequency content of the unsteady heat release.

CHAPTER I

BACKGROUND AND MOTIVATION

Wave engines, recognized by many as pulsejets, buzzbombs, resojets, or pulse detonation engines to name a few, are a class of unsteady, air-breathing propulsion systems that use an intermittent combustion process to generate thrust. Initially attracted by the inherently simple mechanical design, scientists and engineers have studied and developed various wave engine designs since the early 20th century[15]. The wave engine operates on a periodic cycle based on large amplitude longitudinal acoustic waves within a chamber. These large amplitude acoustic waves, created and sustained by an intermittent combustion process, control the mass flow through the engine and provide the compression of reactants in the place of complex and expensive compressors necessary for gas turbine propulsion systems. While the potential for very low cost per unit is an important advantage for propulsion system designers concerned with cruise missiles or uninhabited aerial vehicles, relatively poor performance in terms of specific fuel consumption and maximum flight speed have severely limited successful wave engine applications. In spite of the simple geometry of most wave engine designs, the complexity of key physical processes introduce significant challenges toward the development of a thorough understanding of wave engine operation. The objective of this study is to advance the current wave engine knowledge base through a systematic investigation of the influence of engine shape and mixing processes on wave engine performance. Given the potential advantages of the wave engine for certain propulsion applications, the primary motivation for this investigation is to develop a more detailed physical insight into the influence of gas dynamic nonlinearities and unsteady combustion processes in the hope that a more fundamental knowledge of the wave engine cycle will lead to performance improvements in future engine designs.

Pulsejet wave engines have been investigated extensively throughout the world. Furthermore, in contrast with other wave engine concepts, such as the Pulse Detonation Engine

(PDE), the pulsejet wave engine was once built and deployed on a large scale. In fact, over 10,000 pulsejets were manufactured and deployed during World War II by the Germans. A combination of the rise in popularity of the modern gas turbine jet engine and the inability of pulsejet engine designs to meet performance expectations led to a significant decline in interest in the pulsejet engine.

1.1 Pre World War II

Research and development on resonating combustion devices for the generation of power and thrust began in the early 1900's on two separate applications. The first application, by Karavodine in 1908, was a pulsating gas turbine combustor. Figure 1 shows a schematic of the Karavodine, which consisted of a combustion chamber attached to a straight tube with the exhaust pointed into a turbine. Reactants in this combustor were ignited with a spark plug, creating an explosion that raised the overall pressure. The combustion products then exhaust through the turbine blades, and the inertia of the burned gases leaving the combustor decreased the combustion chamber pressure below the inlet pressure. This decrease in pressure opened the inlet valves and a fresh mixture of reactants entered the chamber, and the process was repeated. Unfortunately for Karavodine, this system was very inefficient, creating only 2 h.p with a consumption of 11 pounds of benzene per horsepower-hour[13].

Around the same time (1908-09), another Frenchman named Marconnet was developing a resonating combustion device for the generation of thrust directly from exhaust gases. Figure 2 presents the geometry of the engine as well as the fuel injector and spark ignitor location. Downstream of the fuel injector was a mixing/vaporization region that smoothly transitioned into a larger diameter bulb-like combustion chamber. Downstream of the combustion chamber was the tailpipe section which flared at the exhaust. One notable aspect of the Marconnet engine in contrast with the Karavodine combustor is the lack of mechanical inlet valves, which further increases the simplicity of the design. Although a certain amount of total efficiency may be lost through the exhaust of burnt gases out of the inlet, well designed inlets can act as effective flow rectifying devices, and valveless inlets on pulsejet wave engines have been used extensively throughout their history.

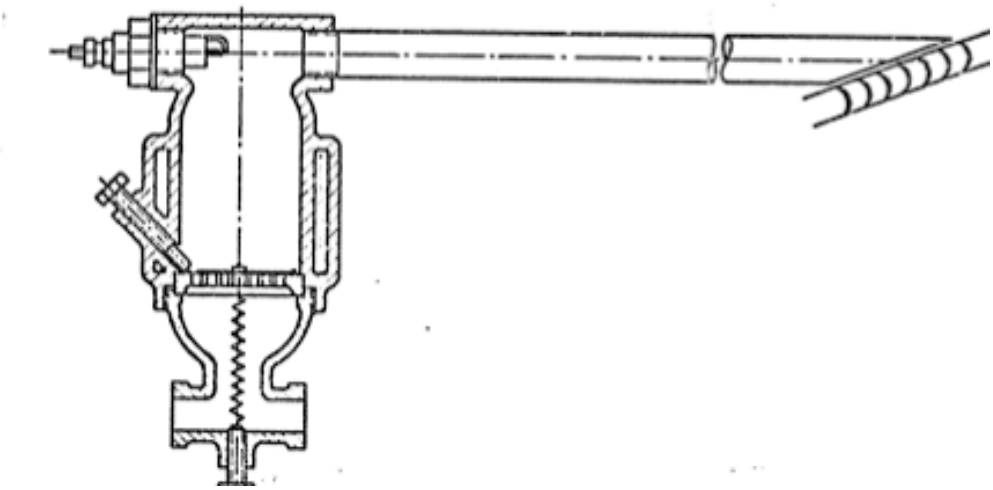

Figure 1: Karavodine gas turbine combustor. (1908)

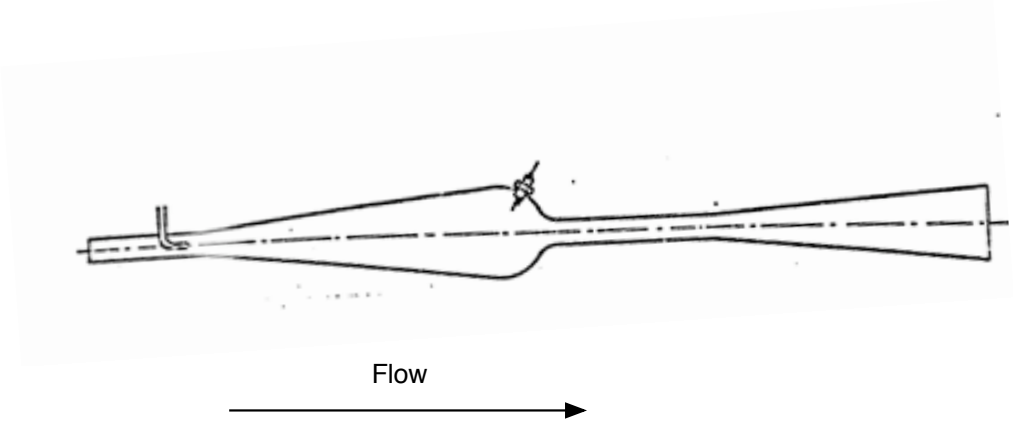

Figure 2: Marconnet valveless pulsejet design. (1908-09)

Later in the 1930's, significant work was completed by Reynst[44] on self-sustained pulsating combustion systems without the use of external ignition sources. The work by Reynst was less application oriented and more concerned with developing an understanding of pulsating combustion phenomena. While the designs discussed above shared the common trait of relatively poor performance, and Reynst never actually designed an engine based on the principles he uncovered, all this work is important to the design of practical pulsejets because of the influence it had on future engine designers in Germany during the Second World War. For example, in a report compiled by A.K. Oppenheim[39] after World War II on the development of pulsejet wave engines by Nazi Germany, Dr. Diedrich, working for the German engine company Argus Aeroengines, submitted a report with a historical outline that discussed this work that eventually shaped much of the pulsejet development program.

1.2 World War II and the Luftwaffe

German interest in the pulsejet as a primary propulsion system increased throughout the late 1930's and early 1940's as a result of both laboratory combustion experiments and fundamental gas dynamic investigations into unsteady flow processes. Hummel and researchers performed a gas dynamic investigation in which a piston was attached to a straight duct that was open to the atmosphere at the exhaust end[39]. This investigation pointed out that positive thrust could be generated merely by oscillating this piston at the resonant frequency of the duct. The reason behind this 'ponderomotoric' effect, as described by Hummel, was that the exhaust flow from the duct behaves as an axial jet while the gases re-entering the duct at the exit plane behave as a sink flow. Furthermore, in 1930, Paul Schmidt patented the basic pulsejet cycle, which he called the impulsive duct[46]. Throughout this time, Schmidt was designing and testing pulsating combustion systems for propulsion applications. Then, in 1940, the Luftfahrtministerium drafted Schmidt to work with Argus Aeroengines, that was also working on this concept[39]. Figure 3 shows an early Argus pulsejet engine that burned gasoline and used a valveless inlet similar to the Marconnet engine discussed above. This engine used a spark ignitor to initiate combustion during

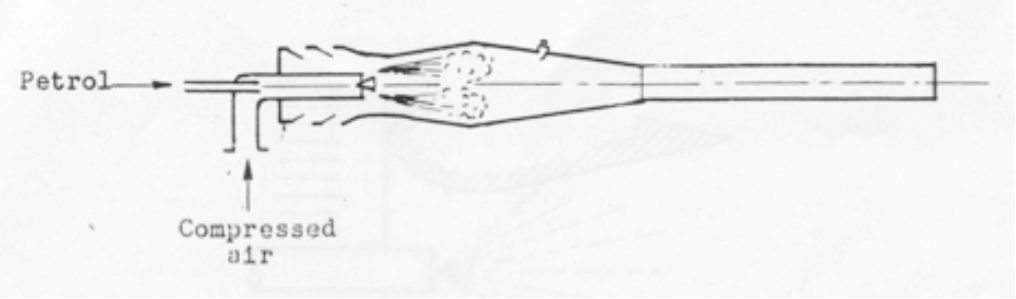

Figure 3: Argus valveless pulsejet burner. (1940)

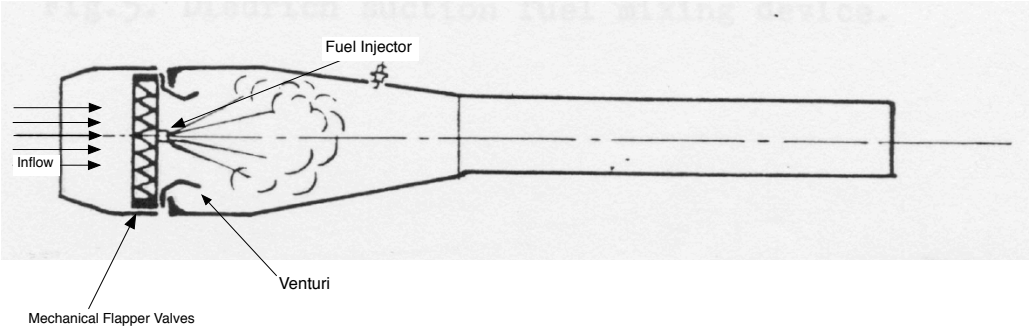

Figure 4: The first V-1 prototype developed by Argus Aeroengines with Paul Schmidt. (1940)

the entire operation although during testing they noticed self ignition of the mixture[18].

In 1940, Argus Aeroengines and Schmidt teamed up to develop a propulsion system, and by 1941, a prototype of the first V-1 was finished. Figure 4 is a schematic of the prototype, whose design did not change drastically throughout the rest of development[39]. Figure 4 shows the mechanical flapper valves at the inlet, as opposed to the valveless concepts developed earlier, and a venturi that accelerated the flow just downstream of the inlet to aid the mixing and vaporization of fuel in the combustion chamber. Initial testing proceeded quickly with this prototype, and the test bed was an automobile, which reached speeds of over sixty miles and hour with the prototype engine strapped to the roof[39]! By the summer of 1941, 'cargo gliders' were propelled solely by these prototype engines, but just as the previous automobile tests, all the flight speeds were relatively low, and nowhere near the design goal of speeds in excess of 700 km/h[18].

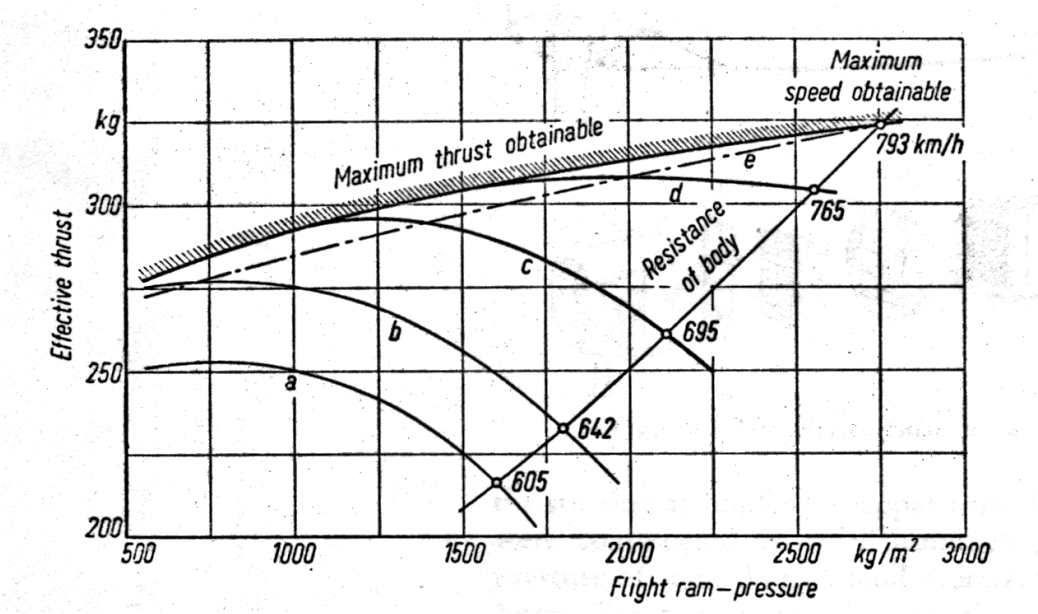

Figure 5: V-1 Thrust as a function of ram pressure. Lettered curves represent design iterations.

The decision was made in 1942 to develop an umanned flying bomb with the pulsejet as the propulsion unit, and the V-1 was born. By the end of initial flight testing, it was quickly realized that the initial designs were not capable of getting close enough to the design speed, and a research program concentrating on fuel control and inlet aerodynamics was started[18, 13]. The major effects present at higher speeds are the increased drag and the increased ram pressure of the air entering the inlet. The production V-1 engine was 3.6 meters long, weighed 138 kg, and produced a sea level thrust of 350 kg with a specific fuel consumption of 0.8g/kg. Figure 5 shows the poor performance of the initial prototypes in terms of effective thrust as a function of RAM pressure resulting from increased flight speeds, with lettered curves representing continuous improvements to the fuel control system and inlet.

Finally, it would be misleading from both an engineering perspective and a historical perspective to omit the significant flaws inherent in the V-1 pulsejet. First of all, the thrust per frontal area of these engines was commonly agreed upon to be rather poor as flight speeds increased[13]. Additionally, one of the most important problems, especially looking forward to future pulsejet designs was the very short valve life of the V-1 inlet. Since these

flying bombs did not have to travel very far, and were only used once, this was not a major problem for the V-1, but it is estimated that the total lifetime of these flapper valves was only 45 minutes of operation. The major difficulty of this aspect of design, which will not be investigated in this study but should be mentioned nonetheless, was the shielding of inlet valves from the high intensity and temperature combustion processes.

1.3 Post War Research and Development

The United States never deployed any pulsejet applications during the war, but it was revealed after the war that Aerojet engine corporation was working on a pulsejet design as early as 1943, and one concept engine was built and tested during this time[13]. Also during 1943, the French aircraft engine company SNECMA also began investigating pulsejet technology because of an interest in developing a propulsion device based on a constant volume combustion process. By 1950, SNECMA had four valveless pulsejets, named escopettes, flying on a manned glider, as shown in Fig. 6 (a)[5]. Figure 6(a) shows that this valveless pulsejet contained an upstream inlet duct that essentially reduced the amount of gas ejected from the inlet during the combustion phase of the cycle, thus decreasing inlet losses. Furthermore, building upon the escopette pulsejet, J. Bertin of SNECMA motors also obtained a U.S. patent for a composite Ramjet-Pulsejet engine[6], as shown in Fig. 6 (b). This engine was to operate in pulsejet mode during low speed flight and transition to ramjet mode as flight speed approached sonic speeds. This design contained cowls (denoted by the number 16 in Fig. 6 (b)) that would close during pulsejet operation and open during ramjet operation. This patent also describes the idea of using thrust ejectors near the exhaust to augment thrust, and these ejectors also contained fuel injection ports for use as an afterburner like device.

In the summer of 1944, the United States recovered the first V-1[13]. Then, starting in the early 1950's, the Office of Naval Research sponsored a large research and development project on wave engines and pulsejets, with over ten different organizations contributing both theoretical and experimental work. This program, named the SQUID project, was motivated mostly from the recovered V-1's, but the applications in mind for this project

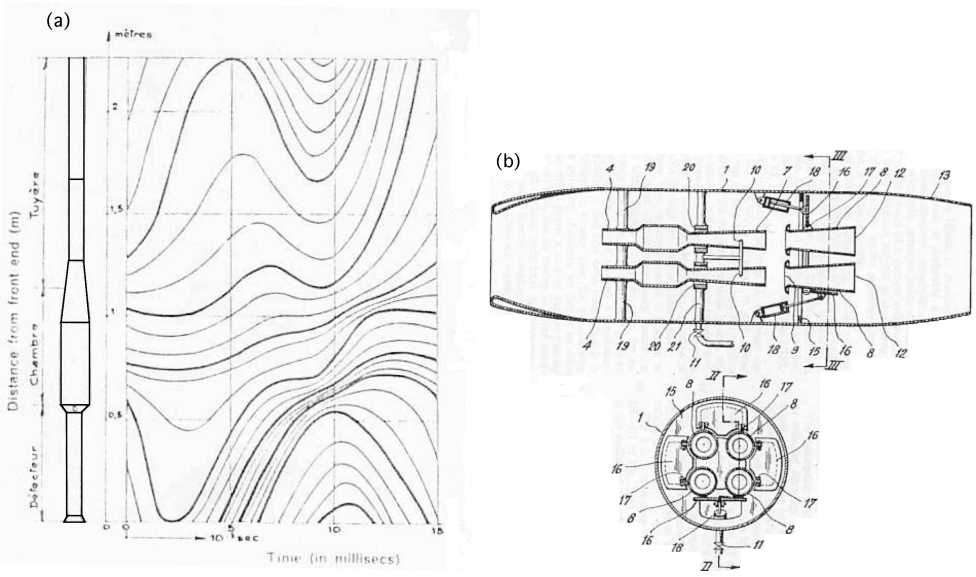

Figure 6: (a): Schematic of SNECMA Escopette along with particle location vs time figure. (b): Figure from U.S. patent of combined cycle pulsejet ramjet by J. Bertin of SNECMA motors.

were more broad than just propulsion units for flying bombs, and eventually included tip mounted helicopter propulsion units. One important contributor to the SQUID project was the Logan group at Cornell University. Logan performed a variety of experiments on an experimental valveless pulsejet including investigations into both engine shape and fuel type. Figure 7 shows the shapes and dimensions of several experimental models. During testing, Logan and workers obtained a maximum specific impulse of 2200 seconds for these pulsejets[34]. A series of experiments with different engine sizes, shapes, and fuels concluded that their test engines were extremely sensitive to small changes in engine size and shape. Figure 8 presents specific impulse measurements from the straight tailpipe engines shown in Fig. 7 using gaseous propane and methane. Further, Fig. 8(a) and (b) present results from combustion chamber diameters of 3.0 and 3.5 inches, respectively. These specific impulse measurements reveal that for all of the engine configurations tested, small changes in tailpipe length often dramatically changed the overall performance. In addition, the results presented in Fig. 8(a) also show that the trend in specific impulse as a function of tailpipe length was different for propane and methane.

Also funded under the SQUID program, Foa and coworkers theoretically investigated

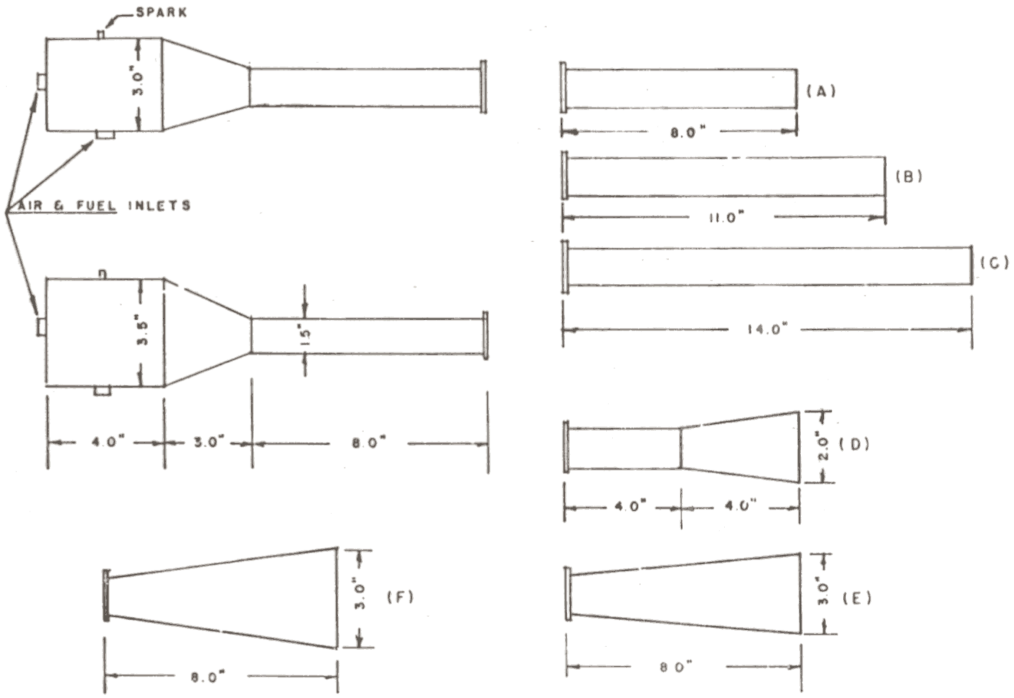

Figure 7: Schematic of different engine geometries experimentally examined by Logan and co-workers[34].

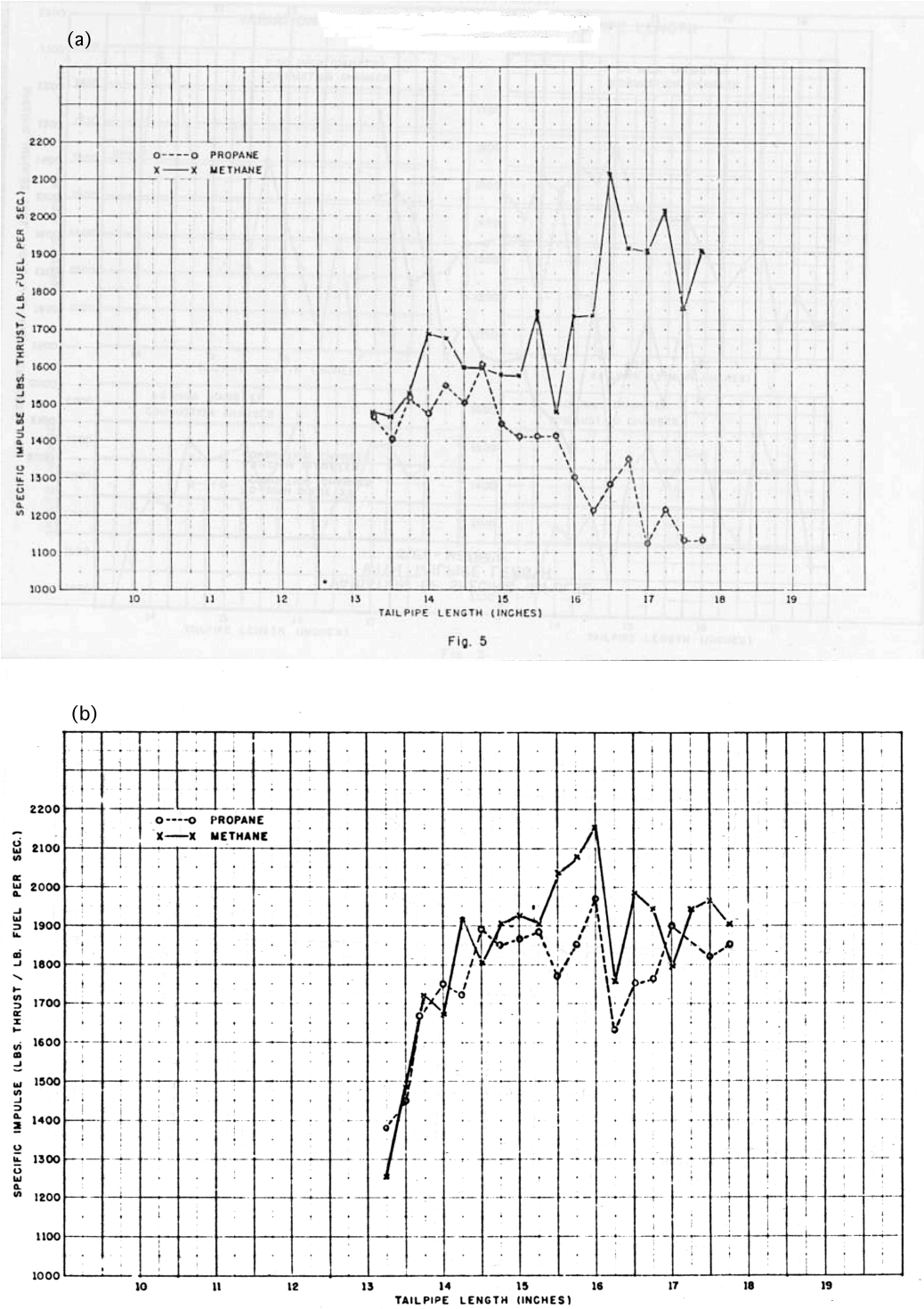

Figure 8: Specific impulse vs. tailpipe length for methane and propane fuels and combustion chamber diameters of 3.0 in (a) and 3.5 in (b). Taken from [34].

pulsejet performance through the development of a method of characteristics (MOC) based technique[15], which was also developed in 1947 in Germany by F. Shultz-Grunow[47]. The primary objective of this work was to investigate the large amplitude wave processes occurring during typical operation, and a simplified combustion model was assumed to model the unsteady heat release rates. The theoretical predictions did not match experimental results very closely, and the reason given for this discrepancy was the simplified combustion model. In reality, the combustion processes in a wave engine occur neither at a constant volume or constant pressure, but many of the MOC based methods assumed a constant volume combustion process.

As a participant in the SQUID program, Raymond Lockwood was also investigating pulsejets during the mid 1950's[1]. Long after the SQUID program concluded, Lockwood continued work on the pulsejet, and received several United States patents for pulsejet designs[32, 33]. Similar to the Ecrevisse valveless pulsejet developed by SNECMA motors, Lockwood patented a valveless pulsejet with a 180 degree bend, as shown in Fig. 9. Pointing the inlet in the direction of the exhaust allows the combustion products that are forced out of the inlet to contribute to positive thrust generation, but the major claim of the Lockwood patent was the non-uniform cross sectional area of the engine. Lockwood claims in the patent that the use of a continuously non-unform cross section improves starting, increases the stability of operation at a broader range of fuel flows, and provides a higher ratio of thrust to air handling capacity.

From the 1970's through the 80's, research and development on wave engines decreased significantly while interest in pulsating combustion systems shifted to applications such as more environmentally friendly heating systems[25] and toxic waste incineration[3]. Despite this shift in focus, the work of Kentfield et al. continued to examine the role of pulse combustion in propulsion[27]. In this work, Kentfield proposed pulse combustors similar to previous valveless pulsejets for use in gas turbine engines. Kentfield noted that typical Brayton cycle steady flow combustors experience a total pressure drop across the combusor that decreases the specific output of the engine by 1-2% per percent pressure drop. Therefore, Kentfield proposed that a pulsating combustor could be used to create a combustor

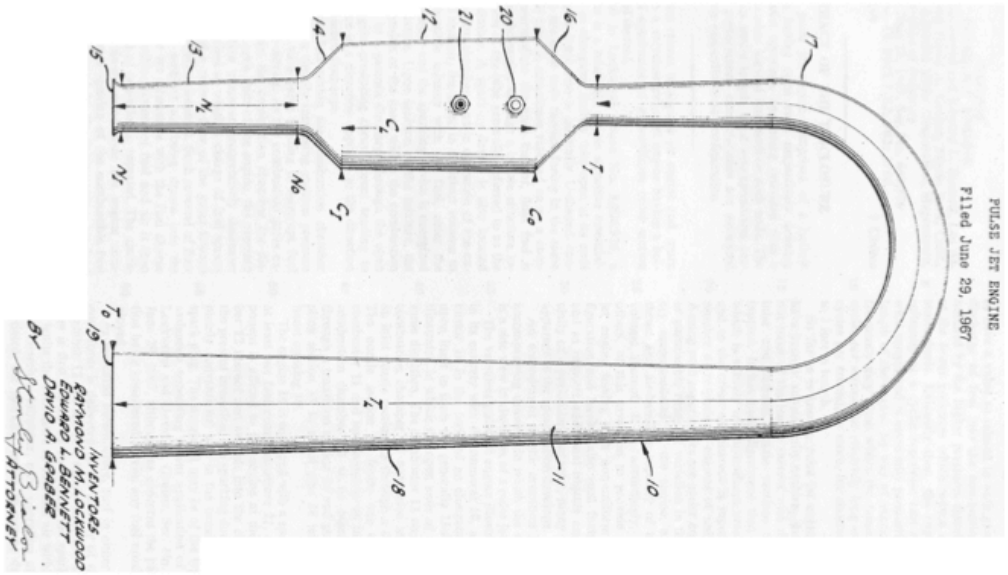

Figure 9: Valveless pulsejet described in Lockwood U.S. patent 3,462,955.

with a net stagnation pressure gain.

1.4 Fundamental Wave Engine Operating Principles

The wave engine creates thrust by generating large amplitude longitudinal flow field oscillations within the engine. These flow field oscillations are driven by an unsteady energy addition process created by the burning of reactants in a combustion chamber located near the engine inlet. Figure 10(a) describes a wave engine consisting of inlet valves, a mixing and combustion zone, and an exhaust section. The inlet valves control the injection of reactants into the combustion chamber and respond to combustor pressure oscillations by opening when the pressure downstream of the valves is lower than the upstream pressure and closing when the inlet pressure is greater than the upstream pressure. This opening and closing of the valves creates impulsive injection of reactants into the combustor which subsequently leads to an unsteady heat release rate. Fig. 10(b) displays a typical time dependence of inlet pressure and velocity as well as the total heat release rate. Initially, the pressure within the chamber is lower than the upstream pressure. At this time, the inlet valves are open and reactants enter the chamber. This impulsive injection creates a flowfield

in which cold reactants and hot combustion products from the previous cycle mix on many different length scales. This mixing leads to the heating, ignition, and rapid burning of the reactants, thus increasing the pressure within the chamber. The elevated pressure closes the inlet valves and the products of combustion leave the system through the downstream exhaust section, thereby generating thrust. The outflow of combustion products causes a decrease in the combustor pressure, allowing the cycle to repeat.

In spite of the relatively large amplitudes of the flow field oscillations generated in the wave engine, the overall engine cycle can be described to first order by acoustic wave processes and to higher orders with the addition to certain nonlinear physical processes. Hence, the frequency response of a mechanically valved wave engine is similar to that of a duct with closed-open boundary conditions, with a large response to forcing occurring at or near the natural acoustic frequencies of the engine. Since the wave engine is a self-sustained driven system and physical processes involving mixing and combustion have certain timescale constraints, most wave engines naturally operate at or near the fundamental natural acoustic frequency of the engine.

Given the large amplitude resonant acoustic oscillations and the complex unsteady flowfield essential for proper wave engine operation, it is clear that engine shape will influence engine performance through both the mean flow and the acoustic characteristics. While previous studies on wave engines have acknowledged that engine shape will impact performance[15, 47, 1], no wave engine studies have systematically examined the role of engine shape on overall performance. Similar to the wave engine, acoustic compression devices designed for refrigeration[35] also require the generation of large amplitude pressure oscillations. These oscillations are generated by sinusoidally forcing a closed, gas filled duct at or near its fundamental natural acoustic frequency. Early studies of forced resonant oscillations in narrow, straight, constant diameter ducts observed and predicted an upper limit of oscillation amplitude independent of forcing amplitude and the formation of shock waves[8]. The limit on attainable amplitude and formation of shock waves in these systems is a result of waveform steepening due to gas dynamic nonlinearities that become more important as oscillation amplitude increases. These nonlinearities transfer acoustic

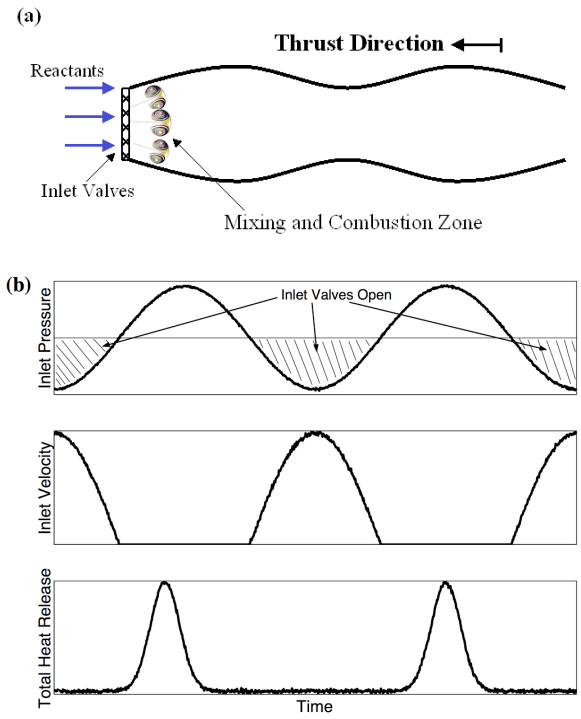

Figure 10: (a) Simplified wave engine schematic, and (b) qualitative time dependence of inlet pressure, inlet velocity, and total heat release rate.

energy from the driven mode into higher harmonics (integer multiples) of the fundamental. As more acoustic energy is transferred from the fundamental into higher harmonics, the waveforms of the driven oscillations steepen until shock waves develop. Shock waves dissipate more energy through viscous mechanisms, thus limiting the maximum attainable amplitude. On the other hand, more recent studies[31, 21] have shown that oscillations driven inside ducts whose diameter changes in the axial direction can reach much larger amplitudes with more continuous waveforms than oscillations driven inside straight ducts. One significant difference between shaped and straight ducts is the relationship between the fundamental and higher natural acoustic frequencies of the two systems. In contrast with the straight duct, whose natural acoustic modes are harmonics of the fundamental, the natural acoustic modes of most shaped ducts do not oscillate at harmonic frequencies of the fundamental. This decreases the transfer of acoustic energy from the fundamental mode into higher harmonics. The larger amplitudes and more continuous waveforms are a direct result of this significant decrease in the transfer of acoustic energy out of the fundamental

mode.

In addition to acoustic compression devices, researchers working on combustion instabilities in liquid rockets have also hypothesized a link between the generation of very large amplitude pressure oscillations to decreased nonlinear acoustic energy transfer. Experimental studies of combustion instabilities in liquid rocket motors[10] have reported pressure oscillations of the first, tangential spinning acoustic mode of the combustion chamber with maximum amplitudes of over 4000 psi above the mean pressure. The large amplitudes of these oscillations are attributed to the fact that, similar to longitudinal natural acoustic mode frequencies of shaped ducts, the transverse natural acoustic mode frequencies of these engines are also not harmonics of the fundamental. This study hypothesized that unstable oscillations in these liquid rocket motors at the first tangential mode did not experience significant acoustic energy transfer from this mode into higher transverse acoustic modes, resulting in very large amplitude spinning waves. However, the study did not conclusively link the large amplitude combustion instabilities with nonlinear acoustic energy transfer. Furthermore, a more recent study by Burnley and Culick[7] concerning transverse combustion instabilities in cylindrical combustion chambers developed a more detailed mathematical formulation of the role of nonlinear gas dynamics in energy transfer between transverse acoustic modes. This study concluded that larger amplitude limit cycle oscillations are generated in systems where the difference between the linear natural acoustic frequencies and the harmonics of the fundamental transverse natural acoustic mode is larger.

The generation and sustainment of large amplitude pressure oscillations in wave engines and related combustion instabilities is the result of a positive feedback between unsteady heat release rates and local pressure oscillations. The well known Rayleigh criterion[43] provides an illustrative framework to examine the role of fluctuating heat release in the driving of large amplitude oscillations within a wave engine. Rayleigh's criterion states that the amplitude of pressure oscillations are reinforced or driven when in the presence of a fluctuating heat release of the same phase. For a wave engine operating at the fundamental, quarter wave resonant frequency, this criterion suggests that the fluctuating heat release

should be designed to occur while the pressure in the engine is near the maximum amplitude. Unfortunately, due to the complexity of the mixing processes responsible for the heat release rates in the wave engine, a detailed understanding of unsteady heat release rates does not currently exist.

In fact, mixing processes associated with the formation and subsequent breakdown of coherent vortical structures control the heat release rates in many unsteady combustion systems, and previous work on these systems reveals the importance of unsteady mixing processes on wave engine performance. Experimental and theoretical work completed at Sandia National Laboratories on a premixed unsteady combustion system used in drying applications (known as a pulse combustor) provides an illustration of large scale vortex formation in a laboratory pulse combustor[24]. Figure 11, taken from Barr and Keller[24], shows that the pulsed injection of reactants into a chamber with a bluff body placed in front of the injection port produces counter-rotating vortical structures around the body as evident by the particle path indicators. Notice also the subsequent breakup of the vortical structure into smaller scale structures shortly after the large vortex formation, as shown in the last column of Fig. 11. Further work[25] showed that through geometrical changes of the reactant injection system that controls the mixing characteristics, the timing and energy release rates could be substantially changed. In addition to pulse combustors, large pressure oscillations encountered in ramjet combustion chambers have also been attributed to unsteady energy release rates resulting from large vortex formation at the dump plane [22, 50].

The previous historical overview and brief discussion of the physical processes most important to wave engine operation outline the key challenges associated with the successful design of a wave engine. Given the level of maturity of virtually all wave engine designs, many research and development issues remain largely unresolved, and the goal of this thesis is to address issues involving engine shape and unsteady heat release characteristics. This is pursued by performing parametric numerical investigations to isolate the influence of specific physical processes on overall wave engine performance. To perform these parametric studies, the modeling tools used in this investigation aim to realistically simulate the important

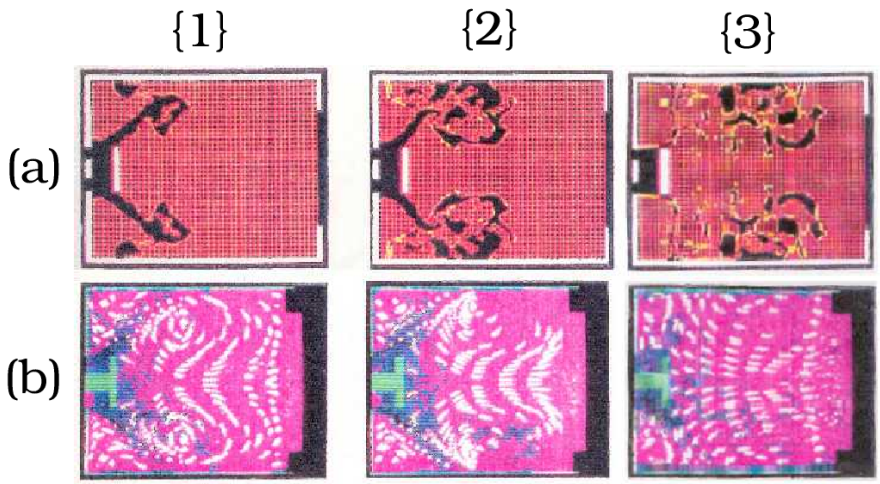

Figure 11: Large vortex formation as a result of impulsive injection[24].Top row: results from vortex dynamics model. Black indicates reactants. Bottom row: Schlieren data with particle path indicators. Left: Peak of injection. Middle: Onset of reaction. Right: Peak of reaction.

physical processes while maintaining relatively small simulation times without the need for significant computational resources.

CHAPTER II

PRELIMINARY DUCT SHAPE INVESTIGATION

The historical review and general overview of the wave engine cycle provided in the first chapter clearly showed that the physical processes necessary for successful wave engine operation are complex and not fully understood. Further, the previous chapter also discussed the similarities between oscillations driven in the wave engine and large amplitude acoustic waves driven in acoustic compression devices (i.e. resonators). In summary, oscillations driven in acoustic compression devices can attain very large amplitudes similar to the wave engine, and the waveforms and maximum amplitudes of limit cycle oscillations in acoustic resonators are determined predominantly by the physical mechanisms that dissipate acoustic energy out of the driven mode. These physical mechanisms include viscous dissipation and acoustic energy transfer resulting from gas dynamic nonlinearities. Additionally, previous experimental and theoretical studies discussed earlier have also shown these dissipation mechanisms can be strongly dependent on resonator geometry. Therefore, since acoustic compression devices are a less complex system than the wave engine while containing physical similarities, a preliminary study on the dynamics of driven oscillations in acoustic resonators may be beneficial in the design of successful wave engines.

This preliminary investigation models driven oscillations in acoustic resonators in order to explore the influence of duct geometry on large amplitude, limit cycle oscillations through nonlinear acoustic energy transfer and viscous dissipation. As Fig. 12 shows, this simplified system is modeled such that the energy addition is supplied by the periodic oscillation of the entire resonator, instead of the unsteady heat release due to the combustion of reactants. Hence, all of the energy addition occurs at the system boundaries and remains independent of the oscillations themselves.

For this investigation, a nonlinear quasi one-dimensional wave equation describes the dynamics of driven oscillations in shaped ducts, and this wave equation is solved using

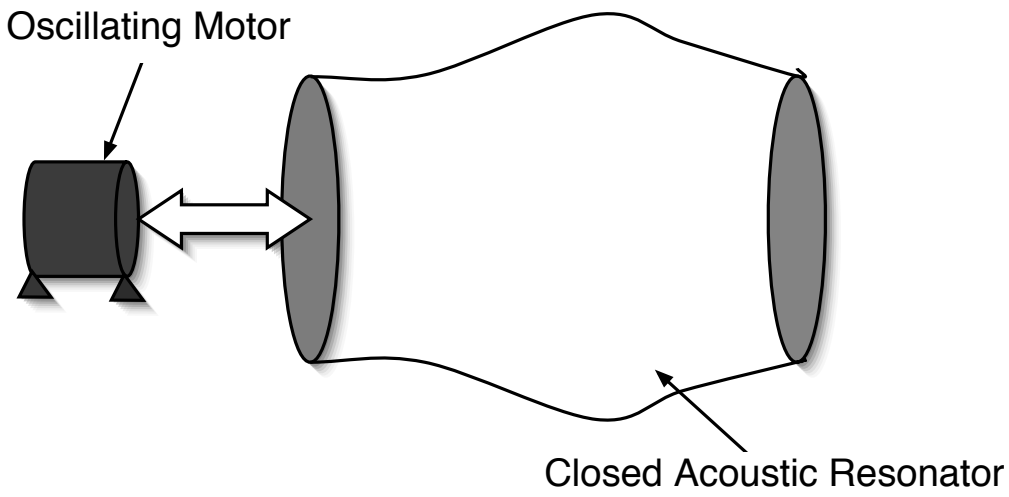

Figure 12: Illustration of forced acoustic resontor used in this investigation.

the Galerkin method. The Galerkin method is an approximate solution technique capable of providing accurate solutions to complex nonlinear partial differential equations. The Galerkin method also provides physical insight into the effect of nonlinearities on driven oscillation properties by expressing the model equation as a set of coupled nonlinear oscillators. Furthermore, the choice of this method was based on successful previous applications to the modeling of similar large amplitude oscillations in unstable combustors[12, 51]. Unfortunately, due to the inherent inability of this method to accurately model unsteady, time dependent flapper valve behavior in addition to the coupling of heat release rates and mixing processes, it is not suitable for the completion of this investigation. Therefore, a fully nonlinear, unsteady, quasi-one dimensional model based on the finite differencing of the conservation equations is proposed for the remainder of the study.

2.1 Model Equations

The nonlinear wave equation used in this study to model oscillations driven in acoustic resonators describes quasi-one dimensional, finite amplitude oscillations of a calorically perfect gas while accounting for linear and second order nonlinear processes, duct forcing and dissipation. This equation was derived by Il'inskii t al.[21] by manipulating variables

in the mass, momentum and state equations, and is given by:

$$\frac{\partial^2\Phi}{\partial\mathcal{T}^2} - \frac{1}{\Omega\pi^2}\left(\frac{1}{S}\frac{dS}{dX}\right)\frac{\partial\Phi}{\partial X} - \frac{1}{\Omega\pi^2}\frac{\partial^2\Phi}{\partial X^2} = -\frac{2}{\Omega}\frac{\partial^2\Phi}{\partial X\partial\mathcal{T}}\frac{\partial\Phi}{\partial X} - \frac{\gamma-1}{\Omega}\frac{\partial\Phi}{\partial\mathcal{T}}\frac{\partial^2\Phi}{\partial X^2} - \frac{\gamma-1}{\Omega}\left(\frac{1}{S}\frac{dS}{dX}\right)\frac{\partial\Phi}{\partial\mathcal{T}}\frac{\partial\Phi}{\partial X} - \frac{\Gamma(\mathcal{T})}{\Omega^2} + \frac{\Xi(\mathcal{T})}{\Omega^2}, \tag{1}$$

where Φ, the normalized velocity potential, is defined as

$$\frac{\partial\Phi}{\partial x} = \frac{u}{\mathcal{L}^2\omega_0}, \tag{2}$$

and X, $\mathcal{T}$, γ,and S represent the nondimensional axial distance, time, ratio of specific heats, and cross sectional area of the duct, respectively. In addition, u, $\mathcal{L}$, and ω_0 describe the dimensional axial velocity, duct length, and fundamental natural frequency of a straight duct, respectively. Finally, Eq. 1 also includes the following normalized forcing frequency parameter Ω:

$$\Omega = \frac{\omega}{\omega_0}. \tag{3}$$

It is important to note that Eq. 1 describes oscillations in a coordinate system that is attached to the duct. Consequently, the flow velocity at the resonator boundaries is zero and the effect of periodic forcing of the duct manifests itself as a body force applied directly to the gas in the duct. This reference frame significantly simplifies the boundary conditions of the problem. The left side of Eq. 1 is the linear wave operator while the right side describes non-linear processes (i.e., the first three terms), forcing (terms involving Γ), and dissipation due to viscous processes (terms involving Ξ). In this case, the forcing term Γ is given by:

$$\Gamma(X,\mathcal{T}) = F\frac{\partial\Phi}{\partial X} + \Omega\frac{\partial F}{\partial\mathcal{T}}X + (\gamma-1)\left(\frac{1}{S}\frac{dS}{dX}\right)\frac{\partial\Phi}{\partial X}FX + (\gamma-1)\,F\frac{\partial^2\Phi}{\partial X^2}X, \tag{4}$$

where F describes the normalized time dependent forcing function that accelerates the entire duct. Finally, dissipation by viscous forces, denoted by Ξ in Eq. 1, is given by:

$$\Xi(X,\mathcal{T}) = \frac{\mathcal{D}\Omega}{\pi^3 S}\frac{\partial^2}{\partial\mathcal{T}\partial X}\left(S\frac{\partial\Phi}{\partial X}\right), \tag{5}$$

where $\mathcal{D}$ is a dimensionless dissipation parameter whose magnitude is determined by experimental results[31].

2.2 Solution Technique

The application of the Galerkin method begins with the assumption that the velocity potential can be represented by the following infinite series:

$$\Phi(X,\mathcal{T}) = \sum_{n=1}^{\infty} \eta_n(\mathcal{T})\Psi_n(X), \tag{6}$$

where $\Psi_n(X)$ describe the spatial dependence of the natural acoustic mode shapes of a given duct geometry (to be discussed in detail later), and $\eta_n(\mathcal{T})$ are the unknown, time dependent amplitudes of these acoustic modes. Since in practice Eq. 6 is truncated to a finite number of modes, the resulting solution for Φ is approximate and does not satisfy Eq. 1 exactly. Specifically, when the truncated series for Φ is substituted into Eq. 1 the resulting expression, called the residual ($R(\Phi)$), is nonzero. The strategy of the Galerkin method is to derive a set of equations for the time dependent amplitudes, $\eta_n(\mathcal{T})$, that when solved will minimize the residual ($R(\Phi)$). To derive the system of equations for the amplitude functions $\eta_n(\mathcal{T})$, the truncated Eq. 6 is first substituted into Eq. 1. The next step in the solution approach takes advantage of the property of orthogonality, which states that a continuous function (here $R(\Phi)$) is zero if it is orthogonal (i.e. inner product equal to zero) to every member of a complete set[14]. This orthogonality property leads to the formation of the following expression:

$$\int_0^{\mathcal{L}} R(\Phi(X,\mathcal{T})) \cdot W_n(X) dX, \tag{7}$$

where the weighting functions, $W_n(X)$, must consist of a complete set of functions. For this problem, the weighting functions are determined based on the duct shape and the trial functions and will be discussed later. Furthermore, the use of natural acoustic mode shapes as trial functions also satisfy the boundary conditions exactly, thus eliminating any residuals at the boundary. Performing the integration in Eq. 7 over the duct length expressed in Eq. 7 results in a set of time dependent coupled ordinary differential equations:

$$\begin{array}{l} \sum_n G_{1n}\ddot{\eta}_1 - \sum_n \mathcal{R}_{1n}\eta_n + \sum_n \sum_m \left(Z_{1nm}\dot{\eta}_n\eta_m\right) + \sum_n E_{1n}(\mathcal{T}) - \zeta_{1n}(\mathcal{T}) = 0 \\ \sum_n G_{2n}\ddot{\eta}_2 - \sum_n \mathcal{R}_{2n}\eta_n + \sum_n \sum_m \left(Z_{2nm}\dot{\eta}_n\eta_m\right) + \sum_n E_{2n}(\mathcal{T}) - \zeta_{2n}(\mathcal{T}) = 0 \\ \vdots \\ \sum_n G_{jn}\ddot{\eta}_j - \sum_n \mathcal{R}_{jn}\eta_n + \sum_n \sum_m \left(Z_{jnm}\dot{\eta}_n\eta_m\right) + \sum_n E_{jn}(\mathcal{T}) - \zeta_{jn}(\mathcal{T}) = 0 \end{array} . \tag{8}$$

where G_{jn} and $\mathcal{R}_{jn}$ describe linear phenomena, Z_{jnm} describes nonlinear coupling, ζ_{jn} describes viscous damping and E_{jn} describes forcing. These quantities are described by the following expressions:

$$G_{jn} = \int_0^1 W_j(X)\Psi_n dX, \tag{9}$$

$$H_{jn} = \int_0^1 W_j(X)\left[\frac{d^2\Psi_n}{dX^2} + \left\{\frac{1}{S}\frac{dS}{dX}\right\}\frac{d\Psi_n}{dX}\right]dX, \tag{10}$$

$$Z_{jnm} = \frac{A_{jnm} + B_{jnm} + C_{jnm}}{\Omega}, \tag{11}$$

$$A_{jnm} = (\gamma-1)\int_0^1 W_j(X)\left\{\frac{1}{S}\frac{dS}{dX}\right\}\Psi_n\frac{d\Psi_m}{dX}dX, \tag{12}$$

$$B_{jnm} = (\gamma-1)\int_0^1 W_j(X)\Psi_n\frac{d^2\Psi_m}{dX^2}dX, \tag{13}$$

$$C_{jnm} = 2\int_0^1 W_j(X)\frac{d\Psi_n}{dX}\frac{d\Psi_m}{dX}dX, \tag{14}$$

$$\begin{aligned} E_{jn}(\mathcal{T}) = &\left[\int_0^1 W_j(X)\frac{d\Psi_n}{dX}dX + (\gamma-1)\int_0^1 W_j(X)\left\{\frac{1}{S}\frac{dS}{dX}\right\}\frac{d\Psi_n}{dX}XdX+\right]F\eta_n+ \\ &+\left[(\gamma-1)\int_0^1 W_j(X)\frac{d^2\Psi_n}{dX^2}XdX\right]F\eta_n + \left[\Omega\int_0^1 W_j(X)XdX\right]\frac{dF}{d\mathcal{T}}, \end{aligned} \tag{15}$$

Specification of initial conditions, trial functions $\Psi_n(X)$, and weighting functions $W_n(X)$ provides all the information needed to solve Eqs. 8, which are numerically integrated to determine the amplitude functions $\eta_j(\mathcal{T})$. Finally, once Φ is determined, the remaining variables of interest can be found[21]. For example, the pressure at any location can be calculated using the following expression:

$$\frac{P}{P_0} = \left[1-(\gamma-1)\pi^2\left(\Omega\frac{\partial\Phi}{\partial\mathcal{T}} + \frac{1}{2}\left(\frac{\partial\Phi}{\partial X}\right)^2 + FX - \frac{\mathcal{D}}{\pi^3}\frac{\partial^2\Phi}{\partial X^2}\right)\right]^{\frac{\gamma}{\gamma-1}}. \tag{16}$$

2.3 Trial Functions

The choice of trial functions $\Psi_n(x)$ used in the Galerkin method are often solutions of simpler, yet related problems. For this study, $\Psi_n(x)$ are chosen to be the natural acoustic modes of the same or similarly shaped duct. These functions can be determined analytically for certain duct shapes by solving the following linear wave equation, corresponding to the left hand side of Eq. 1;

$$\Omega^2\frac{\partial^2\Phi}{\partial\mathcal{T}^2} - \frac{1}{\pi^2}\frac{1}{\mathcal{A}}\frac{d\mathcal{A}}{dX}\frac{\partial\Phi}{\partial X} - \frac{1}{\pi^2}\frac{\partial^2\Phi}{\partial X^2} = 0 \tag{17}$$

where $\mathcal{A}$ describes the axial dependence of the cross sectional area of a duct that may equal or differ from that of the investigated duct. Note that Eq. 17 is a form of the Webster horn equation[30] in terms of velocity potential. To illustrate the determination of trial functions used in this study, consider a duct with exponentially varying axial cross sectional area:

$$\mathcal{A} = \mathcal{A}_0 exp(\alpha X) \tag{18}$$

where $\mathcal{A}$ satisfies the relationship

$$\frac{1}{\mathcal{A}}\frac{d\mathcal{A}}{dX} = \alpha \tag{19}$$

Given that the frame of reference of this study is attached to the duct, Φ must satisfy zero velocity boundary conditions. Assuming $\Phi(X, \mathcal{T}) = \tau(\mathcal{T})\Psi(X)$ and using the method of separation of variables to solve Eq. 17 subject to the zero velocity boundary conditions, one obtains an equation of the classical Sturm Liouville type equation with the following sets of eigenfunctions and eigenvalues:

$$\Psi_n(X) = \exp\left(\frac{-\alpha X}{2}\right)\left(\cos(n\pi X) + \frac{\alpha}{2n\pi}\sin(n\pi X)\right) \qquad \text{(for n=1,2,3,...)} \tag{20}$$

$$\mathcal{K}_n^2 = \left(\frac{\omega_n}{c_0}\right)^2 = (n\pi)^2 + \frac{\alpha^2}{4} \tag{21}$$

where $\Psi_n(X)$ form a complete set and $\mathcal{K}_n$ are the natural acoustic wave numbers of the duct. An examination of the natural acoustic mode frequencies determined by Eq. 21 illustrates an important difference between straight and shaped ducts. Consider, for example, the natural acoustic mode frequencies of two ducts, one straight and one horn shaped having the same fundamental natural acoustic mode frequency. The first four natural acoustic mode frequencies were calculated using Eq. 21 for a straight ($\alpha = 0.0$, $l = 0.165m$) and for a horn shaped duct ($\alpha = 5.75$, $l = 0.2237m$) using a sound speed of 330 m/s, see Table I. The determination of natural acoustic mode frequencies for horn shaped ducts provides an analytical example as well as a quantitative measure of the well documented[21] shifting of natural acoustic mode frequencies that is important to this problem. Upon determination of the trial functions, the final terms needed for a complete description of the time dependent amplitude Eqs. 8 are the weighting functions, $W_j(X)$. The weighting functions, defined in

Table 1: Calculation of natural acoustic mode frequencies for straight and horn shaped ducts based on Eq. 21. Assumed sound speed and flare constant of 330m/s and 5.75, respectively.

Natural Mode	Straight Duct Natural Frequency (Hz)	Horn Shaped Duct Natural Frequency (Hz)
1	1000	1000
2	2000	1623
3	3000	2314
4	4000	3027

this study as

$$W_n(X) = A(X)\Psi_n(X) \tag{22}$$

are based on the following orthogonality condition of $\Psi_n(X)$ from Eq. 20:

$$\int_0^1 [A\Psi_n]\,\Psi_m = 0 \qquad \text{when n} \neq \text{m} \tag{23}$$

The weighting functions of Eq. 22, based on the orthogonality condition of Eq. 23 simplify the first terms of Eqs. 8 by reducing the summation to a single term. This simplification transforms Eqs. 8 into a system of nonlinear oscillators where the energy transfer between modes is modeled as the coupling between elements oscillating at the natural frequencies of the duct. While the discussion above was limited to ducts with exponentially varying cross sectional areas, similar analytical solutions can be found for other classes of duct shapes. In addition, as long as the choice of trial functions forms a complete set and satisfies the boundary conditions, this method can be applied to model any arbitrary duct shape (within the applicability of the model equation).

2.4 Results

Figure 13 presents a comparison of the predictions using the Galerkin method with two sets of previously published results[21, 9]. The results describe the pressure oscillations at one end of a straight duct forced at its fundamental natural acoustic frequency. For one of the comparisons, the Galerkin method and Ilinskii et al.[21] numerical approaches were used to solve a nearly identical model equation (i.e. Eq. (1)). The one difference between the

two approaches, other than the differing solution techniques, is the exclusion of the third order nonlinearities in the equations solved with the Galerkin method. The third order nonlinearities are apparently not important in the investigated problem as the solution using the Galerkin method is in excellent agreement with the Ilinskii et al. results. The second comparison in Fig. 13 corresponds to the problem solved by Chun and Kim.[9]; i.e. a sinusoidally driven 0.2 meter long duct filled with 27C R-12 refrigerant (Mol. Weight = 120.09, $\gamma = 1.129$). In order to compare with results using the Galerkin method, the dimensional forcing amplitude (a_0) of $100 m/s^2$ reported by Chun and Kim is normalized, leading to a value for F_0 of 8.939e-5. It is noteworthy that in spite of the fact that Chun and Kim solved a different set of model equations and used a different numerical solution technique, the results are nearly identical to those obtained by the Galerkin method. Furthermore, the similar pressure amplitudes of these two studies are attributed to the use of the same value for the viscosity coefficient, which was based on the value chosen by Ilinskii et al.

Consider a straight duct that is closed at both ends and oscillated periodically at the frequency of maximum response. Figure 14 (a) and (b) present the temporal pressure history at one end of the duct. Figure 14(a) shows the time evolution of the pressure starting from rest. Notice a growth in the amplitude until the time when the pressure amplitude saturates and limit cycle oscillations are obtained. The pressure signal displayed in the remainder of the figure represents several oscillations of this limit cycle behavior. The maximum pressure obtained for this setup is of the the order of 10% of the mean, with a compression ratio of approximately 1.22. In addition, the waveform of oscillations driven in the straight duct resemble steep fronted shockwaves which travel back and forth through the duct. The steepening of the waveform is a result of the nonlinearity of the gasdynamics whose effect becomes more pronounced as oscillation amplitude grows.

Figure 15 shows the time dependence of limit cycle oscillations forced in a straight duct and the FFT of the oscillations. Note that the power in the FFT is normalized with respect to the power in the fundamental mode. Therefore, the fundamental mode is not fully shown in the figure, in order to better show the power content of higher harmonics. Figure 15 shows that the power contained in the first harmonic is over 16 percent of the power in

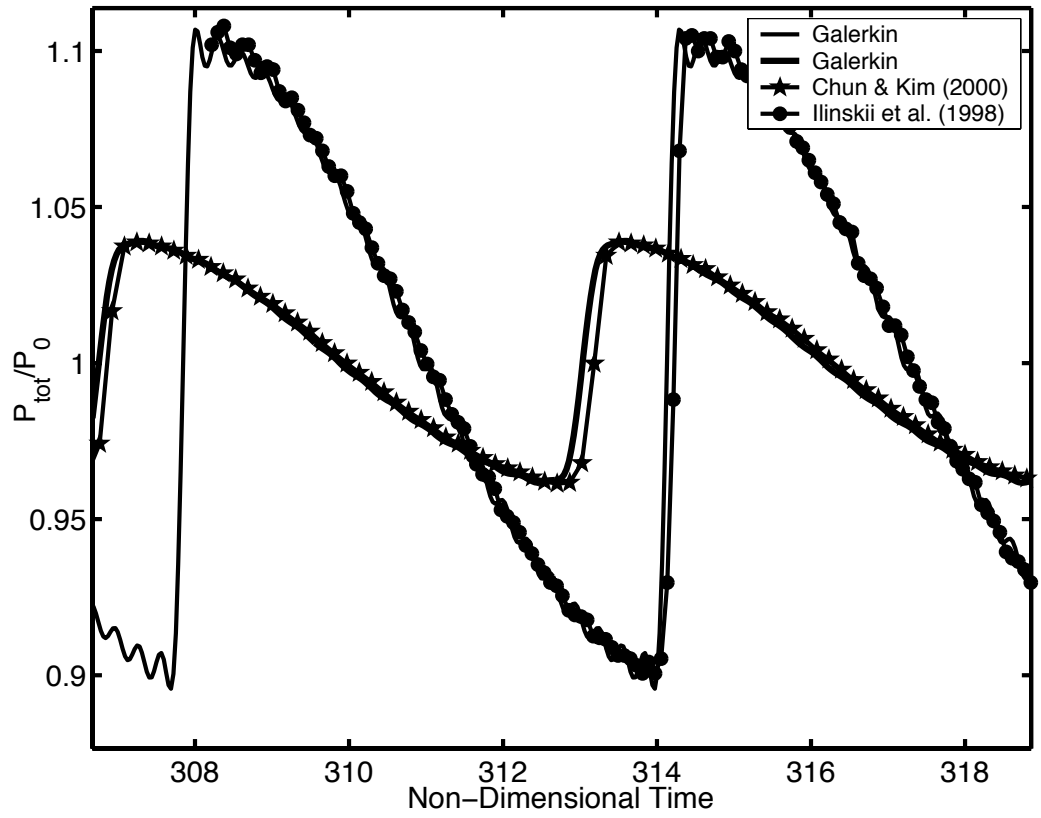

Figure 13: Comparison of driven pressure oscillations within straight ducts using the Galerkin method with two other published results. Results from Galerkin method for comparison with Ilinskii et al.[21] data correspond to larger forcing amplitude than that of the Chun and Kim[9] study.

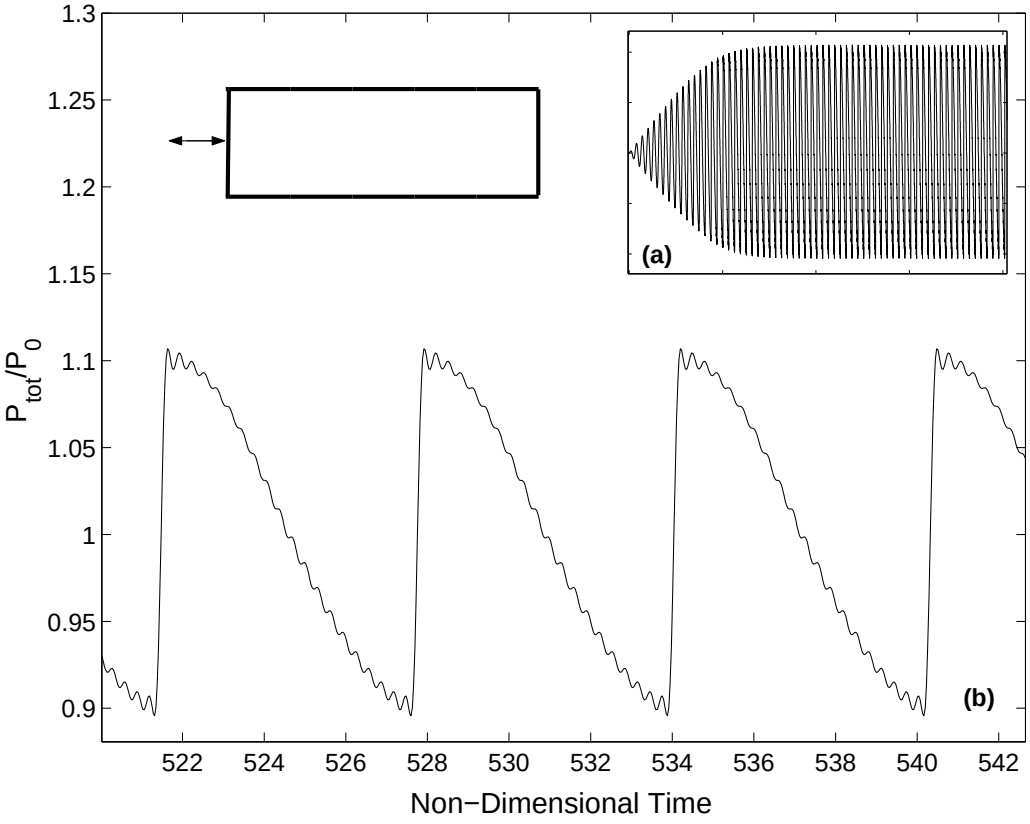

Figure 14: (a): Time evolution of pressure at a closed end of a cylindrical duct forced at the fundamental natural frequency starting from rest. (b): Enlarged view of the limit cycle behavior.

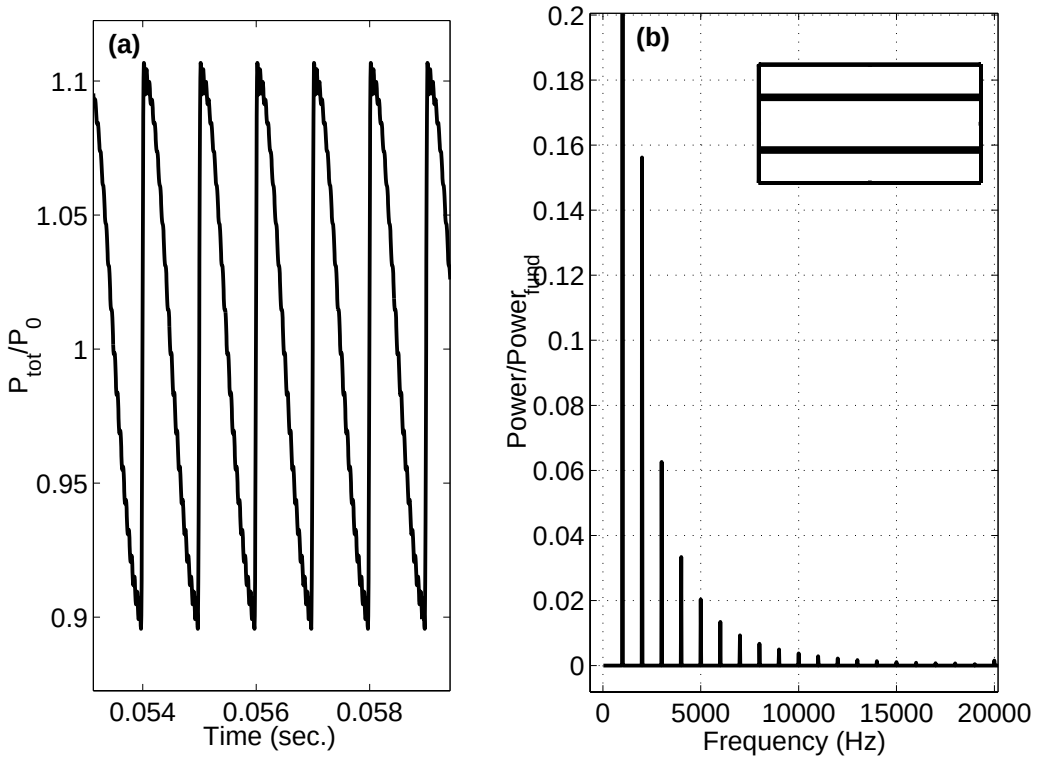

Figure 15: (a) Time dependence of finite amplitude, limit cycle pressure oscillations driven in a straight duct ($F_0 = 5e-4$, $\Omega = 1.0$, $c_0 = 330m/s$, $\mathcal{L} = 0.165m$), and (b), the corresponding FFT. Duct shape is shown in the upper right portion of (b). Note that the power in the FFT is normalized with respect to the power in the fundamental mode.

the fundamental, forced mode, with the relative power decreasing for higher harmonics. The frequency content of driven oscillations provides a measure of the energy transfer between the driven mode and higher harmonics created as a result of nonlinear processes.

Figure 16 describes the frequency dependence of the amplitude of the pressure oscillations when forced at different amplitudes. The results indicate a slight skewing of the maximum response frequency for the cylindrical duct (See [11]). In addition, this skewing also appears to be slightly dependent on the forcing amplitude, as shown by an increase in frequency shift for increasing forcing amplitude. The vertical line in Fig. 16 represents the non-dimensional fundamental natural acoustic frequency for the straight duct.

Now consider another duct forced in a similar manner, whose shape is changed to resemble a horn that is closed at both ends. The forcing coefficient is the same as the one used in straight duct calculations ($F_0 = 5.0e-4$), and the forcing frequency ($\Omega = 1.36$)

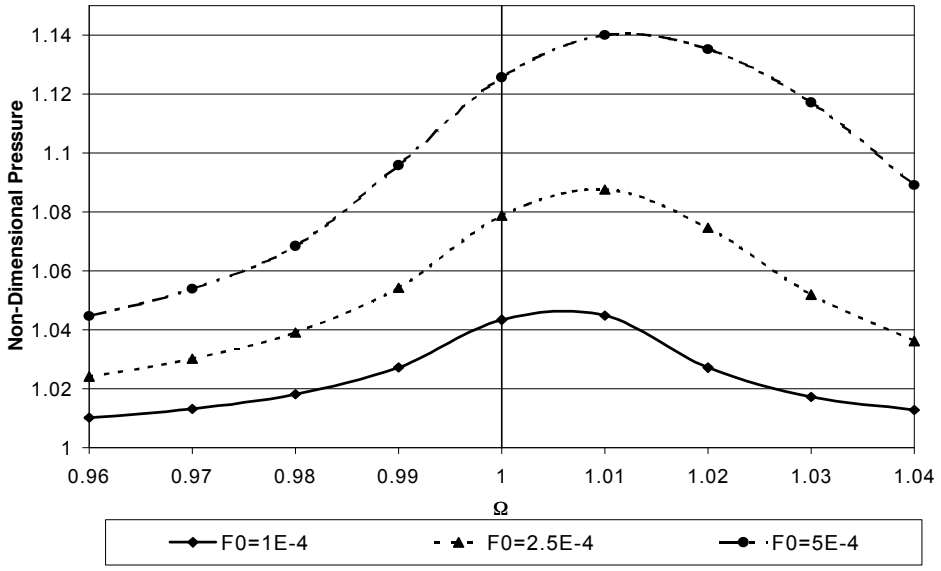

Figure 16: Frequency dependence of limit cycle pressure oscillations for different forcing amplitudes in a straight duct.

corresponds to the frequency of maximum response for a duct with a flare constant (α) of 5.75. Figure 17 (a) displays the time dependence of limit cycle pressure oscillations at the small end of the duct. The maximum normalized pressure amplitude equals approximately 2.5, as compared to approximately 0.15 for the straight duct. Figure 17 (a) also presents a prediction based on only 5 modes showing that the compression ratio is only slightly larger when compared with the 20 mode calculation. Additionally, the waveform and frequency of the two calculations are very similar to one another, thus suggesting that the influence of higher harmonics for this duct is less significant than for the straight duct. Figure 17 (a) also establishes that the shape of the waveform no longer resembles the sawtooth shape found in the straight duct. The FFT of the waveform, shown in Fig. 17 (b), indicates that the amplitudes of the higher harmonics relative to the forced mode are much smaller than those observed in Fig. 15 (b) for the straight duct; i.e. the power of the first harmonic in the horn shaped duct is approximately 2 percent of the energy of the fundamental. Further, Fig. 18 presents a comparison of temporal pressure traces for both the straight and horn shaped ducts. The horn shaped duct attains a maximum pressure amplitude of around 2.8

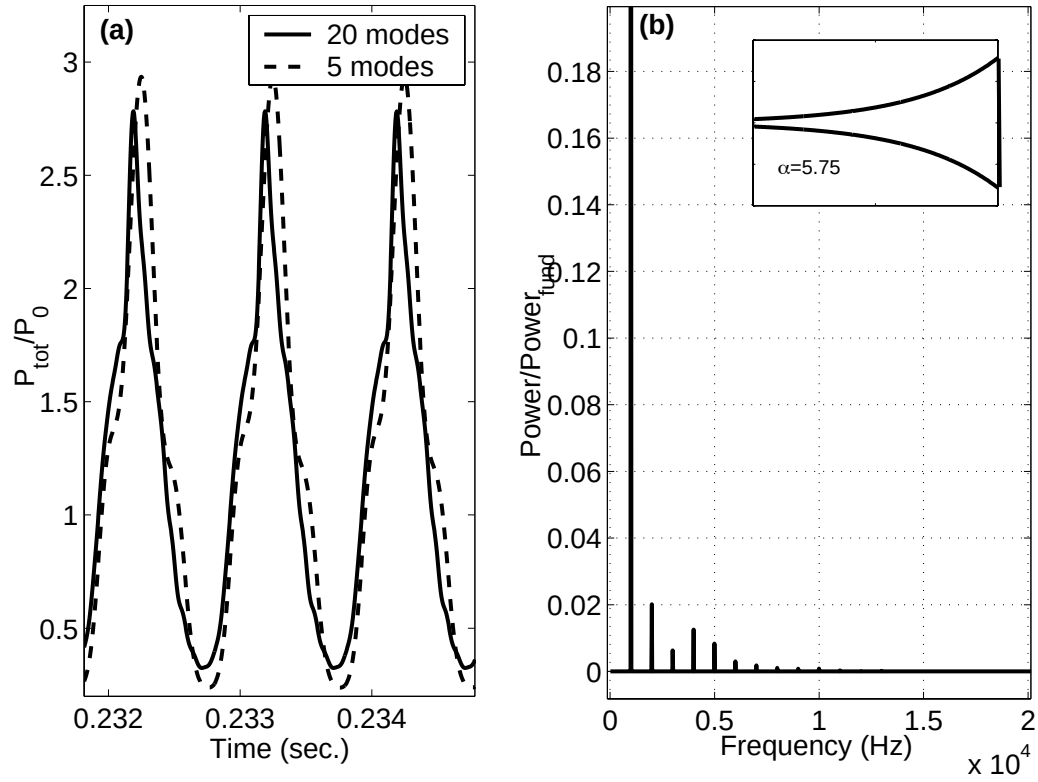

Figure 17: Time dependence (a) and frequency content (b) of driven oscillations at the small end of horn shaped duct ($\alpha = 5.75$, $F_0 = 5E{-}4$, $\Omega = 1.36$, $c_0 = 330m/s$, $\mathcal{L} = 0.224m$). The frequency content in (b) corresponds to the calculations including 20 modes (solid line in (a)).

times ambient as well as a compression ratio of over 8.5.

While it was clearly demonstrated that with a given forcing amplitude it is possible to excite much larger amplitude oscillations in shaped ducts, it is still not clear whether an optimal duct shape can be found based on a desired performance parameter; i.e., is it possible that the compression ratio for a given volume and forcing amplitude is maximized for only one duct shape? This possibility was examined for a simplified problem by finding the flare constant, α that maximizes the compression ratio for horn-shaped ducts. Figure 19 shows the maximum compression ratio for different flare constants ranging from 3.0 to 6.75. The results presented in Fig. 19 reveal that the compression ratio does not monotonically increase as the shape of the duct diverges from that of the straight geometry. In fact, a significant decrease in compression ratio occurs as the flare constant is increased from 5.75

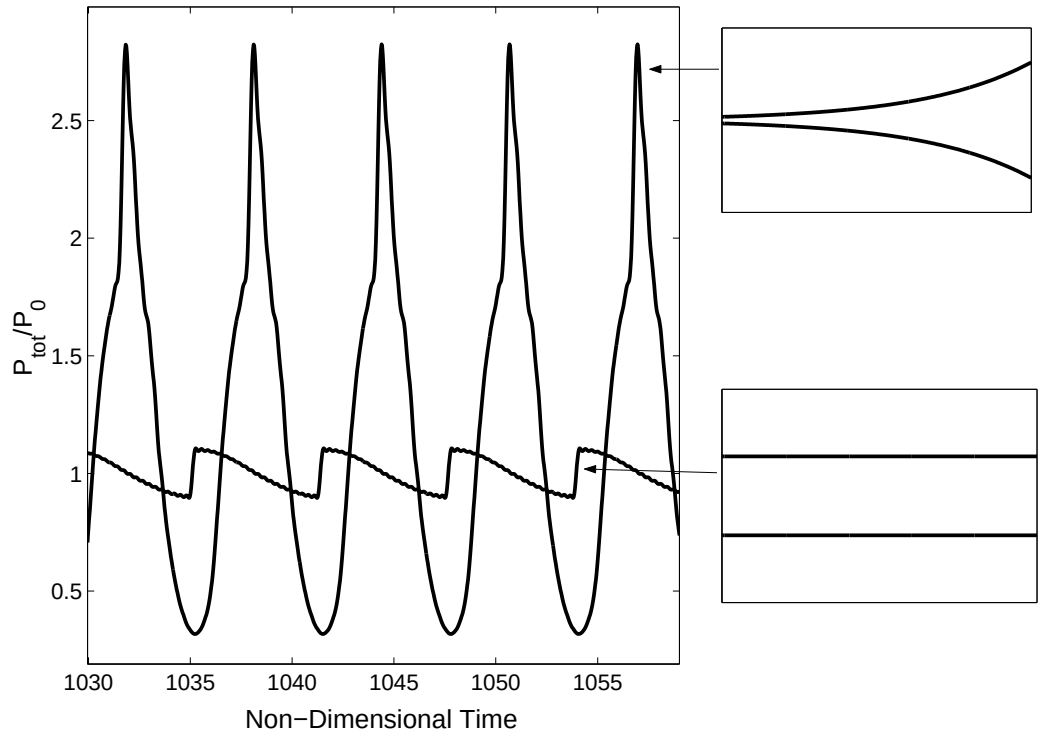

Figure 18: Pressure oscillations excited in straight and horn shaped closed ducts of equal volume using single frequency sinusoidal forcing.

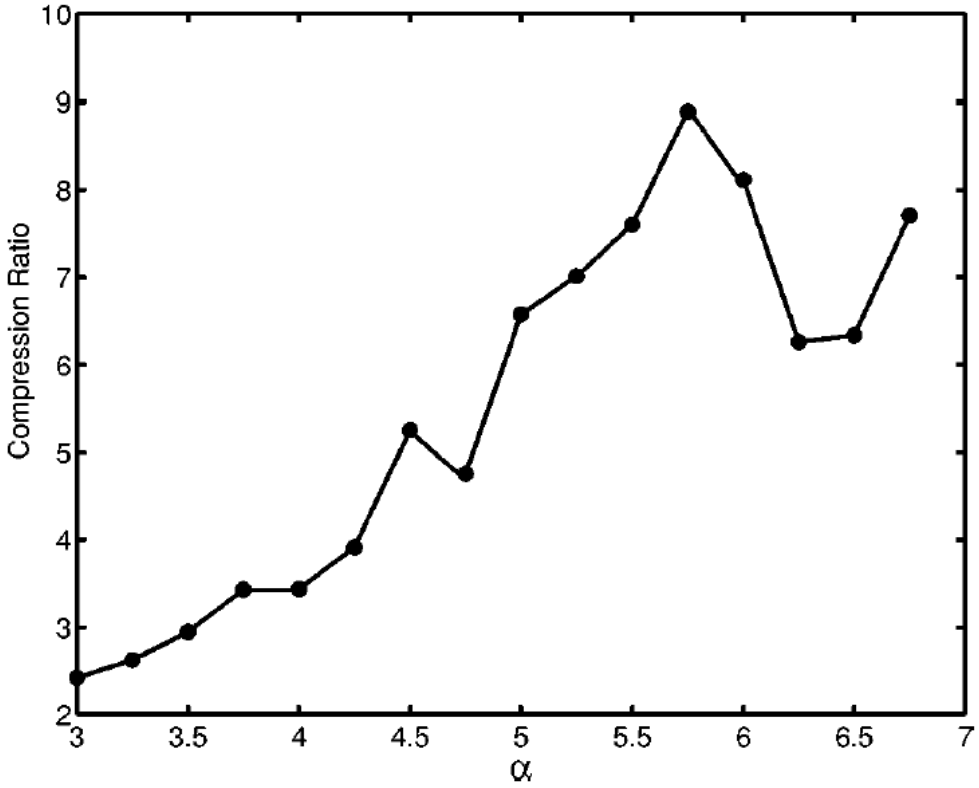

Figure 19: Dependence of compression ratio on flare constant for exponential horn shaped acoustic resonators.

to 6.25. These findings suggest that caution must be exercised in the design of acoustic compression devices because slight changes in duct shape can have a significant impact on overall performance.

Differences in waveforms between the horn shaped duct and the straight duct are strongly influenced by gas dynamic nonlinearities, but the large difference in amplitude is attributable to the conservation of total acoustic energy, i.e. when the cross sectional area of the duct decreases, the amplitude of the oscillation increases. Therefore, the impact of duct shaping on oscillation amplitude primarily through nonlinear processes should be examined not only with ducts of a similar volume but also having similar cross sectional areas at the ends. For the following results, a straight duct was assumed for the determination of the trial functions, while duct shapes found in Hamilton et al.[19] were examined

as described by the following expression:

$$S(X) = S_0 \left(\exp\left[a_m \cos(2m\pi X) + a_n cos(2n\pi X) + \ldots\right]\right) \tag{24}$$

This class of duct shape controls the shifting of individual natural acoustic mode frequencies with respect to those of the straight duct thereby having an effect on the nonlinear properties of the system. In Eq. 24, the subscripts $m, n, \ldots$ denote the specific natural acoustic mode frequencies to be shifted by an amount dependent on a_m, a_n, respectively. Hence, for the shifting of the second natural acoustic frequency only, m = 2, $a_m \neq 0$, and $a_n = 0$. Figure 20 presents results for three different duct shapes, chosen to correspond to the selective shifting of the frequencies of the second ($a_2 = -0.5$, $a_3 = 0$) and third ($a_2 = 0$, $a_3 = -0.5$) natural acoustic modes as well as the simultaneous shifting of both frequencies ($a_2 = -0.5$, $a_3 = -0.5$). The pressure traces show that for the duct shape with shifting of the second natural acoustic mode frequency only, there is still a portion of the waveform with very steep property gradients; yet unlike the sawtooth waveform driven in the straight duct, the pressure continues to rise after this sharp jump. It is also apparent from Fig. 20 that the maximum amplitude of the oscillations driven in all three shaped ducts is considerably larger than for the straight duct. While the maximum amplitude of pressure oscillations given the same driving amplitude for the straight duct was around 10% of the mean, the maximum amplitude for all three shaped ducts lies between 25% and 35% of the mean. In conclusion, results presented for a closed system with no mean flow have shown that harmonic energy transfer can be controlled through duct shape.

While the previous results provide a foundation for the understanding of the influence of duct shape on the properties of driven large amplitude gas oscillations, it must be pointed out that the operation of the wave engine and an acoustic compression device differ in several important ways. First, the wave engine requires a significant mean flow through the chamber as a result of large inflow and exhaust processes. Additionally, there are also large temperature gradients in both space and time in the wave engine that do not exist in the resonator. Both of these factors will alter the natural acoustic mode shapes and frequencies of the system. Second, while the resonator has physically simple boundary conditions,

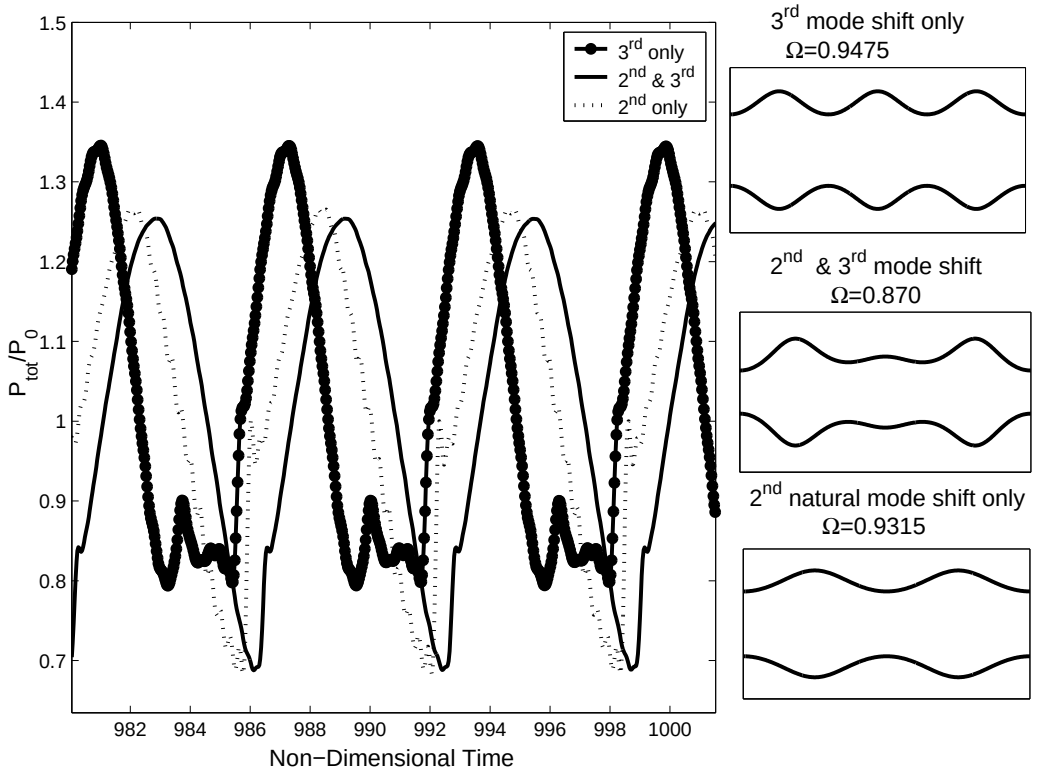

Figure 20: Pressure oscillations at an end of three different duct shapes motivated by study of Hamilton et al[19]. For duct shapes displayed on the right, the top, middle, and lower ducts correspond to $a_2 = 0$, $a_3 = -0.5$, $a_2 = -0.5$, $a_3 = -0.5$, and $a_2 = -0.5$, $a_3 = 0$, respectively.

the wave engine requires aerodynamic of flapper valves and an exhaust boundary that connect the processes within the engine with the "outside world". Furthermore, neither of these boundary conditions can be satisfied sufficiently using the previously explored trial functions. Third, energy input for the wave engine occurs via the combustion of reactants as opposed to the simple oscillation of the entire duct used in resonator studies. For the resonator, the energy input was concentrated at the closed ends of the system and was not affected by any of the processes occurring inside the resonator itself. In contrast, the driving mechanism in the wave engine is now a function of both the pressure field within the engine and fluid dynamic structures in the flow and no straightforward means of modeling this behavior exists for such an unsteady system within the Galerkin methodology. Therefore, while the Galerkin method was useful for clarifying the influence of duct geometry on nonlinear acoustic energy transfer in large amplitude, limit cycle oscillations, it is no longer feasible for a full wave engine simulation.

CHAPTER III

WAVE ENGINE MODEL DEVELOPMENT AND NUMERICAL IMPLEMENTATION

The objective of the previous study was to determine the influence of duct shape on nonlinear acoustic energy transfer between harmonics when large amplitude oscillations are driven in closed systems. The Galerkin method based technique discussed in the previous chapter provided a modeling tool for rapid studies of the dynamical aspects of large amplitude driven oscillations such as system response to different forcing frequencies and amplitudes as well as the influence of gas-dynamic nonlinearities on oscillation properties. However, it is generally agreed upon that this technique is not as effective at examining the detailed physical phenomena responsible for the driving mechanisms in unsteady combustion systems. These physical processes include turbulent mixing processes and chemical kinetics which strongly influence the unsteady combustion that drives oscillations in wave engines. Furthermore, there are currently no comprehensive reduced order unsteady heat release rate models for wave engine applications. While Galerkin method based techniques are very useful for studying the dynamics of complex systems with well defined physical processes such as the previous study on acoustic compressors, the accurate simulation of wave engine behavior requires the development of reduced order sub-models for mixing and combustion processes. Therefore, the following modeling tool expands on the foundations developed in the previous chapter by taking into account additional physical processes necessary to accurately capture unsteady combustion processes responsible for driving oscillations wave engines.

The modeling approach for the following wave engine simulations retains the quasi one-dimensionality of the previous Galerkin method based technique but now solves directly the nonlinear conservation equations, including the energy and species conservation equations to account for unsteady heat release. The solution of the unsteady conservation equations

is based on spatial finite differencing and time-marching, and the boundary conditions are modeled using a characteristic based technique that accurately simulates wave reflections and mean flow through the engine. Additionally, given the importance of mixing processes in the operation of the wave engine, this modeling approach includes a sub-model based on a one dimensional mixing model specifically tailored to the mixing characteristics of wave engines.

3.1 Detailed Wave Engine Operation

Figure 21 describes the behavior of various phases of the cycle during limit cycle wave engine operation. Starting with phase I, the flapper valves are open and reactants enter the combustion chamber. At this time, the pressure downstream of the valves is lower than the pressure upstream of the flapper valves, resulting in the an impulsive injection process. During phase II, large scale coherent structures develop as cool reactants are injected into hot combustion products from the previous cycle. As discussed previously, large scale vortex formation facilitates the mixing of cooler reactants with hot combustion products from previous cycles on a timescale capable of establishing the proper phase between the pressure oscillations and the unsteady heat release. Throughout phase III, the heating of reactants and subsequent breakdown of coherent structures into a turbulent flow field results in a rapid increase in the heat release rate due to combustion. This unsteady heat release rate provides the energy required to drive acoustic oscillations and maintain limit cycle operation. Finally, during phase IV the combustion products are blown down through the engine generating forward thrust. This process is shown to occur at a distinct time in the cycle directly after the majority of heat release in the cycle is completed. In reality, this process occurs throughout the cycle whenever the exhaust velocity is positive. This process is included at this point in the cycle because this is when the exhaust mass flow is near the maximum.

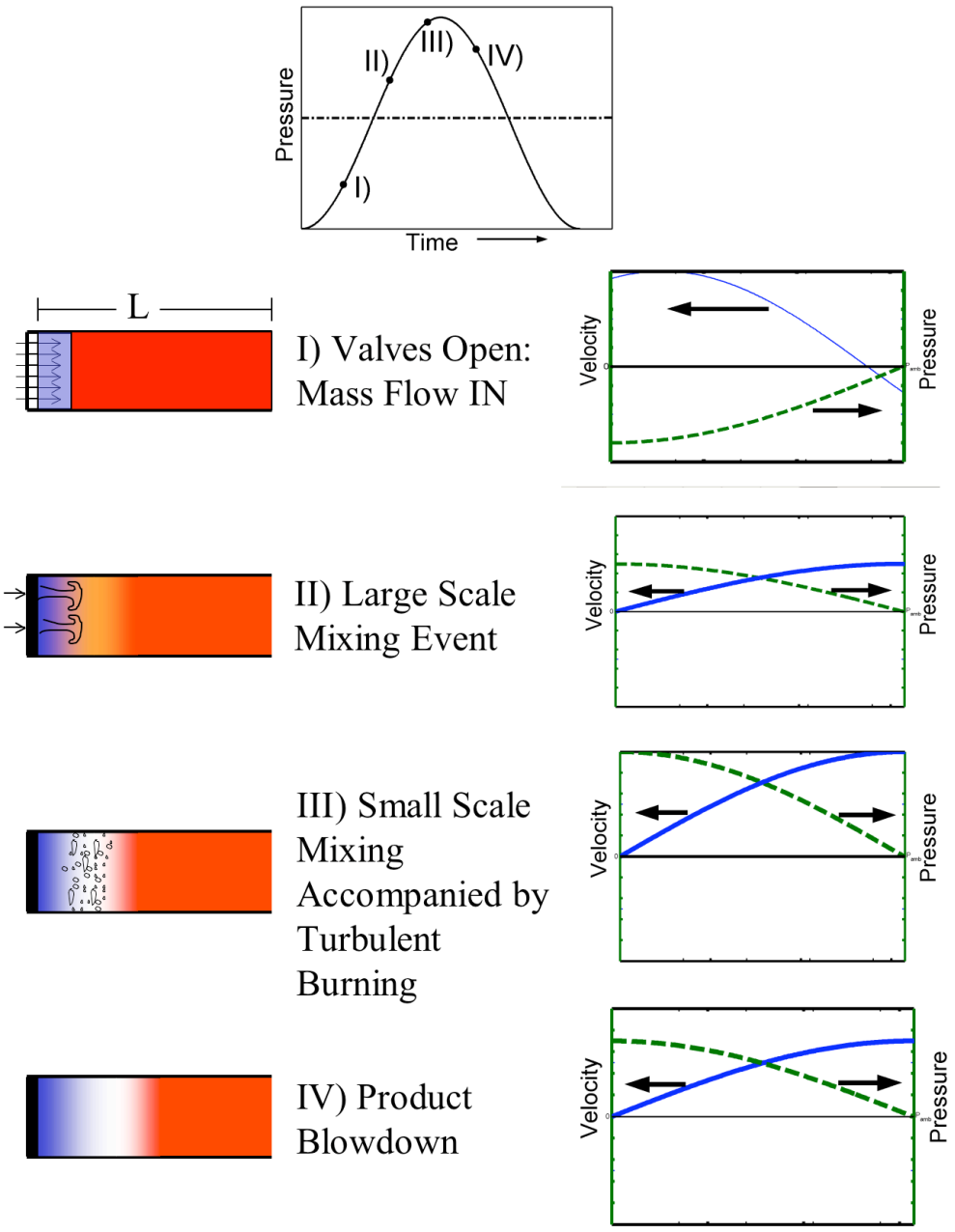

Figure 21: Illustration of important physical processes occurring each cycle accompanied by axial pressure and velocity profiles.

3.2 Formulation

The previous discussion of the details of wave engine operation provides the physical framework for the following modeling approach. The solution approach of this tool is based on the explicit finite differencing of the quasi one-dimensional form of the unsteady conservation equations. Additionally, the mixing processes described in phases II and III of Fig. 21 are modeled with the Linear Eddy Mixing (LEM) model[28]. The one-dimensional LEM model is an accurate and practical model for unsteady mixing that has been successfully applied to detailed studies of turbulent flames[48, 45, 37].

In addition to gas dynamics and mixing, the modeling of unsteady combustion processes is generally viewed as the most difficult aspect of thermoacoustic models, and this investigation examines several different sub-models for calculating reaction rates. The formulation of accurate models for unsteady heat release rates in dynamical systems is exceedingly difficult due to the fact that local heat release rates are extremely sensitive to local conditions such as species concentrations and temperatures. Also, these local conditions are strong functions of both transport processes such as diffusion and turbulent mixing and the reactant consumption rates themselves. The net result is that the global unsteady heat release rates are dependent on a wide range of different length and time scales from chemical reactions, diffusion, and mixing processes. For this modeling approach, diffusion transport is modeled through terms in the conservation equations, and turbulent convection is modeled with a specific application of the LEM model. Considering the thickness of reaction zones for turbulent premixed flames ($\sim 0.175mm$ for stoichiometric CH_4/Air flames), realistic modeling of the thermochemistry requires a very fine spatial resolution when compared with the other length scales in the engine. Since this significantly increases computational expense, a simplified heat release model that requires far less computational resources is examined. While this approach does not capture all of the details of the thermochemistry, it can accurately model large amplitude longitudinal waves with computation times small enough to perform parametric studies with reasonable turnaround times.

3.2.1 Model Equations

The quasi one-dimensional formulation of the conservation equations, which models convection, molecular transport, and the chemical reaction of multi-component perfect gas mixtures, is expressed as follows:

$$\frac{\partial \rho A}{\partial t} + \frac{\partial \rho u A}{\partial x} = 0, \tag{25}$$

$$\frac{\partial \rho u A}{\partial t} + \frac{\partial}{\partial x}\left(A\left(\rho u^2 + P - \tau_{xx}\right)\right) = P\frac{dA}{dx}, \tag{26}$$

$$\frac{\partial E A}{\partial t} + \frac{\partial}{\partial x}\left(A\left(u(E+P) - u\tau_{xx} - k\frac{\partial T}{\partial x}\right)\right) = 0. \tag{27}$$

$$\frac{\partial \rho Y_i A}{\partial t} + \frac{\partial}{\partial x}\left(A\left(\rho Y_i u - D\frac{\partial Y_i}{\partial x}\right)\right) = \dot{m}_i'''. \tag{28}$$

In Eqs. 25-28, ρ, u, P, A, Y_i, and E are the density, axial velocity, pressure, cross sectional area, mass fraction of species i, and total energy per unit volume, respectively. The total energy E is:

$$E = \rho\left(e + \frac{1}{2}u^2\right), \tag{29}$$

where

$$e = c_v T + h, \tag{30}$$

and h and c_v are the local enthalpy of formation and constant volume specific heat for the mixture, defined as:

$$h = \sum_{i=1}^{n} Y_i \bar{h^0_{f,i}}. \tag{31}$$

$$c_v = \sum_{i=1}^{n} Y_i c_{v,i}. \tag{32}$$

In Eqs. 31 and 32, the summation is over all of the individual species i. Furthermore, it is assumed that all species in the mixture behave as thermally perfect gases. Terms containing τ_{xx} model the influence of viscosity on momentum conservation in Eq. 26 and energy conservation in Eq. 27, and τ_{xx} is expressed as:

$$\tau_{xx} = \frac{2}{3}\mu\left(2\frac{\partial u}{\partial x}\right). \tag{33}$$

In Eq. 33, μ represents the dynamic viscosity whose temperature dependence is modeled using Sutherland's formula[49]

$$\mu = \mu_0 \left(\frac{T}{T_0}\right)^{3/2} \frac{T_0 + \varsigma}{T + \varsigma}, \tag{34}$$

with $\varsigma = 111.0$. Axial heat transfer due to conduction and molecular species diffusion is modeled assuming Fourier's law and Fick's law, respectively. The coefficients of thermal conductivity, k, and species diffusivity, D, are calculated assuming

$$k = \frac{c_p}{Pr}\mu, \tag{35}$$

$$D = \frac{\mu}{PrLe} \tag{36}$$

with constant Prandtl and Lewis numbers of 0.72 and 1.0, respectively. Discussed in more detail later, $\dot{m}_i'''$ represents the reaction rate of species i, and hence also determines the heat release due to combustion.

3.2.2 Boundary Conditions

The conditions at the inlet and exhaust boundaries influence wave engine dynamics in two important ways. First, the boundaries reflect acoustic waves propagating throughout the engine, and second, the conditions at the inlet and exhaust boundaries specify the properties of gas entering the engine. Furthermore, since the waveform and amplitude of the pressure waves determine the inflow and mixing of reactants and, thus, unsteady heat release rates, realistic simulation of the boundary conditions is essential to any wave engine model. Following the formulation by Poinsot and Lele[41], inlet and exhaust boundary conditions are calculated using a characteristic representation of the one-dimensional Euler equations. This formulation provides control of wave reflections for all of the physical conditions encountered at the boundaries of the wave engine. The following description of the boundary conditions used in this investigation deals only with the application of this method to wave engine simulations, and the Poinsot and Lele reference should be consulted for a detailed description of the formulation of this method.

Conditions at the inlet are described by two conditions depending on whether the valves are closed or open. When the valves are closed, the inlet is modeled as a perfectly reflecting,

zero velocity solid wall. With this assumption, the inlet pressure and density are calculated with the following characteristic relations:

upstream boundary with closed valves:

$$\frac{\partial \rho}{\partial t} = -\frac{1}{c^2}\left[u\left(c^2\frac{\partial \rho}{\partial x} - \frac{\partial P}{\partial x}\right) + (u-c)\left(\frac{\partial P}{\partial x} - \rho c\frac{\partial u}{\partial x}\right)\right] \tag{37}$$

$$\frac{\partial P}{\partial t} = -(u-c)\left(\frac{\partial P}{\partial x} - \rho c\frac{\partial u}{\partial x}\right), \tag{38}$$

and the temperature is calculated from the perfect gas state equation.

When the flapper valves are open and reactants are injected into the engine, the inlet velocity is determined by the following characteristic relation:

upstream boundary with valves open:

$$\frac{\partial u}{\partial t} = \frac{1}{\rho c}\left(\frac{\partial P}{\partial t} + (u-c)\left(\frac{\partial P}{\partial x} - \rho c\frac{\partial u}{\partial x}\right)\right). \tag{39}$$

Because of the presence of the time derivative of the pressure in Eq. 39, the current inlet velocity depends on the current inlet pressure. Consequently, another equation relating inlet pressure and velocity is required for closure. In this study, the inlet velocity and the pressure gradient across the valves are related by the following expression based on the Bernoulli equation:

$$\triangle P = \frac{1}{2}\xi\rho u^2, \tag{40}$$

where $\triangle P$ is the pressure difference between the stagnation pressure upstream of the valves and the pressure at the valves within the engine. This simplified relationship essentially assumes that the inflow of reactants behaves as flow through an orifice, and it has been applied previously to pulsating combustor simulations[4]. Equation 40 introduces the parameter ξ into the model, which physically represents the resistance of the valves to the inflow of reactants. For example, a larger value of ξ (relative to some reference ξ) requires a larger pressure difference to maintain the same inlet velocity, whereas a smaller ξ requires a smaller pressure difference. A simple iterative procedure is then used to calculate the inlet velocity and pressure that satisfy Eqs. 39 and 40. Using this method, the mass flow into the engine through the inlet is not set a priori, and adjusts itself depending on the current inlet

conditions. The fluid dynamic description of this boundary condition is essentially an orifice flow, but this formulation can also be described as an impedance boundary condition from the perspective of an acoustic wave. A larger ξ value corresponds to a larger impedance, and the limit of $\xi \Rightarrow \infty$ represents an infinite impedance, i.e. a perfectly reflecting wall.

The exhaust boundary condition will initially be modeled as an open, perfectly reflecting pressure release surface (*i.e.*, $P = P_{amb}$). Although the exhaust plane of the engine is always open and contains no valves, two different boundary conditions exist depending on the direction of mass flow. When gases flow out of the exhaust, conditions at the exhaust are known completely by the specified exhaust pressure and the conditions within the engine. The exhaust velocity and density are then calculated using the following characteristic relations:

$$\frac{\partial u}{\partial t} = -\frac{1}{\rho c}\left[(u+c)\left(\frac{\partial P}{\partial x} + \rho c \frac{\partial u}{\partial x}\right)\right] \tag{41}$$

$$\frac{\partial \rho}{\partial t} = -\frac{1}{c^2}\left[u\left(c^2\frac{\partial \rho}{\partial x} - \frac{\partial P}{\partial x}\right)\right], \tag{42}$$

and the temperature is calculated using the perfect gas state equation. On the other hand, during portions of the operating cycle for many operating conditions the momentum of the gases flowing toward the exhaust cannot overcome the adverse pressure gradient in the engine and backflow, or the flow of gas into the engine through the exhaust, occurs. Unfortunately, during backflow, the temperature of the gases flowing in through the exhaust cannot be determined with this modeling tool. Hence, flow conditions must be specified based on other information. Based on results from a study performed by Keller et al.[26] that examined the flow field of oscillating jets, it is assumed in this study that a large portion of gases entering the exhaust during backflow are entrained from ambient gases and not from recently expelled combustion products. Therefore, the backflow gas temperature is assumed to be significantly lower than the products temperature but greater than ambient due to some entrained combustion products. Given the uncertainty inherent in this treatment of the exhaust properties, a parametric study presented later in this thesis will examine the importance of this assumption, but unless otherwise specified, the backflow temperature is assumed to be 650K. With the temperature and pressure specified during

backflow, Eq. 42 is not applicable, and the perfect gas state equation is instead used to calculate the density. Furthermore, to avoid temporal discontinuities in gas properties when the boundary condition changes from exhaust to backflow, the exhaust and backflow conditions are averaged over a small portion of the period during this transition. This insures that the species and temperature gradients remain finite, and the slope of this gradient is chosen such that this transition region from exhaust backflow takes place over no more than twenty percent of the operating cycle period.

3.2.3 Mixing Model

As discussed previously, the turbulent mixing of impulsively injected reactants and combustion products strongly influences the unsteady heat release rates, and therefore the overall performance of the wave engine. Furthermore, since the conservation equations presented above model only convection, molecular diffusion, and wave propagation, a separate sub-model based on the Linear Eddy Mixing (LEM) model is included to incorporate the effects of the formation of coherent fluid structures and turbulence. Turbulent mixing on small scales is a combination of molecular diffusion and turbulent convection, and the one-dimensional LEM model simulates this mixing by treating these two processes separately. Molecular diffusion is modeled through terms in the conservation equations described above, and turbulent stirring is then explicitly modeled with random events that rearrange certain fluid elements at discrete times during the simulation. The overall mixing of reactants and products is then modeled by numerous individual mixing events occurring at different times and locations throughout the combustion chamber. Conceptually, each mixing event represents the rearrangement of fluid parcels by individual turbulent eddies. The size, location, and frequency of these events (eddies) is based on the physical characteristics of the turbulence in the flow field, which must therefore be assumed throughout the simulation. These discrete, random events rearrange fluid elements with instantaneous mappings that increase diffusion by increasing scalar gradients. Several mappings, each with specific properties, have been developed[29, 3] for different types of flows, but this study exclusively uses the 'block inversion' mapping[28], due to its proven ability to adequately model turbulent

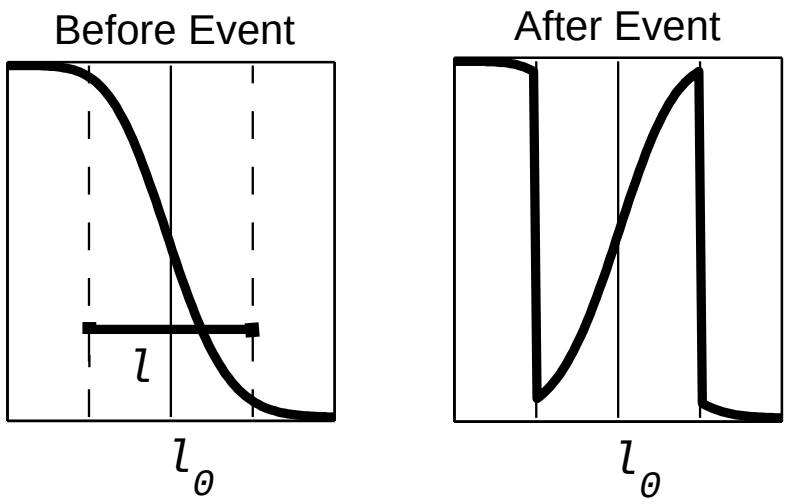

Figure 22: Block inversion of a scalar field with event center located at l_0 and size l.

transport in flows with Reynolds numbers similar to those found in wave engines[3, 28]. Figure 22 illustrates one mixing event modeled with the block inversion mapping to a linear scalar gradient. Figure 22 clearly shows the substantial increase in scalar gradients due to the rearrangement of fluid elements. Once the size and location of the event are prescribed, the mapping exchanges fluid elements from one side of the event center with the corresponding elements from the other side. This is described mathematically by the following expression:

$$\theta(x,t) = \begin{cases} \theta(2l_0 - x, t) & \text{if } l_0 - l/2 < x < l_0 + l/2 \\ \theta(x,t) & \text{otherwise} \end{cases}$$

3.2.3.1 Application of the LEM model to wave engine simulations

For the wave engines modeled in this investigation, the mixing of reactants and products during and after injection is controlled by different length scales. Initially, as reactants are impulsively injected into the combustion chamber, large scale coherent structures form which fold the reactants and products. As Fig. 11 illustrated, at some time after the start of injection, the flow field is dominated by two large, counter-rotating vortices, which eventually break down into intense, small scale turbulence. Although Fig. 11 shows the flow field from a specific combustor, it is generally accepted that similar mixing occurs in many wave

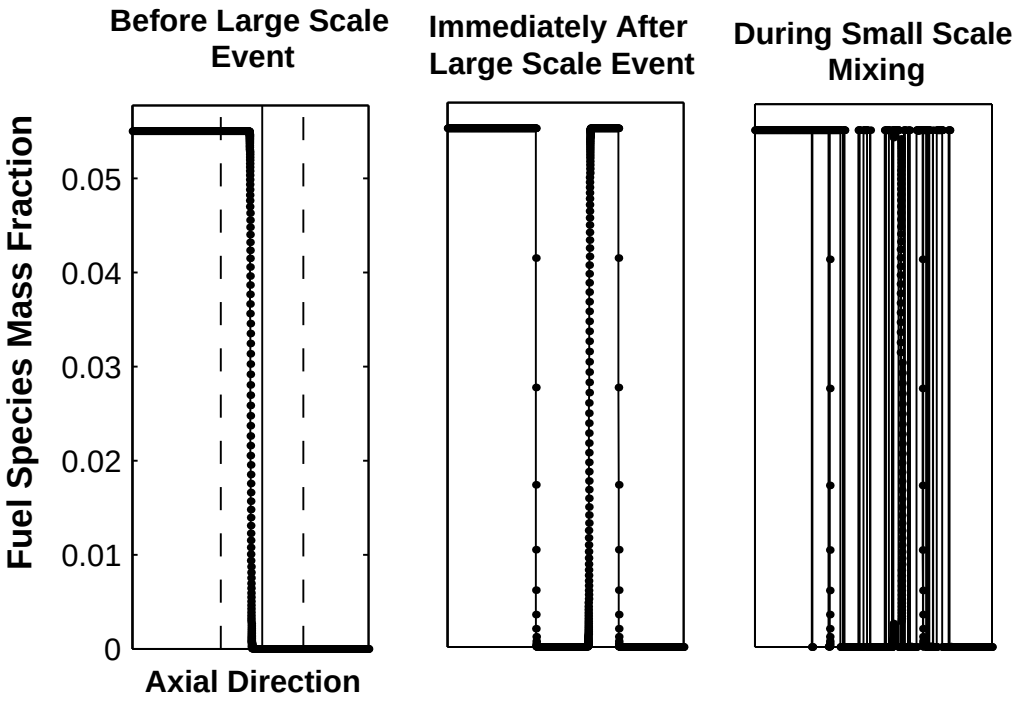

Figure 23: Illustration of two length scale mixing using the LEM model.

engine designs. In general, large coherent structures are necessary to heat the reactants rapidly by significantly increasing the interfacial area between cold reactants and hot products. In addition, intense small scale turbulence is necessary in wave engines to increase the reactant consumption rate. In practice, both scales are required to generate the unsteady heat release rates needed to efficiently drive large amplitude oscillations. Therefore, mixing is modeled on two distinct length scales. First, a large scale mixing event occurs after a specified time lag following the start of injection. This large scale event, modeled as a block inversion mapping located at the interface between the reactants and products, describes the mixing of the initial coherent structure, see Fig. 23.

Small scale mixing ensues throughout the entire combustion chamber immediately after the large scale event, see Fig. 23, and a single turbulent length scale is used to model this small scale mixing. Although in reality small scale mixing occurs across a range of length scales, both engineering models[3] and detailed studies[48] of moderate Reynolds number flow fields have been successful in accurately simulating the behavior of turbulent premixed

flames using only one length scale (i.e., eddy size). For single length small scale mixing, the event frequency per unit length, λ, is determined by[48]

$$\lambda(x,t) = \frac{C_1 \nu Re}{L_{small}^3}, \tag{43}$$

where $Re = u_{rms} L_{int}/\nu$ and ν, L_{int}, L_{small}, and C_1 are the kinematic viscosity, integral scale of the turbulence, small scale event size, and an adjustable model constant, respectively. Therefore, the time interval between events is given by $\Delta t_{stir} = 1/(\lambda x_{comb})$ where x_{comb} is the combustor length. Finally, the location of each event is determined by uniformly sampling the λ distribution in the axial direction. Additional in-depth discussions of many aspects of the LEM model can be found in the references cited above, and the above discussion should serve only as a brief exposition of this subject matter.

3.2.4 Heat Release Models

Heat release is modeled in two ways. The first model, called the chemical kinetic model, calculates reaction rates using the following well known eight species, four reaction methane/air mechanism[40]:

$$CH_4 + 2H + H_2O \rightleftharpoons 4H_2 + CO \tag{44}$$

$$H_2O + CO \rightleftharpoons H_2 + CO_2 \tag{45}$$

$$2H + M \rightleftharpoons H_2 + M \tag{46}$$

$$3H_2 + O_2 \rightleftharpoons 2H + 2H_2O. \tag{47}$$

Details of this mechanism, such as reaction rate coefficients are omitted here for brevity. These values can be found in Packzo et al.[40]. Reaction rates for the individual species in this reaction mechanism are calculated using CHEMKIN[23]. While this finite rate model of chemical kinetics can calculate realistic physical characteristics of methane air flames such as flame thickness and laminar consumption rate, the attainment of accurate results requires very high spatial resolution, which significantly increases computation cost.

The second heat release model, called the simplified consumption model, assumes that the characteristic mixing and heating time between injected reactants and hot combustion

products from the previous cycles most strongly influences the heat release rates found in wave engines as well as many unsteady combustion systems. Therefore, if overall reaction rates are determined by mixing rates, then the details of the finite rate chemical kinetics are not necessary to reasonably predict overall heat release rates. While the previous finite rate chemical kinetics calculations required the inclusion of minor species such as H, H_2, and CO, the simplified consumption model requires only the major species, namely CH_4, O_2, CO_2, H_2O, and N_2. Based on a previous study of wave rotors by Nalim and Paxson[38], the following expression for the reaction rate of methane is used:

$$\dot{m}'''_{CH_4} = -\kappa \rho Y_{CH_4}[1.0 - T_{ign}/T] \qquad \text{for T} > T_{ign}. \tag{48}$$

The reaction rate model described by Eq. 48 assumes zero methane consumption below a specified ignition temperature. As shown in Figure 24, the simplified consumption model for the reaction of fuel broadens the temperature dependence of the reaction rate compared to the more realistic Arrhenius expression that assumes an exponential temperature dependence. The simplified consumption model therefore produces laminar flames which are significantly thicker than actual flames. The result of this is a decrease in the resolution needed to reasonably model flame structures. However, since overall consumption rates are dominated by mixing characteristics rather than chemical kinetics, it is hypothesized that this simplification will not strongly effect performance prediction capabilities of the developed model. To test this hypothesis, a comparison of these two reactant consumption models is performed and presented later in this thesis.

3.2.5 Numerical Implementation

The conservation Eqns. 25-27 were discretized and numerically integrated using a time accurate explicit MacCormack predictor-corrector scheme[2]. This scheme, which solves Eqns. 25-27 for all interior grid points, is second order accurate in both time and space. In terms of the generalized variables $\mathbf{U}$ and $\mathbf{F}$, the predictor step is:

$$\overline{\mathbf{U}_i^{n+1}} = \mathbf{U}_i^{\overline{n}} - \frac{\Delta t}{\Delta x}\left(\mathbf{F}_{i+1}^n - \mathbf{F}_i^n\right), \tag{49}$$

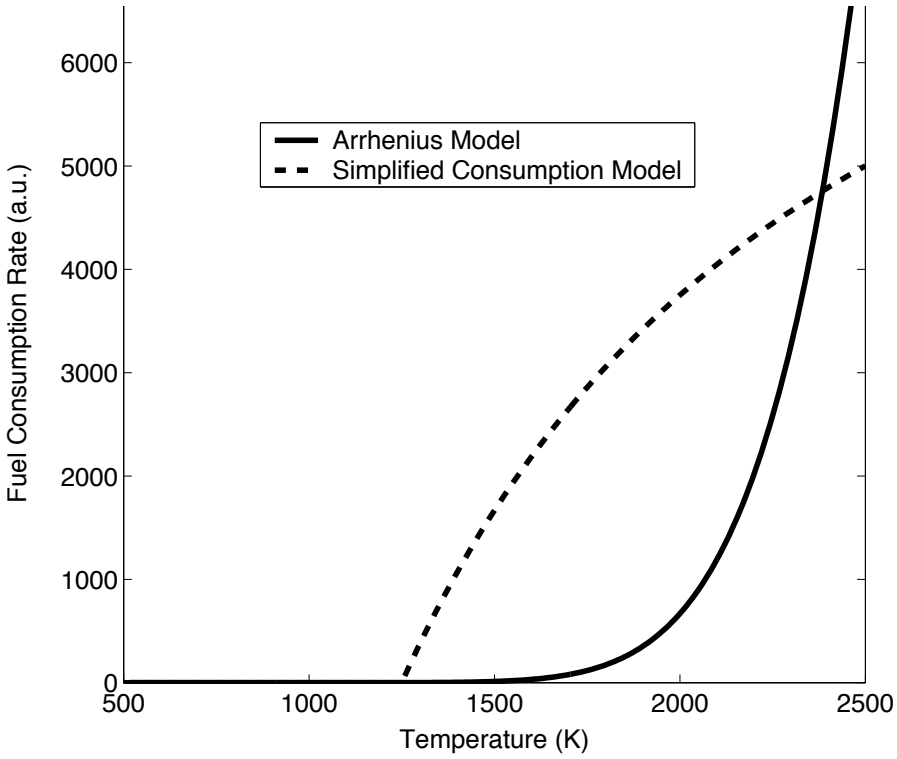

Figure 24: Temperature dependence of simplified consumption model and Arrhenius fuel consumption rates.

and the corrector step is:

$$\mathbf{U}_i^{n+1} = \frac{1}{2}\left[\mathbf{U}_i^n + \overline{\mathbf{U}_i^{n+1}} - \frac{\Delta t}{\Delta x}\left(\overline{\mathbf{F}_i^{n+1}} - \overline{\mathbf{F}_{i-1}^{n+1}}\right)\right], \tag{50}$$

For the wave engine model equations developed previously, the vectors $\mathbf{U}$ and $\mathbf{F}$ are

$$\mathbf{U} = \begin{bmatrix} \rho A \\ \rho u A \\ E A \\ \rho Y_{sp_j} A \end{bmatrix}, \tag{51}$$

and

$$\mathbf{F} = \begin{bmatrix} \rho u A \\ A\left(\rho u^2 + P - \tau_{xx}\right) - P\frac{dA}{dx} \\ A\left(u(E+P) - u\tau_{xx} - k\frac{\partial T}{\partial x}\right) \\ A\left(\rho Y_i u - D\frac{\partial Y_i}{\partial x}\right) - \dot{m}_i^{'''}. \end{bmatrix}. \tag{52}$$

During the predictor-corrector time marching, additional calculations are performed in order to calculate the temperature dependence of the specific heat of the gas mixture. Figure 25 displays the temperature dependence of the constant pressure specific heats for several of the major species over the range of temperatures commonly found in the wave engine. The curves in Fig. 25 were generated using the commonly used curve fit coefficients based on experimental observation[20] and display a significant variation in gas properties as a function of temperature. Since nitrogen is heated from 300K to greater than 2000K and methane (CH_4) is typically injected into the engine at temperatures around 300K and is heated to 700-800K before combustion, the large variation in specific heats in Fig. 25 indicates that the temperature dependence of specific heats should be accounted for in the calculations. This temperature dependence eliminates the calorically perfect assumption used for all previous simulation results, as well as introducing an additional complication to the calculations. Using a thermally perfect assumption, the gas mixture properties are a function of the temperature, yet the temperature is also a function of the gas properties through the conservation of energy. Therefore, at each time step, a gradient method based iterative scheme is applied in order to calculate the actual temperature.

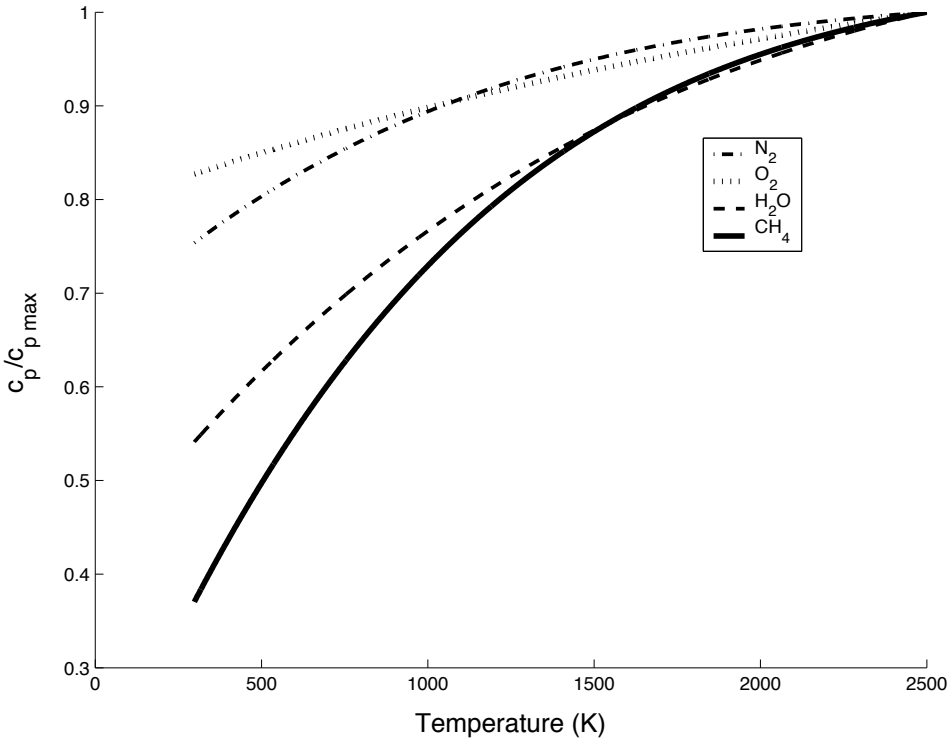

Figure 25: Temperature dependence of constant pressure specific heats for major species.

The following fourth order artificial smoothing function is also used to prevent the formation of high frequency numerical oscillations near large spatial gradients:

$$-\frac{\varphi}{8}\left(\mathbf{U}_{i+2}^{n}-4\mathbf{U}_{i+1}^{n}+6\mathbf{U}_{i}^{n}-4\mathbf{U}_{i-1}^{n}+\mathbf{U}_{i-2}^{n}\right). \tag{53}$$

These gradients arise as a result of both the highly unsteady nature of the heat release rate and the steepening of large amplitude oscillations due to gas-dynamic nonlinearities. Furthermore, for all simulations performed in this investigation, $0 \leq \varphi \leq 1.0$, and given this function is fourth order accurate, it does not affect the formal accuracy of the solver.

The grid spacing of the discretized conservation Eqns. 25-27 must adequately resolve the smallest length scale modeled in a given simulation. For example, when a simplified heat release model is used, the smallest length scale is typically the mixing model eddy size, which then determines the grid spacing. On the other hand, since the length scale of flame structures when using an eight species finite rate chemical mechanism to model the heat release is much smaller than even the mixing length scales, typically of the order of 0.1mm, the grid spacing must resolve these structures to accurately model heat release. Additionally, since these small length scales are limited to the combustion chamber, a simple grid transformation is used in order to increase the number of grid points in the combustion chamber and reduce the number of grid points in the tailpipe of the engine. Following [2], the grid transformation requires the re-formulation of the conservation equations in terms of transformed variables, $\overline{x}$ and $\bar{t}$, which are given by

$$\bar{t} = t \tag{54}$$

$$\overline{x} = \begin{cases} x & x \leq L_{c.c} \\ 1 + \frac{1}{\tanh(\varepsilon)} \tanh\left(\varepsilon\left(\frac{x}{(L-L_{c.c})} - 1\right)\right) & L_{c.c} \leq x \leq L \end{cases} \tag{55}$$

As Eq. 55 shows, in order to simplify the implementation of the LEM model, a uniform grid spacing is used within the mixing and combustion chamber. The constant ε in Eq. 55 determines the spacing of the physical points within the hyperbolic tangent framework. It is chosen such that the distance between the first two physical points in the tailpipe region is almost the same as the distance between the last two points in the combustion chamber, and this constant is found using a simple iteration procedure. The conservation equations

in vector form expressed in terms of $\overline{x}$ and $\overline{t}$ become

$$\frac{\partial \mathbf{U}}{\partial \overline{t}} + \frac{d\overline{x}}{dx}\frac{\partial \mathbf{F}}{\partial \overline{x}} = 0, \tag{56}$$

where $\frac{d\overline{x}}{dx}$ is computed numerically at each point. Figure 26 shows an example of the grid stretching used in this investigation where the upper figure represents the physical grid, x, and the lower figure represents the computational grid, $\overline{x}$. In addition to the implementation of the grid transformation, the code was parallelized using the common Message Passing Interface (MPI) to allow more reasonable simulation times for cases modeling detailed chemical kinetics. The implementation of MPI for the detailed chemical kinetic simulations had no effect on the results, and as discussed later, the majority of the results presented in this thesis were generated using the simplified consumption model for unsteady heat release. Therefore the computational expense was significantly decreased to the point where all simulations were completed using a single processor. Hence, the details on the parallelization of this modeling tool will be omitted for brevity.

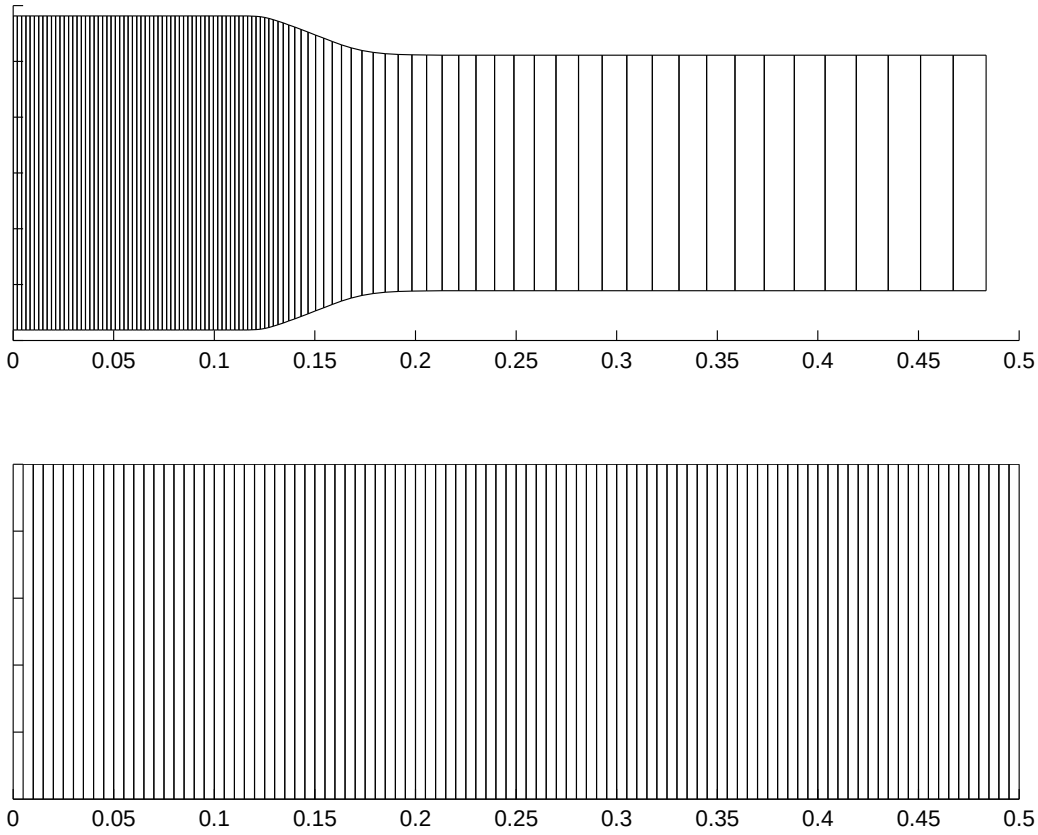

Figure 26: Illustration of grid transformation.

CHAPTER IV

INITIAL NON-REACTING AND REACTING FLOW WAVE ENGINE SIMULATIONS

The previous chapter presented the formulation of the wave engine modeling tool used for the remainder of this investigation. Given that one primary characteristic of this modeling tool is the ability to perform parametric investigations of the influence of operating conditions on overall performance, several of the sub models developed for this tool are reduced order representations of complex physical processes. Therefore, before presenting results from parametric studies of full wave engine simulations, it is necessary to examine the validity of some of the key assumptions behind the implementation of the inlet and exhaust boundary conditions and the sub models. This chapter explores these assumptions by presenting results from several simplified scenarios that isolate these key assumptions. Cold flow, or non-reacting simulations are presented first to confirm that this modeling tool is capable of reproducing results similar to the previously validated Galerkin method technique. Results from this cold flow investigation also explore the differences between externally forced oscillations in closed systems similar to the previous acoustic resonators and closed-open ducts that more closely approximate the boundary conditions found in wave engines. In addition to non-reacting simulations, the remaining results presented in this chapter concentrate on the assumptions related to the reacting flow portions of the modeling tool. A comparison and validation of the unsteady heat release models as well as the formulation for future thrust calculations is presented in order to clearly define the performance metrics for full wave engine simulations. Finally, this chapter explores the influence of the assumptions behind the exhaust boundary condition on overall wave engine performance.

4.1 Non-Reacting Simulations

Two simplified non-reacting cases are discussed to show that this modeling tool can effectively simulate the influence of gas dynamic nonlinearities on driven oscillation properties. Similar to the acoustic resonators previously modeled using the Galerkin method technique, the first non-reacting simulation examines driven oscillations in a closed/closed, 0.3m long straight duct filled with 300K air. The second non-reacting simulation replaces one of the closed ends with an open end (i.e. pressure release boundary condition) to more closely approximate the boundary conditions found in the wave engine. While this case remains closely related to the previously discussed acoustic resonator example driven at the single frequency by small amplitude forcing at the boundary and the absence of mean flow through the duct, it will be shown that the pressure release boundary condition significantly influences the driven oscillation properties. The final non-reacting simulation examines the influence of the flapper valves on an unforced flow field subject to an initial disturbance. The purpose of this simulation is to investigate the role of the inlet flapper valves in the dissipation of acoustic energy when they are used to control the flow of fresh reactants into the engine.

4.1.1 Closed/Closed Systems

For this case, the straight duct is held stationary while a piston at one end is oscillated sinusoidally with a maximum displacement of 1.2mm at 561.67 Hz, corresponding the fundamental natural acoustic frequency of the chosen configuration. The pressure at the piston face for these conditions is displayed in Fig. 27. Figure 27(a) describes three limit cycle pressure oscillations extracted from Fig. 27(b) showing the shock waves resulting from waveform steepening. Hence, this indicates that the chosen numerical solution approach technique is capable of describing the nonlinear gas dynamic processes resulting from the generation of large amplitude waves similar to those encountered in the previous study using the Galerkin method.

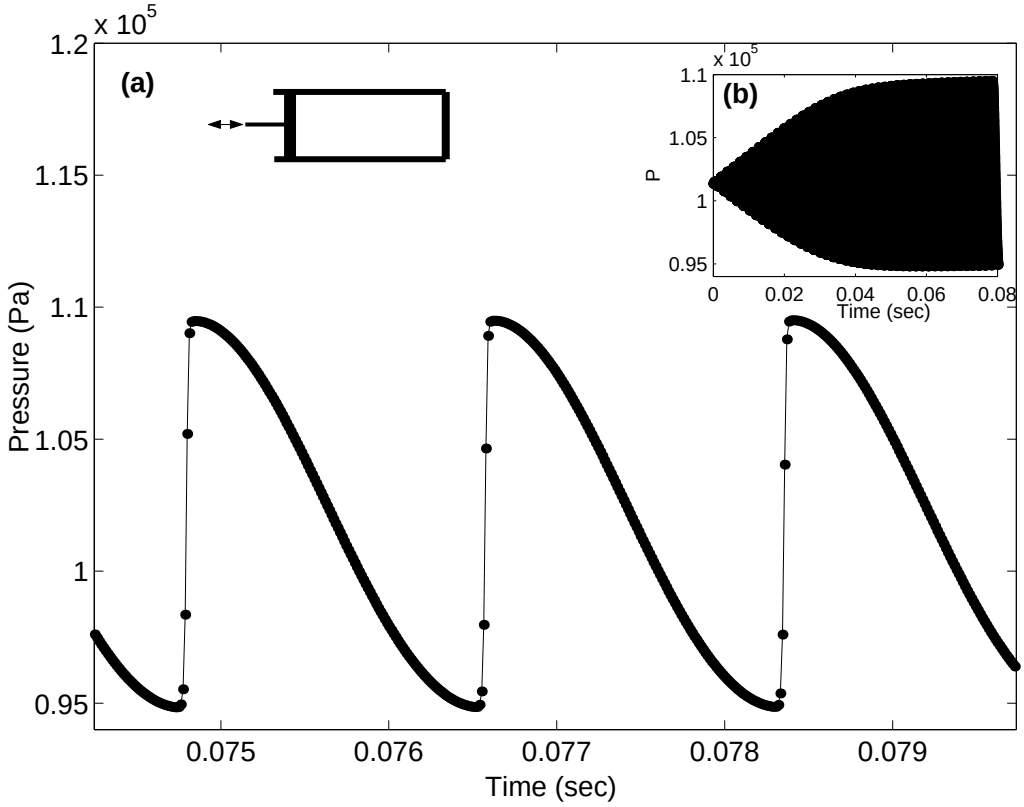

Figure 27: Piston forced oscillation within a closed 0.3m long straight duct. (a) details three limit cycle oscillations extracted from (b).

4.1.2 Closed/Open Systems

The forcing for the closed/open system is the same as in the previous case, with a solid piston oscillating at a prescribed frequency and no mean velocity in the duct. The difference between this case and the previous case is that the closed end has been replaced by an open pressure release surface. Furthermore, for this example, the duct length is 0.5 meters long because this length corresponds to the wave engine length modeled in future reacting flow studies. Figure 28 shows the predicted pressure amplitude at the piston for a forcing frequency of 165Hz, which corresponds to the maximum amplitude response of driven oscillations for this duct. The waveform of the pressure oscillations does not exhibit the same sawtooth shape as seen in the closed/closed example, but the pressure oscillation envelope shown in Fig. 28(b) exhibits the same growth and saturation as the closed/closed acoustic resonators. Furthermore, Fig. 29 describes the frequency content of the piston face pressure oscillations. While the temporal pressure trace provides qualitative evidence of waveform distortion resulting from the transfer of acoustic energy from the driven frequency into harmonics by gas dynamic nonlinearities, the spectrum of this signal compared to the closed/closed case reveals that a significantly lower portion of the acoustic power resides in the harmonics.

The final non-reacting simulations performed in this investigation examine the dynamics of the previously discussed mechanical flapper valve boundary condition. The engine used in this study is comprised of a 0.3m long straight duct with mechanical flapper valves controlling the inflow and an open pressure release boundary at the exhaust. For this study, an initial pressure pulse is supplied to three wave engines with different flapper valve characteristics filled with atmospheric air at 300K. This disturbance evolves in time with no external forcing and no unsteady heat release. Due to the absence of heat release and the perfectly reflecting outflow boundary condition, the energy in this initial disturbance dissipates only through convective losses and the flapper valves. Figure 30 shows the time dependence of pressure and velocity at the flapper valves. The spatial dependence of the initial pressure disturbance is a quarter cosine wave, corresponding to the fundamental acoustic mode of a closed-open duct, with a maximum pressure amplitude of 120% the

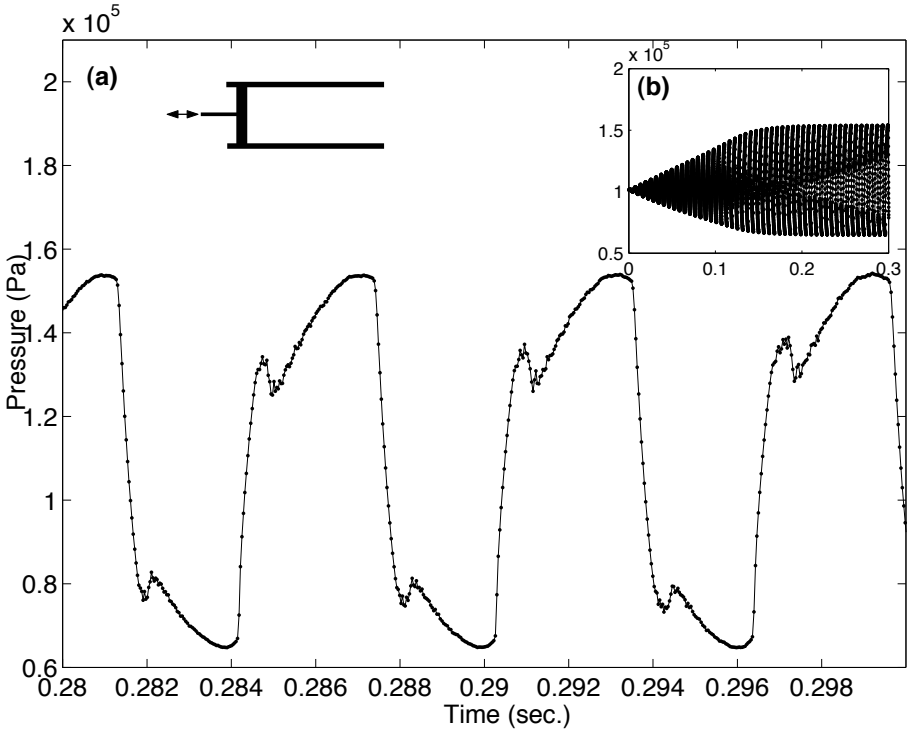

Figure 28: Piston forced oscillation within a closed 0.5m long straight duct with open pressure release boundary condition. (a) shows detailed limit cycle oscillations extracted from (b).

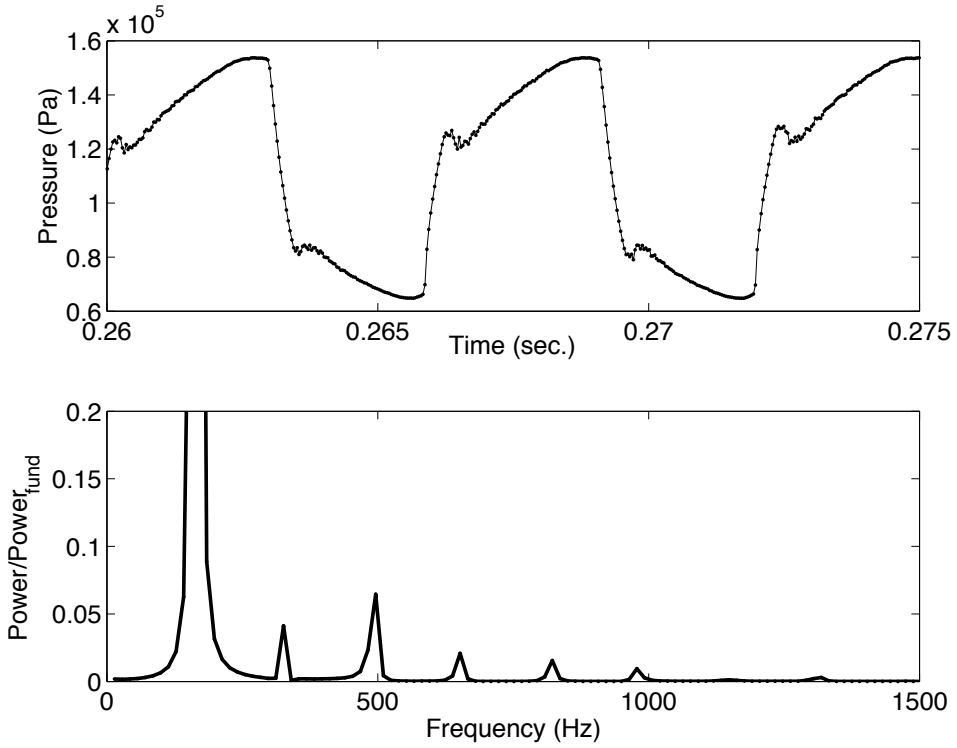

Figure 29: FFT of limit cycle pressure oscillations at the piston face for the straight duct Closed/Open system.

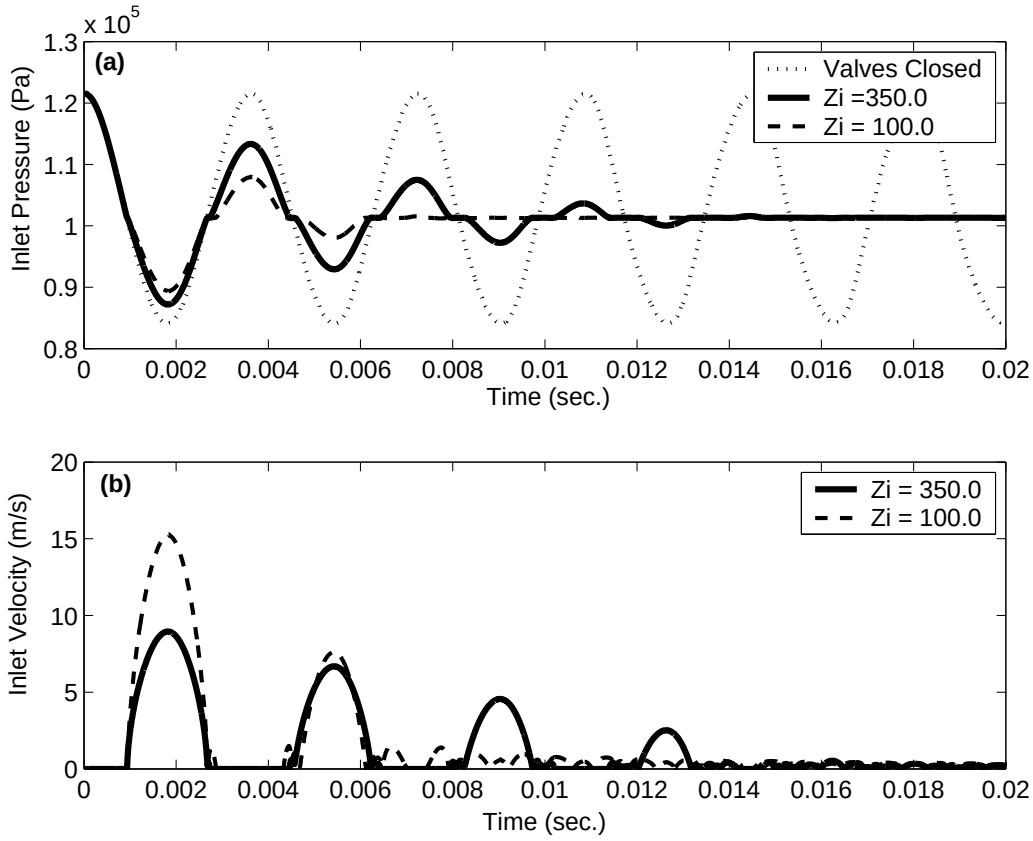

Figure 30: Inlet pressure and velocity traces for nonreacting cold flow conditions and several values of the flapper valve parameter ξ.

upstream pressure of 1.01kPa. Figure 30 shows three cases with identical initial conditions corresponding to three different flapper valve characteristics. The dotted line in Fig. 30 (a) describes the time dependence of the inlet pressure when the flapper valve remains closed for the duration of the simulation (i.e. $\xi \rightarrow \infty$ from Eq. 40). As a result, the amplitude of the oscillation does not change appreciably and there is no mass flow through the valves. The remaining two cases show that as ξ is decreased, the dissipation of acoustic energy increases while more reactants flow into the engine. The comparison of these two cases illustrates an important tradeoff in the design of inlet valves for wave engines. The reactants injected into the engine provide the chemical energy for the unsteady heat release that drives the oscillations, therefore maximizing the mass of reactants injected each cycle maximizes the available driving energy. Yet, the results from Fig. 30 show that increasing the mass of reactants injected into the engine also increases the dissipation of oscillation energy. Since the basic operating principle of the wave engine extracts energy from the oscillations in order to inject fresh reactants which drive the next cycle, results from this cold flow valve study suggest that an optimal valve design exists that balances losses and driving to maximize oscillation energy, and thus thrust generation.

4.2 Reacting Flow Results

The primary objective of this section is to investigate the influence of different heat release models on such simulation characteristics as runtime and ease of implementation as well as predicted engine performance. Additionally, this comparison also elucidates the relationship between mixing, acoustic, and reaction timescales. First, results from the heat release model based on finite rate chemical kinetics are presented. While this heat release model is more physically realistic, these simulations require either significant computational resources or a large amount of time, thus negating the positive aspects of using a one-dimensional model. The following study investigated a comparison of different heat release models applied to the same model problem. This comparison shows that the simplified heat release model captures many of the essential wave engine physical processes while reducing simulation times by over an order of magnitude. The final portion of this investigation

presents a validation of the simplified heat release model by comparing simulation results with experimental measurements.

4.2.1 Detailed Chemical Kinetics Simulation Results

A 0.5m long wave engine at stationary, sea level conditions is used for the first reacting flow simulation using the detailed chemical kinetic mechanism for the calculation of reactant consumption rates. The reactants, consisting of a premixed stoichiometric mixture of methane and air, are injected through the inlet flapper valves characterized by a resistance parameter, ξ, of 55.0. The large scale mixing event is assumed to be ten percent of the combustion chamber diameter. Figure 31 describes the predicted time dependence of the inlet pressure and velocity for several cycles of operation. The vertical lines in Fig. 31 denote instants when the large scale mixing event takes place as well as the time for the start of small scale turbulent stirring events. Figure 31 shows that for the proper timing of large and small scale mixing, this modeling tool can simulate self-sustained finite amplitude oscillations without an external source of ignition and without a priori specification of the unsteady heat release rate within the combustion chamber.

The timing and duration of large and small scale mixing events for this simulation were chosen based on an experimental study of vortex driven combustion instabilities[42]. Figure 32, showing a Schlieren image taken in this investigation, clearly shows one large scale vortex formed during the unsteady injection of premixed reactants into a multiple inlet dump combustor. Other Schlieren images presented in this study proceed to capture the subsequent breakdown of this coherent structure into smaller scale turbulence. Using measured C_2 radical emission and spark-Schlieren images, it has been concluded that vortex formation begins when the dump combustor inlet velocity reaches a maximum, and the vortex is subsequently convected downstream while growing in size. Additionally, the large coherent vortex structures begin to breakdown as the amplitude of the combustor pressure oscillation becomes positive. The overall result of this process is a significant increase in unsteady heat release rate and the sustained driving of acoustic oscillations within the combustor.

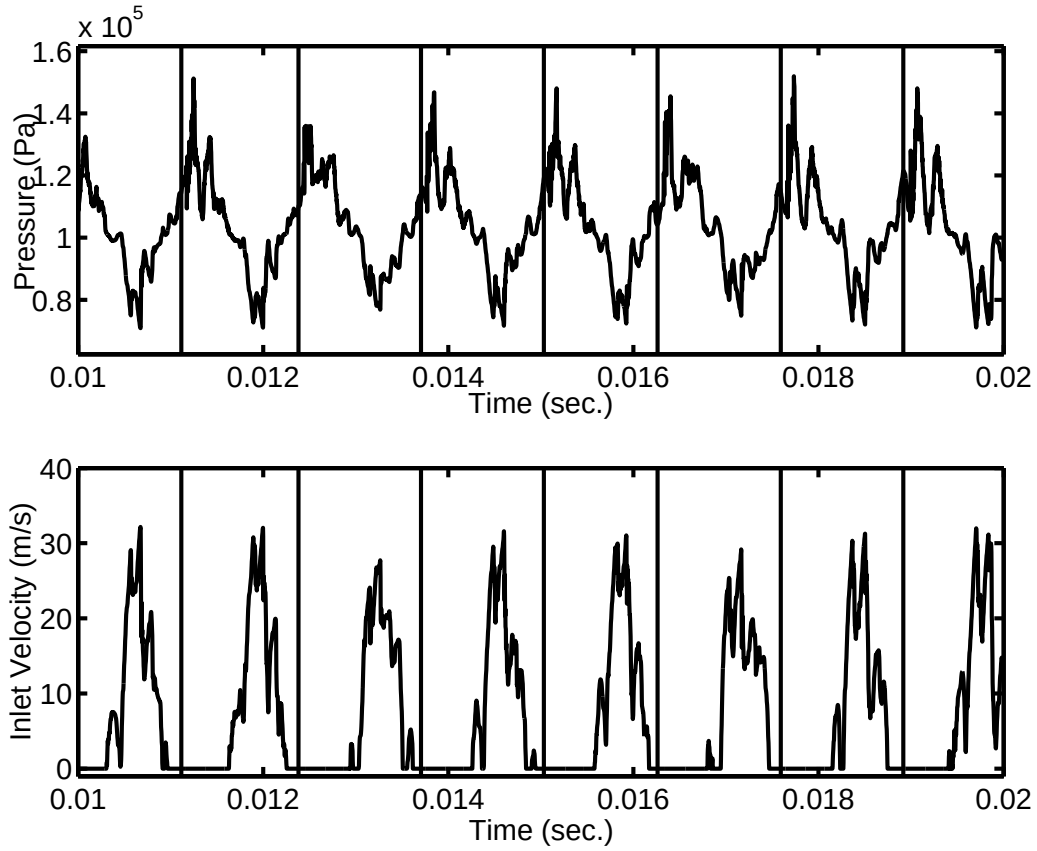

Figure 31: Inlet pressure and velocity for a reacting flow wave engine simulation using a detailed chemical kinetic mechanism.

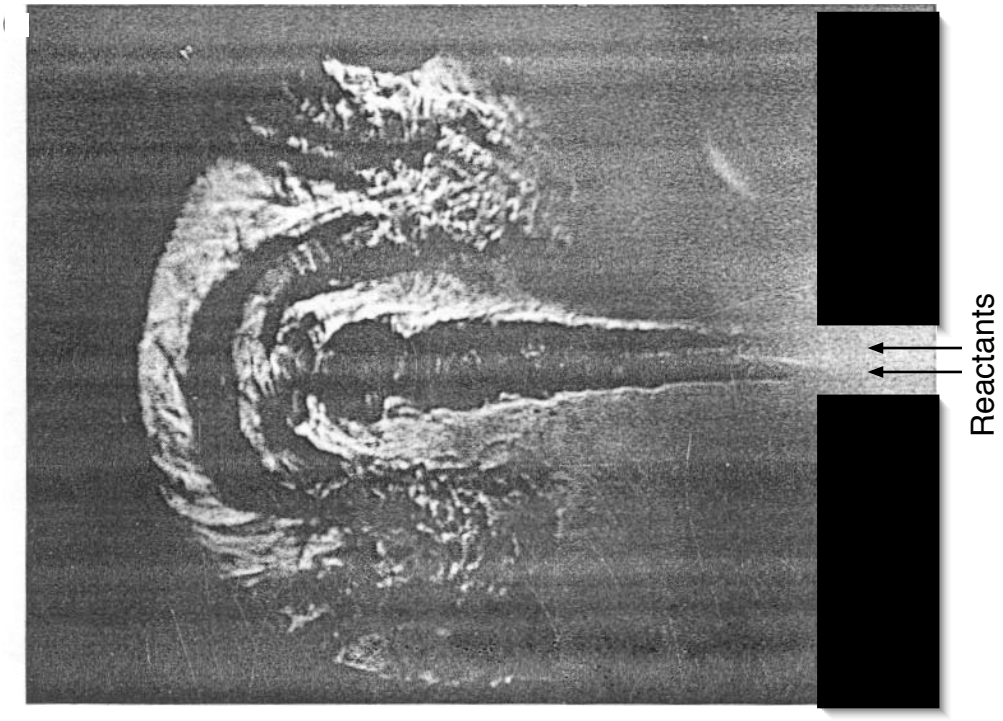

Figure 32: Experimental Schlieren image of large vortex formed during the unsteady injection of premixed reactants into a dump combustor. Taken from Poinsot et al.[42]

The total heat release within the combustion chamber at a given time is obtained by integrating the local heat release, $q(x,t)$, over the length of the engine:

$$Q(t) = \int_0^L q(x,t)dx. \tag{57}$$

Figure 33 shows the time dependence of the pressure and overall heat release a quarter of one engine length downstream from the inlet. The relative phase between the heat release rate and combustor pressure at this location shows that a significant amount of heat release each cycle is occurring during the time of elevated chamber pressure, thus satisfying Rayleigh's criterion and providing the necessary driving to maintain limit cycle behavior. Under typical conditions, the inlet velocity profile, which promotes the formation of coherent vortices, is in phase with the pressure oscillations, and the formation time of these vortices provides the proper time lag for this phase difference between heat release and pressure oscillations. The predicted unsteady heat release shown in Fig. 33 exhibits large spikes coincident with the large scale mixing event followed by a significant drop off in heat release immediately afterwards. This temporal dependence of heat release differs from measured heat release presented in many experimental studies of vortex driven combustion instabilities, and the large spike and subsequent dropoff suggest that the relationship between the large scale mixing properties and small scale turbulent mixing is not being modeled accurately in these simulations. This relationship between mixing model parameters will be investigated in greater detail later, yet nonetheless these simulations capture many of the essential features necessary to drive large amplitude pressure oscillations in unsteady combustion systems.

The importance of large scale vortex formation and breakdown can be examined with this modeling tool through alteration of the mixing model parameters. As an example, consider a wave engine with the same physical dimensions as in the previous case but with a different flapper valve configuration. For this case, the flapper valve geometry was chosen to inhibit the formation of large coherent structures. To model this flapper valve geometry, the large scale mixing event is eliminated while still retaining the smaller scale turbulent mixing. Figure 34 displays the inlet pressure and velocity time history for this configuration.

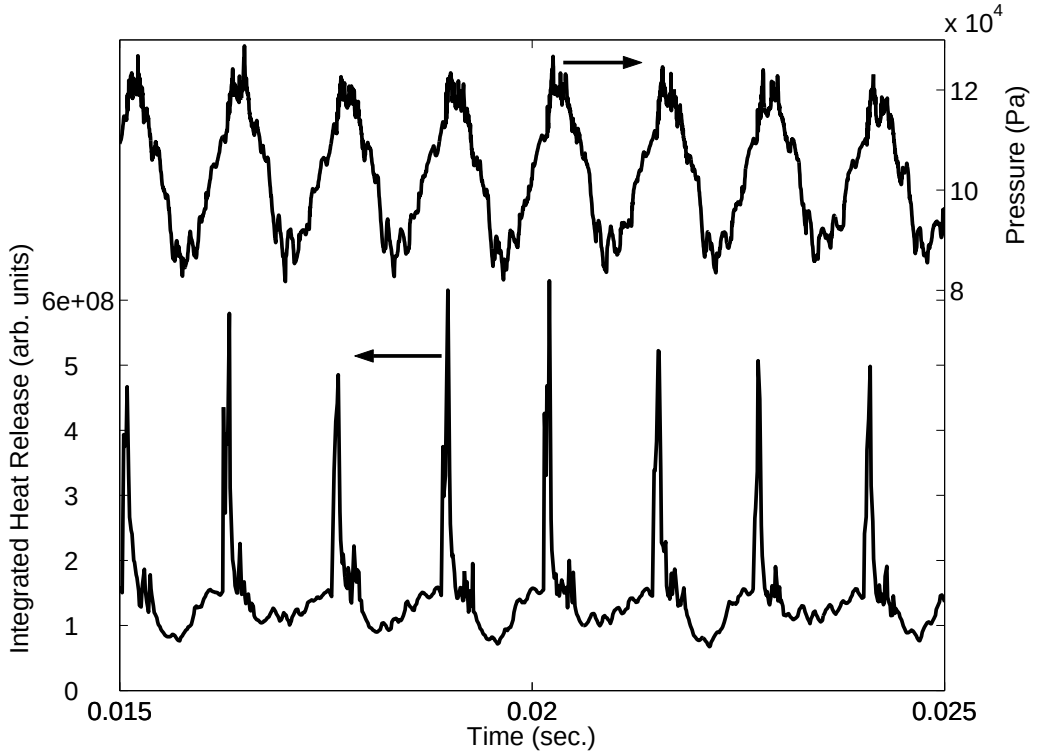

Figure 33: Pressure time history inside combustor (at 0.25*L) in addition to spatially integrated heat release.

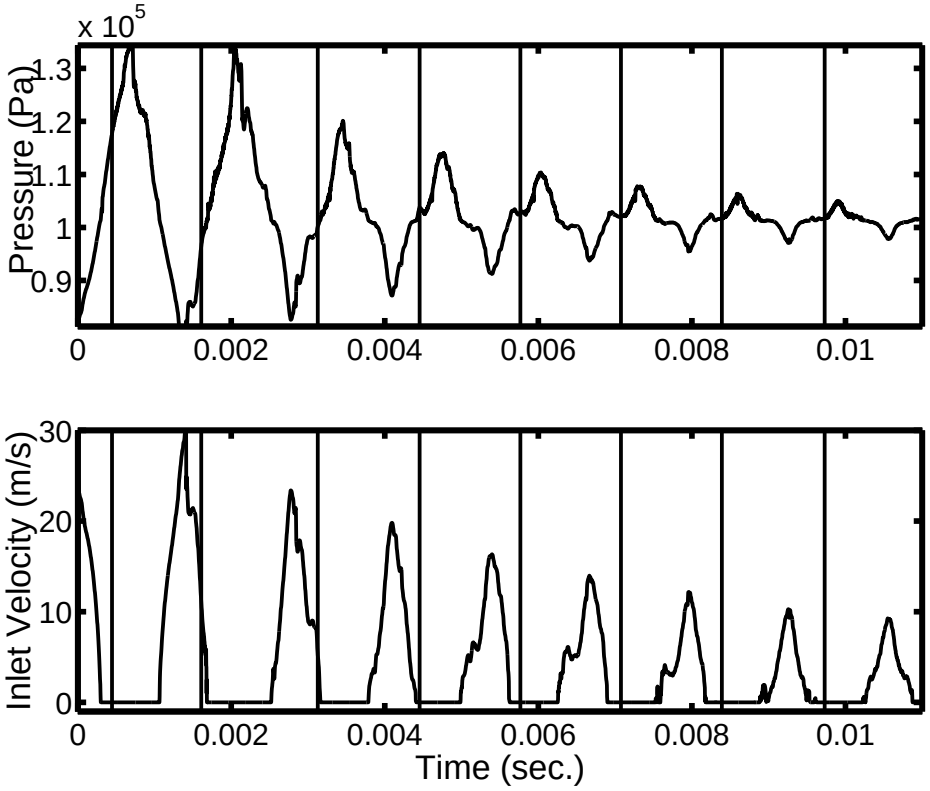

Figure 34: Inlet pressure and velocity values for a reacting flow condition. No large scale mixing event included, therefore vertical lines represent start of small scale mixing.

While the initial conditions for this case are the same as those of the previous case, the results show a steady decrease in the pressure amplitude, suggesting that the driving by the unsteady heat release cannot overcome the losses due to the flapper valves, convective, and viscous losses. Figure 35 presents the pressure and heat release in the same manner as Fig. 33. Figure 35 shows that in the absence of large scale mixing processes, the heat release does not exhibit the same spiking behavior seen in Fig. 33. It is therefore concluded from these results that the spatial and time scales created by the large scale coherent fluid dynamic structures are essential to the establishment of an unsteady heat release profile necessary for limit cycle operation. The spatial length scale of the coherent vortex structures provides the initial distribution of reactants and products that promotes the thorough mixing and heating by the small scale turbulence. Additionally, the coherent vortices also establish a timescale for the unsteady heat release similar to that of the driven oscillations.

The previous simulation using the detailed chemical kinetic heat release model required approximately 400-450 CPU hours to reach periodic operation when run in parallel on a ten CPU intel based cluster. This long simulation time is directly a result of both the number of equations that must be solved at each timestep (11; mass, momentum, energy, and 8 species) and the use of finite rate chemical kinetics model that requires a spatial resolution of ~ 10 grid points per millimeter to resolve flame structures. This resolution is far greater than anything needed to model the other physical processes in this system, and leads to very small time steps in order to satisfy CFL criteria for numerical stability. Unfortunately, while very fine resolution is necessary for the numerical stability of the model, it still does not accurately model the highly multi-dimensional flame structures in a wave engine given that this is still a one-dimensional model. Furthermore, while the reduced eight species mechanism described by Eqs. 26-47 has been shown to reproduce accurate burning rates under certain conditions, the ability of this mechanism to model highly unsteady heat release rates, large local strain rates, and possible extinction and re-ignition events is yet to be determined. Given that a one-dimensional formulation of this system was chosen in order to examine the performance of a wide range of different engine designs rapidly, the use of a finite rate chemical kinetics model reduces this capability considerably by significantly

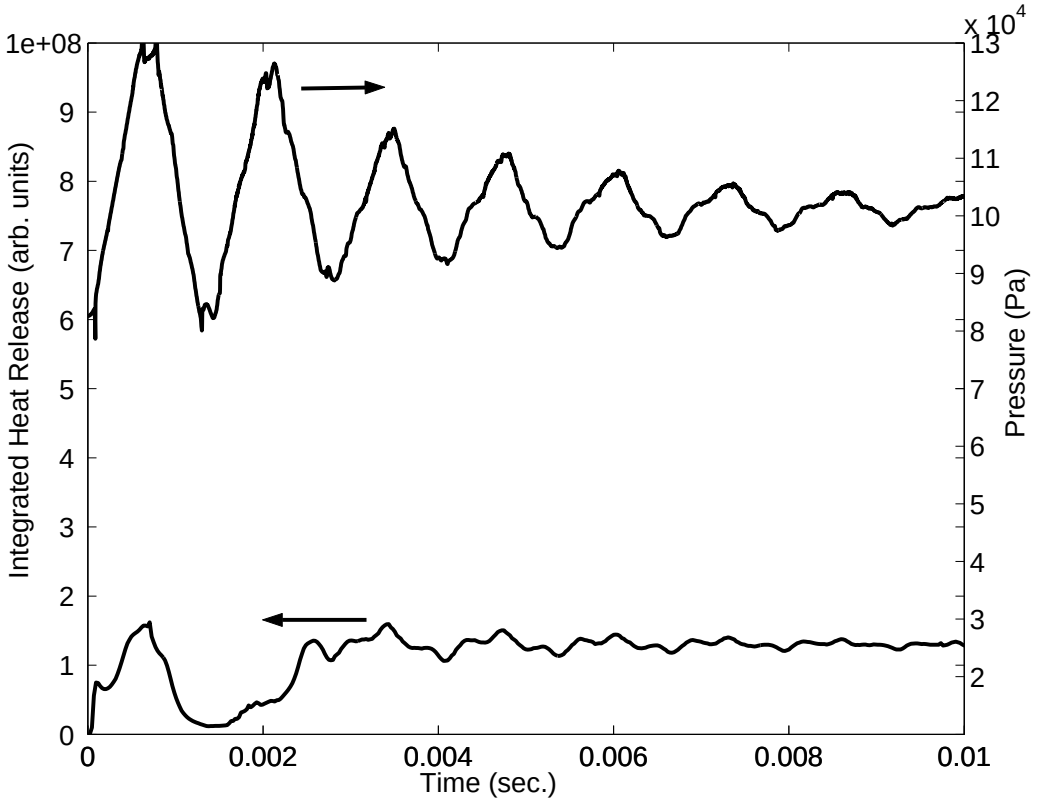

Figure 35: Pressure time history inside combustor (at 0.25*L) in addition to spatial integral of heat release in the absence of a large scale mixing event. Decreasing upstream pressure amplitude suggests that unsteady heat release not large enough to overcome damping processes.

increasing simulation times.

4.2.2 Comparison of Heat Release Models

As discussed previously, unsteady heat release rates in the pulsejet can be modeled ranging in detail from full chemical kinetic calculations to simplified consumption models. Additionally, it was hypothesized that the unsteady heat release rate is more strongly influenced by the characteristics of the mixing between cold reactants and hot combustion products from previous cycles, rather than the details of the chemical kinetics. To examine this hypothesis, one wave engine geometry was simulated with both the chemical kinetic model and the simplified consumption model.

The investigated wave engine was a straight duct 0.3m long and 0.06m in diameter, and the reactants consisted of a premixed stoichiometric mixture of methane and air. Furthermore, both test cases were assumed to be stationary, and the valve inflow resistance parameter, ξ, was set to 47.0 for both cases. The simulations were started with the engine filled with hot combustion products and at a pressure one and a half times the ambient pressure (101kpa), and were run until limit cycle was attained and oscillation properties did not change appreciably from cycle to cycle.

Figure 36 displays the inlet pressure and inlet velocity as well as the total instantaneous heat release rate calculated using both heat release models. The inlet pressure and velocity are very similar for both the detailed chemical kinetics calculations and the simplified heat release model in terms of both maximum amplitude and waveform, with minor differences occurring as the pressure amplitude drops from the maximum. The total instantaneous heat release rates predicted with the two models increase at almost the same rate during the pressure rise, but the detailed chemical kinetic model predicts a more rapid drop off in heat release rate as the pressure begins to decrease. An examination of the individual species present in the combustion chamber through this time shows this drop off occurs because of incomplete carbon monoxide oxidation, which typically requires more time at high temperatures than this cycle allows. Interestingly, incomplete carbon monoxide oxidation is also an important issue in spark ignition engines, which also operate in a periodic manner

similar to the wave engine[20]. Studies of spark ignition engines have shown that carbon monoxide concentrations in postflame combustion products are close to equilibrium levels, yet the burned gases cool considerably during the expansion and exhaust strokes, effectively quenching the the oxidation of carbon monoxide. Figure 37, taken from a study of carbon monoxide chemical kinetics in spark ignition engines, compares the time dependence of kinetic and equilibrium values of carbon monoxide after the completion of combustion. The significantly larger kinetic carbon monoxide levels in Fig. 37 account for this quenching of carbon monoxide recombination. Furthermore, since carbon monoxide oxidation is exothermic, and the simplified consumption model assumes complete oxidation, the calculated heat release rate is larger during this portion of the cycle, as the results in Fig. 36 clearly show. The time integration over one cycle of the heat release rates for the two models shows that the simplified consumption model releases approximately twenty percent more heat than the chemical kinetic model for almost identical reactant flow rate.

Figure 38 displays the total heat release at each spatial location over the entire simulation, thus showing the distribution of heat release throughout the combustion chamber for both the chemical kinetic model and the simplified consumption model. The spatial heat release profile shows the distribution of heat release predicted with the simplified consumption model is more broad than that predicted by the chemical kinetic model as a result of the difference in the temperature dependence of the reaction rates for the two models. Although not appearing to have a large impact on overall performance, the detailed chemical kinetic model predicts larger amplitude small scale fluctuations of the heat release rate, resulting from the nearly exponential temperature dependence coupled with fine spatial resolution.

4.2.3 Simplified Heat Release Model Validation

Results presented from the previous non-reacting simulations validated certain aspects of this solution technique including finite amplitude wave propagation and the behavior of the flapper valves, but it is still necessary to validate the multi-length scale mixing model and heat release rate calculations. Experimental pulse combustor results reported by Keller et al.[25] are used to validate these sub-models. Results from their investigation include a

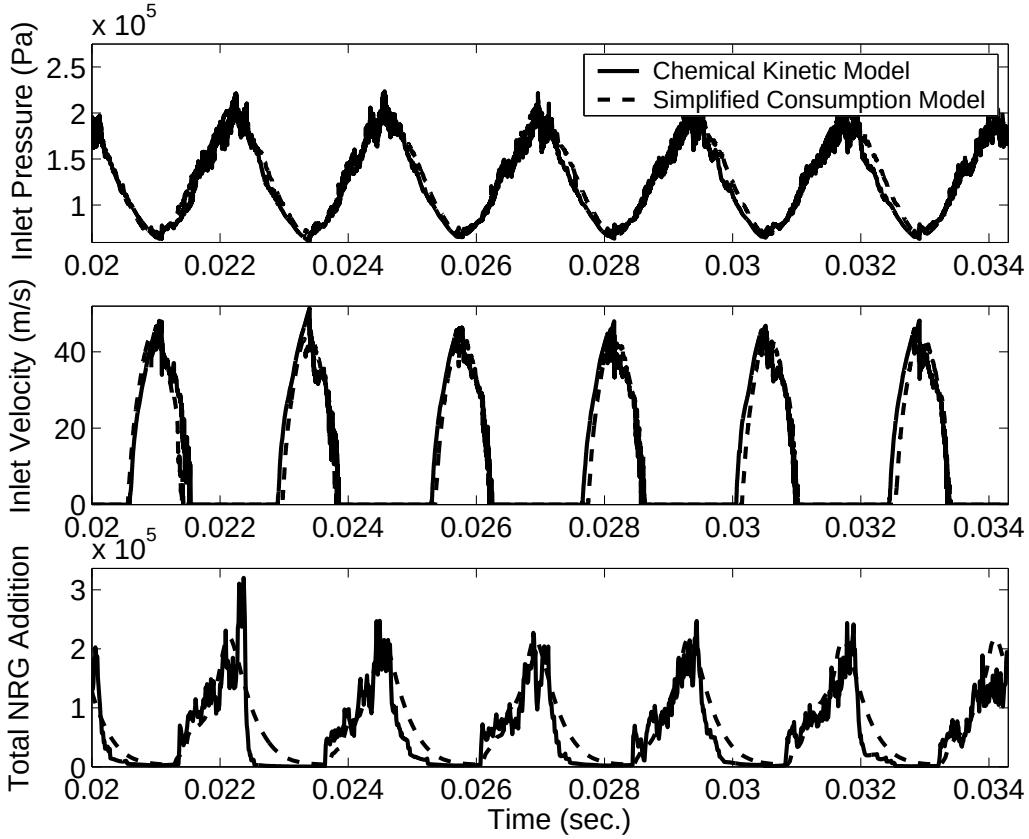

Figure 36: Comparison of inlet conditions and total instantaneous heat release rate using chemical kinetic model and simplified consumption model.

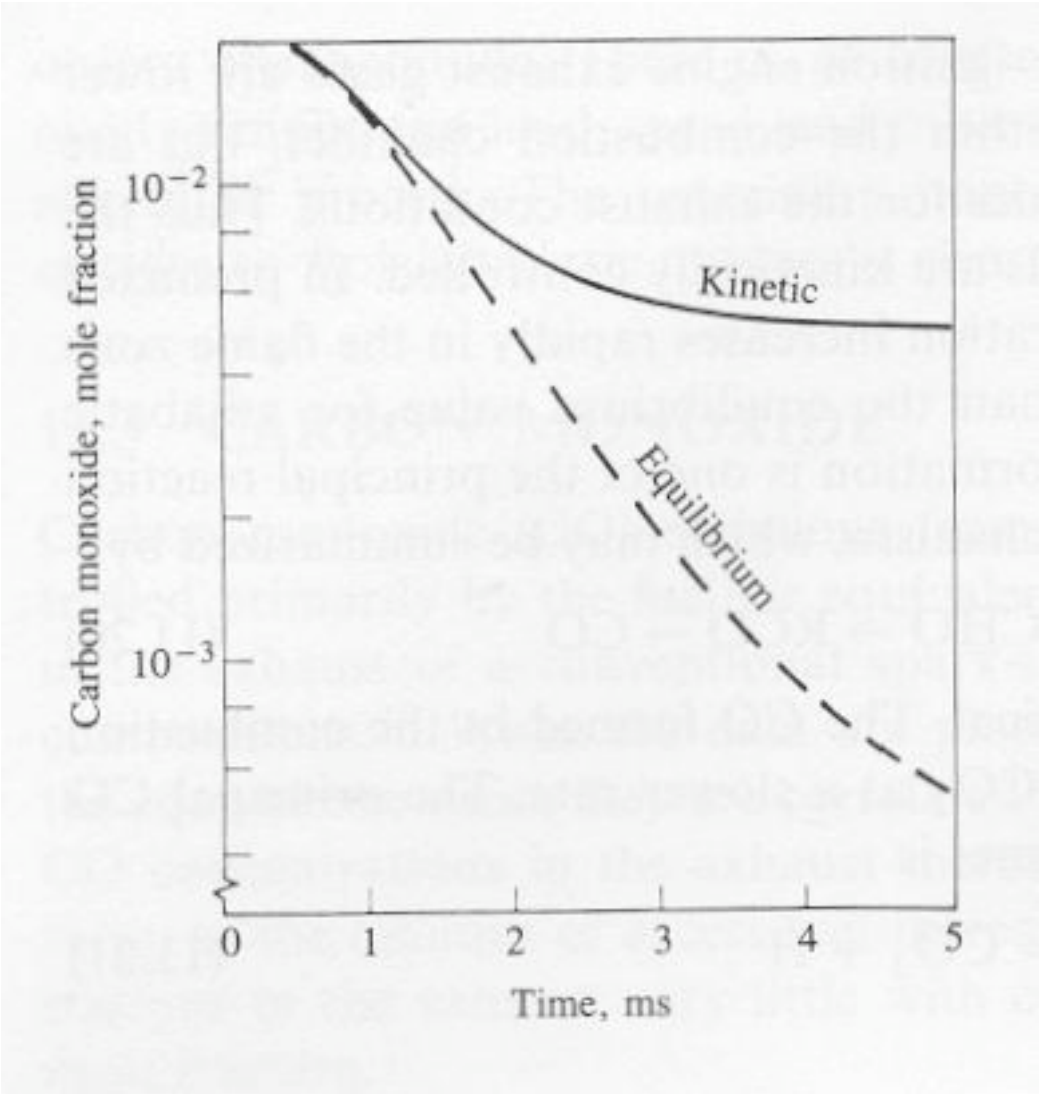

Figure 37: Equilibrium and kinetic carbon monoxide mole fraction as a function of time for a typical spark ignition engine cycle. Taken from Heywood[20]

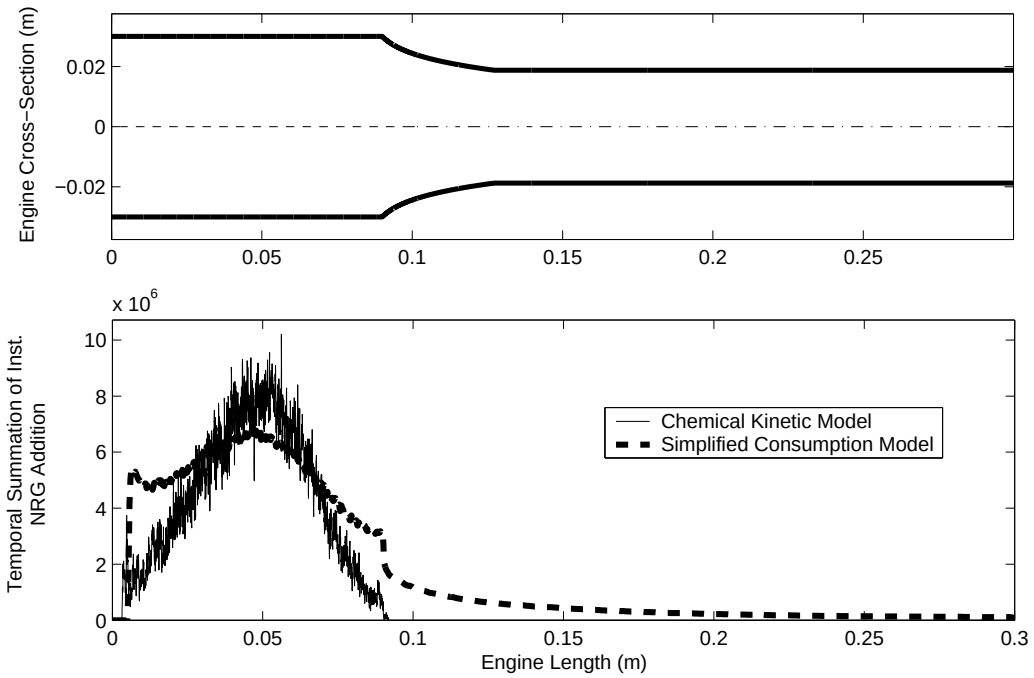

Figure 38: Spatial heat release distribution from chemical kinetic model and simplified consumption model.

detailed physical schematic of the device, total instantaneous heat release through $< OH^* >$ chemiluminescence measurements, and instantaneous pressure within the combustion chamber. The following procedure was used in this validation study. First, the geometry of the experimental pulse combustor was input into the model. The entire system was approximately 1.1m long with the combustion chamber comprising ten percent of the total length. In addition, the diameter of the combustion chamber was twice the diameter of the tailpipe. Next, the timing of the large scale event in the model was obtained from the reported heat release results. Although no specific information about the characteristics of the mixing processes was reported, the timing of the large scale mixing was estimated based on the start of the sudden increase in the heat release rate. The simulation was then run while adjusting the flapper valve resistance parameter (ξ) to obtain the reported mass flow rate of 9.0 g/s. For the following validation study, the simplified consumption model was used to calculate local instantaneous heat release rates. Based on results displayed in Fig. 11 of a similar experimental pulse combustor, the size of the large scale event was estimated

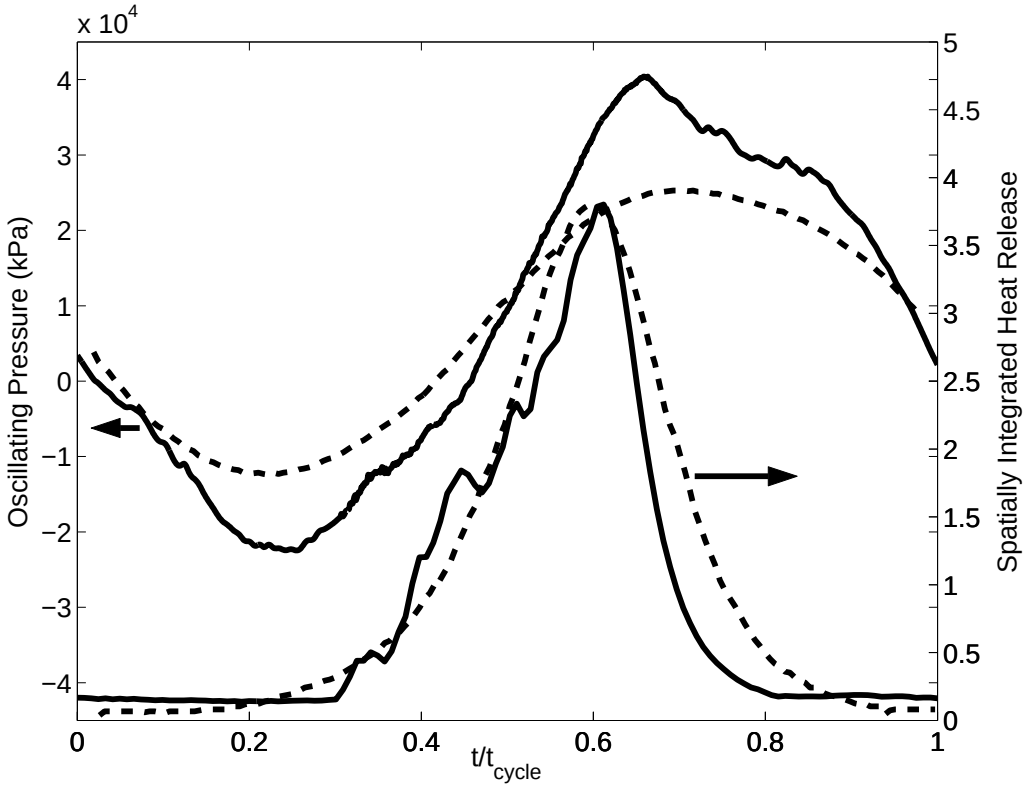

Figure 39: Comparison of model results with experimental pulse combustor data reported in Keller et al.[25]. - - - Experimental results; — Model prediction. No acoustic radiation from open exhaust end. $\xi = 2800$.

to be ninety percent of the combustion chamber diameter, and the small scale event size was assumed to be three percent of the large scale event. These estimates, while more of a heuristic starting point than a detailed validation, are assumed to capture the essential physics necessary to reasonably predict the unsteady heat release rates in this device.

The results in Figure 39 compare predicted pressure and heat release rates with experimental data for one cycle. This comparison shows that while the predicted maximum pressure amplitude is larger than the experimental results, the overall waveforms of the two pressure traces are similar. Additionally, while the maximum pressure amplitudes of the experimental results are slightly larger than 25% of the mean, the waveform of both the experimental and model results are nearly sinusoidal. This observation, in light of the previous investigation into the dominating influence of gas dynamic nonlinearities on driven oscillations in acoustic resonators, suggests that the self excited forcing of the system by

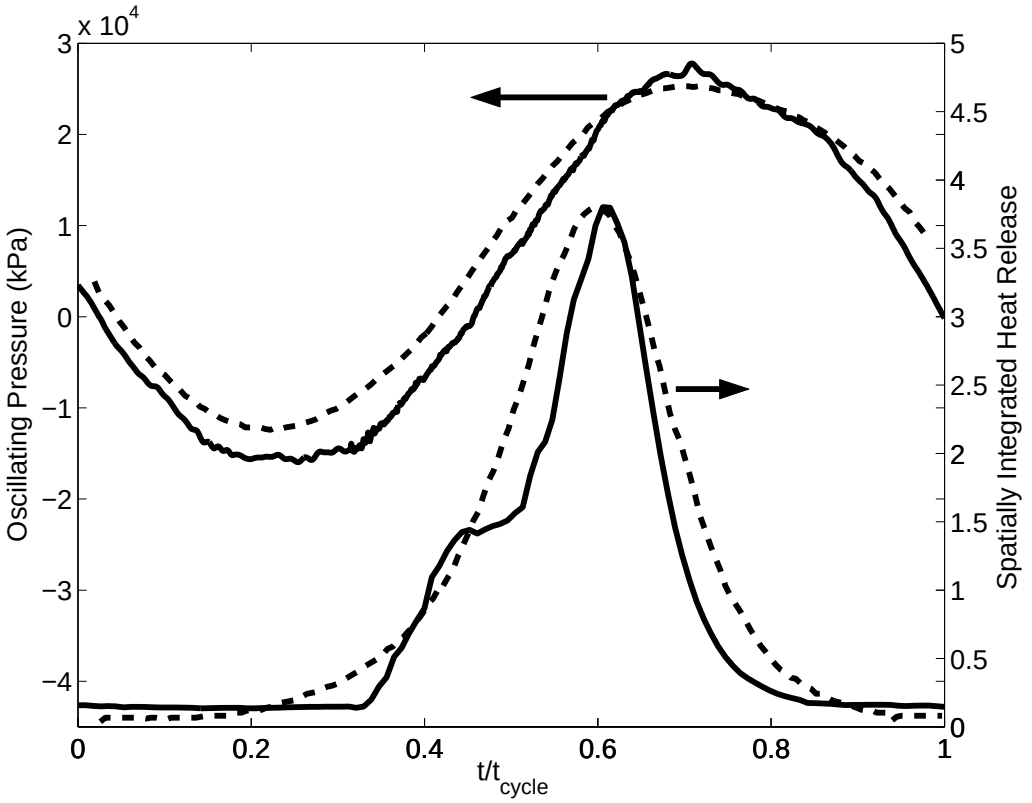

Figure 40: Comparison of model results with experimental pulse combustor data reported in Keller et al.[25]. - - - Experimental results; — Model prediction. 6% acoustic radiation from open exhaust end. $\xi = 2500$.

unsteady heat addition plays an important role in the determination of oscillation waveforms. The comparison of experimental and predicted heat release rates also shows that the model qualitatively captures the time dependence of the total instantaneous unsteady heat release rate, thus suggesting that the flow field can be reasonably described by one large scale representing the coherent toroidal vortex formation and one length scale for the smaller scale turbulent mixing.

One explanation for the over-prediction of maximum pressure amplitude is that this model does not account for acoustic radiation losses at the open exhaust. In reality, it is unlikely that the large pressure oscillations generated in this device would reflect from the exhaust plane with no loss of acoustic energy, thus leading to the loss of some portion of the acoustic energy each cycle. Given that the characteristic based implementation of the exhaust boundary condition provides a means of controlling acoustic radiation losses at the

exhaust plane, this hypothesis can be investigated in order to examine the effect of acoustic losses on overall pressure waveforms. Figure 40 shows a comparison of the same experimental results with simulation results including the addition of acoustic radiation loss from the exhaust plane. A comparison of experimental and predicted pressure oscillations shown in Fig. 40 illustrates that the inclusion of acoustic losses at the exhaust plane brings the predicted results even closer to the reported experimental results in terms of both maximum pressure amplitude and waveform. The frequency of operation of the experimental pulse combustor was 106Hz while the model predicted an operating frequency of 127Hz. Given that the wave engines investigated in this thesis are all less than half the total length of this pulse combustor system, a detailed investigation into the root cause of this operating frequency difference is not warranted for this validation. Nonetheless, it is hypothesized this difference is attributed to the fact that this model does not account for heat losses in the tailpipe region that reduce the temperature of the combustion products in the tailpipe. This decrease in tailpipe gas temperature decreases the local speed of sound resulting in a lower operating frequency.

4.3 Calculation of Thrust and Specific Fuel Consumption

For a large portion of the remaining studies, the average thrust generated and the specific fuel consumption are the metrics used to assess the influence of engine parameters on overall performance. Unlike thrust calculations for rockets and jet engines, the calculation of thrust from a wave engine requires the inclusion of several time dependent terms as well as the treatment of reverse flows. This section describes the assumptions and equations used in this study to calculate thrust from simulation results.

4.3.1 Thrust Calculation Formulation

In order to calculate the thrust generated by a stationary wave engine, we will use a control-volume analysis based on the control-volume illustrated in Fig. 41. For the following analysis, the flow of fuel into the system is assumed to have a negligible effect on the overall thrust, hence it is ignored. Thrust is calculated using the following integral form of the

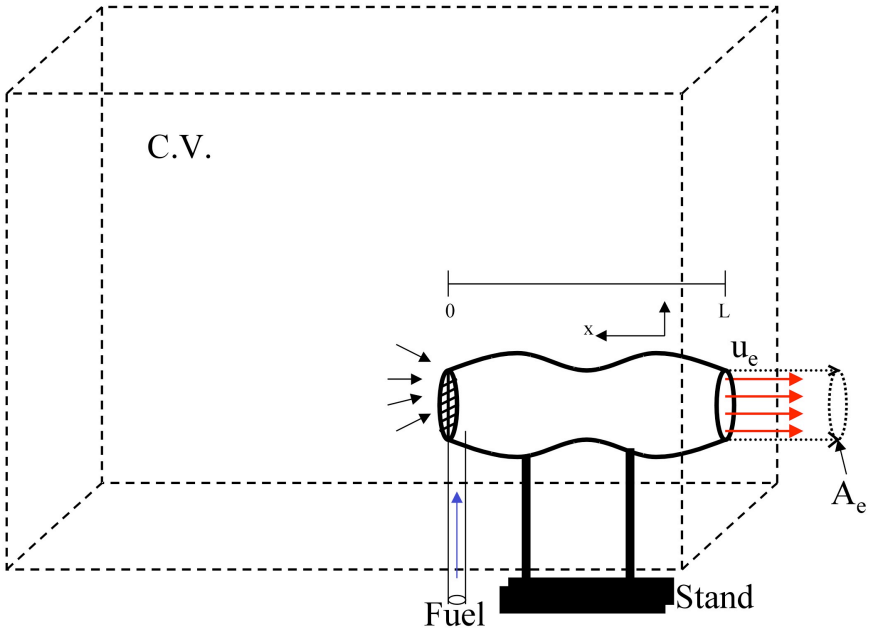

Figure 41: Stationary wave engine with control volume used to calculate thrust.

unsteady momentum equation[15]

$$\frac{\partial}{\partial t}\oint_V \rho\mathcal{U}dV + \oint_S \rho\mathcal{U}(\mathcal{U}\cdot\mathbf{n})dS = A_e(P_a - P_e) + \Theta_i, \tag{58}$$

where ρ, $\mathcal{U}$, A_e, P_a, P_e, and Θ_i are the density, velocity, cross-sectional area of the engine exhaust plane, ambient pressure, exhaust pressure, and instantaneous thrust, respectively. The first term in Eq. 58 is the rate of change of momentum within the control volume and the second term in Eq. 58 is the flux of momentum across the control surface. The first term on the R.H.S of Eq. 58 represents the pressure force on the entire control surface. Furthermore, the wave engine simulations in this investigation assume a perfectly reflecting exhaust boundary condition, hence the pressure at the exhaust is equal to the ambient pressure. Therefore, this term is always equal to zero. The average thrust generated by a wave engine is the time integration of the instantaneous thrust over a given time interval

divided by the time interval itself:

$$T_{ave} = \left(\frac{1}{\tau}\right)\int_0^\tau \Theta_i dt = \left(\frac{1}{\tau}\right)\left[\int_0^\tau \frac{\partial}{\partial t}\oint_V \rho\mathcal{U}dV + \int_0^\tau \oint_S \rho\mathcal{U}(\mathcal{U}\cdot\mathbf{n})dSdt\right]. \tag{59}$$

In order to have periodic operation, the volume integral on the R.H.S of Eq. 59 must be zero, leaving

$$T_{ave} = \left(\frac{1}{\tau}\right)\int_0^\tau \oint_S \rho\mathcal{U}(\mathcal{U}\cdot\mathbf{n})dSdt. \tag{60}$$

At this point, consider only the forces in the axial direction and assume the control-volume exists such that the velocities at the control surface are negligible everywhere except at the engine exhaust. Therefore, the instantaneous and average thrust equations can then be rewritten as

$$\Theta_x = \frac{\partial}{\partial t}\oint_V \rho u dV + \oint_{A_e} \rho u(u\cdot\mathbf{n})dA \tag{61}$$

$$T_{ave_x} = \left(\frac{1}{\tau}\right)\int_0^\tau \oint_{A_e} \rho u(u\cdot\mathbf{n})dAdt. \tag{62}$$

This investigation also uses the Specific Fuel Consumption (SFC) as a metric of performance, as it is a common metric used in determining the performance of air-breathing propulsion systems and is defined as the mass flow rate of fuel into the engine divided by the thrust produced at that fuel flow rate. For this investigation, the instantaneous SFC is not considered, but rather the average SFC, which can be expressed in the following form:

$$\overline{SFC} = \frac{\overline{\dot{m_{fuel}}}}{T_{ave_x}}, \tag{63}$$

where

$$\overline{\dot{m_{fuel}}} = \left(\frac{1}{\tau}\right)\int_0^\tau \dot{m}_{fuel}dt. \tag{64}$$

4.3.2 Positive Exhaust Outflow

For the portion of the cycle in which combustion products are expelled from the exhaust, the calculation of thrust is straightforward. By assuming the velocity profile of the exhaust plane is uniform and the rate of change of momentum inside the control volume but outside of the engine is negligible, the instantaneous and average thrust equations take the form

$$\Theta_x = \frac{\partial}{\partial t}\int_0^L \rho u A dx + \rho_e u_e^2 A_e \tag{65}$$

$$T_{ave_x} = \left(\frac{1}{\tau}\right) \int_0^\tau \rho_e u_e^2 A_e dt. \tag{66}$$

4.3.3 Backflow

The pressure gradient within the engine is negative for a portion of every cycle, and if this gradient is large enough to overcome the momentum of the mean flow of gases out of the exhaust, the exhaust velocity becomes negative and gas is drawn into the engine through the exhaust plane. When backflow occurs, the wave engine acts as a sink for surrounding gases, at which time it is assumed that virtually no thrust is produced because a large portion of the momentum of the incoming gases resides in the radial and tangential directions.

4.3.4 Example

Figure 42 illustrates the time dependence of the different terms in Eq. 65 for several cycles in the operation of a typical wave engine. The impulse, calculated with Eq. 66, for this example is 93.0 N, while the total instantaneous thrust can exceed 1600 N, thus showing the highly unsteady nature of the thrust production for the wave engine. Figure 42 also shows the instantaneous rate of change of momentum within the control volume, but this term integrates to zero over every periodic cycle and therefore contributes zero to the average thrust per cycle.

4.4 Exhaust Boundary Condition Investigation

The previous discussion on the representation of the exhaust boundary condition in the wave engine model noted that backflow enters the wave engine through the exhaust plane for many typical engine operating conditions. Consider Fig. 43, which illustrates two instances during one cycle of operation. Due to the mixing of exhaust combustion products with ambient air, the composition and temperature of the backflow is determined by the characteristics of the mixing between the exhaust plume of combustion products created during blowdown and the ambient air. Given the highly unsteady nature of the flow field downstream of the exhaust, it is not possible to quantitatively determine the composition and temperature of the backflow gases without the use of experimental measurements or

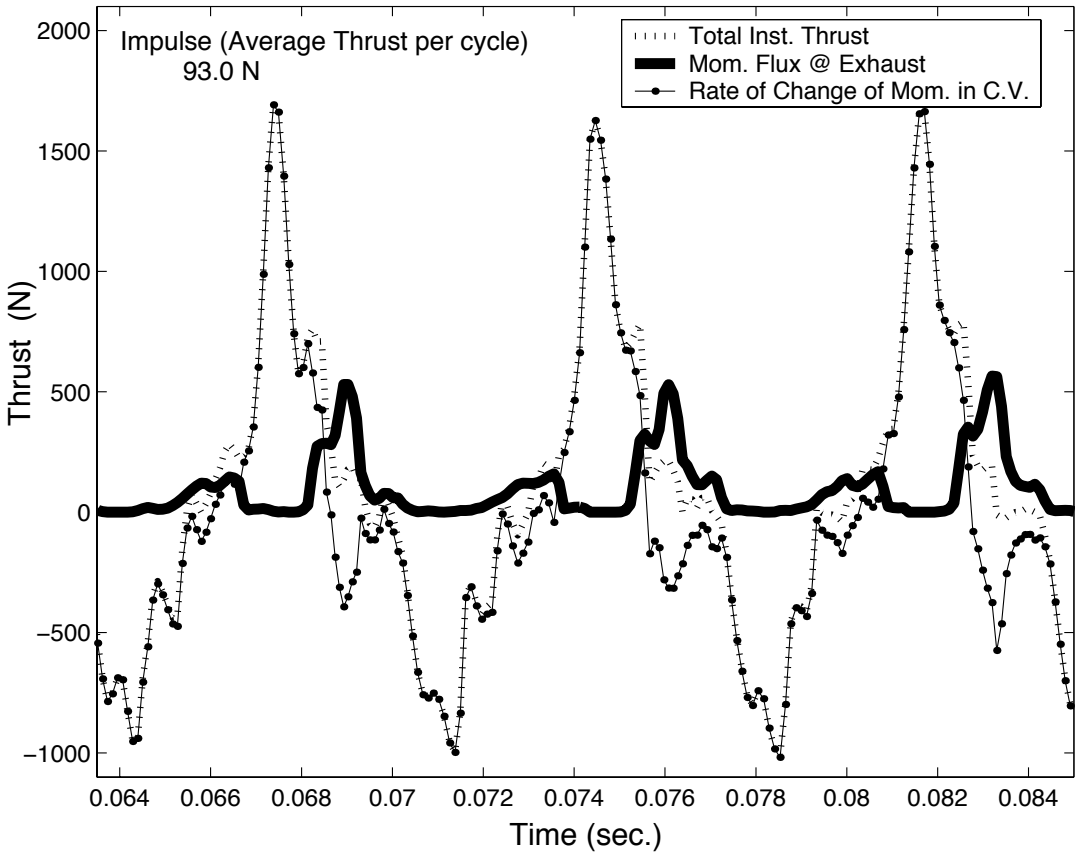

Figure 42: Time dependence of the terms in the instantaneous thrust equation.

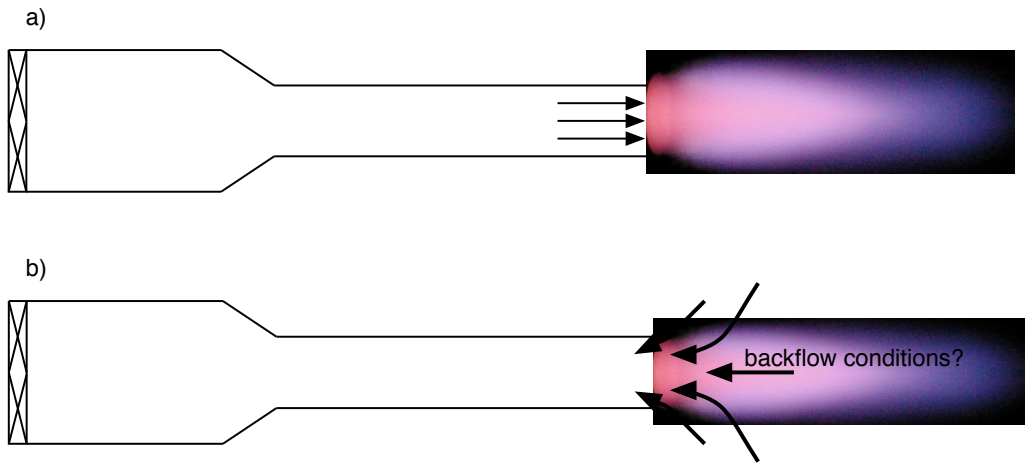

Figure 43: Illustration of a) ejected combustion products mixing with ambient air and b) backflow of resultant mixture back into wave engine.

a more detailed model of the mixing of the combustion products ejected during blowdown and ambient air. Therefore, the backflow species concentrations and temperature must be assumed a priori. Furthermore, the temperature and composition of the backflow influence the acoustic properties by changing γ and the temperature of gases within the tailpipe of the wave engine. In addition, since the backflow gases are subsequently blown down during the thrust producing portion of the cycle, the density, and thus the mass of the backflow gases also influence overall wave engine performance as evident by the terms in the previously discussed thrust equations.

To investigate the effect of backflow temperature and composition on wave engine performance, backflow gas properties were varied from a mixture of combustion products and air at 550K to backflow of all combustion products at the exhaust temperature. These conditions represent two extremes from thorough mixing of the combustion products with the atmosphere to absolutely no mixing where the exhaust gases merely flow back into the engine when backflow begins. Figure 44 presents the wave engine modeled in this investigation, which was assumed to be stationary, and whose inlet valves controlled the inflow of a stoichiometric mixture of methane and air and were characterized by inflow resistance parameter of $\xi = 550.0$.

Figure 45 describes the time dependence of exhaust conditions for a typical wave engine

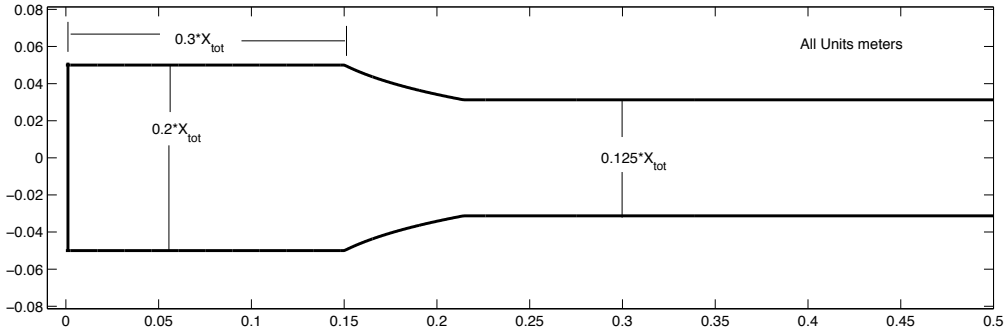

Figure 44: Schematic of engine geometry used in backflow temperature study.

simulation. For this case, the backflow temperature was set to 550K, and as the temporal variation of exhaust density shows, a significant portion of the cycle involves backflow either entering or leaving the engine. Furthermore, the vertical lines in the figure represent the start of mixing (red) and the end of mixing (black). Although it cannot be deduced from Fig. 45, the backflow for this simulation penetrated approximately 60% of the total engine length, but it should be noted that this value depends on the operating conditions and geometry of the tailpipe.

A parametric study of the start of large scale mixing with respect to the opening of the inlet valves was completed for all backflow temperatures. The purpose of this study is to determine if backflow temperature influences the dependence of wave engine performance on the timing between the start of large and small mixing and the start of injection. Optimal timing for the wave engine is defined as the timing that generates the largest average thrust, and these results are presented in Fig. 46. The timing sweeps in Fig. 46 show that the optimal timing does change slightly for different backflow temperatures, and the lowest backflow temperature has the smallest optimal time lag. Figure 46 also shows that the average thrust for backflow temperatures of 550K and 2000K drop off significantly at a time lag of approximately 0.375-0.38. While these two cases do not follow the trend of a monotonic increase in thrust before the optimal lag, both cases did reach limit cycle behavior. The exact cause for this behavior is not clear, but it is hypothesized that this predicted performance drop off may be related to the specification of initial conditions.

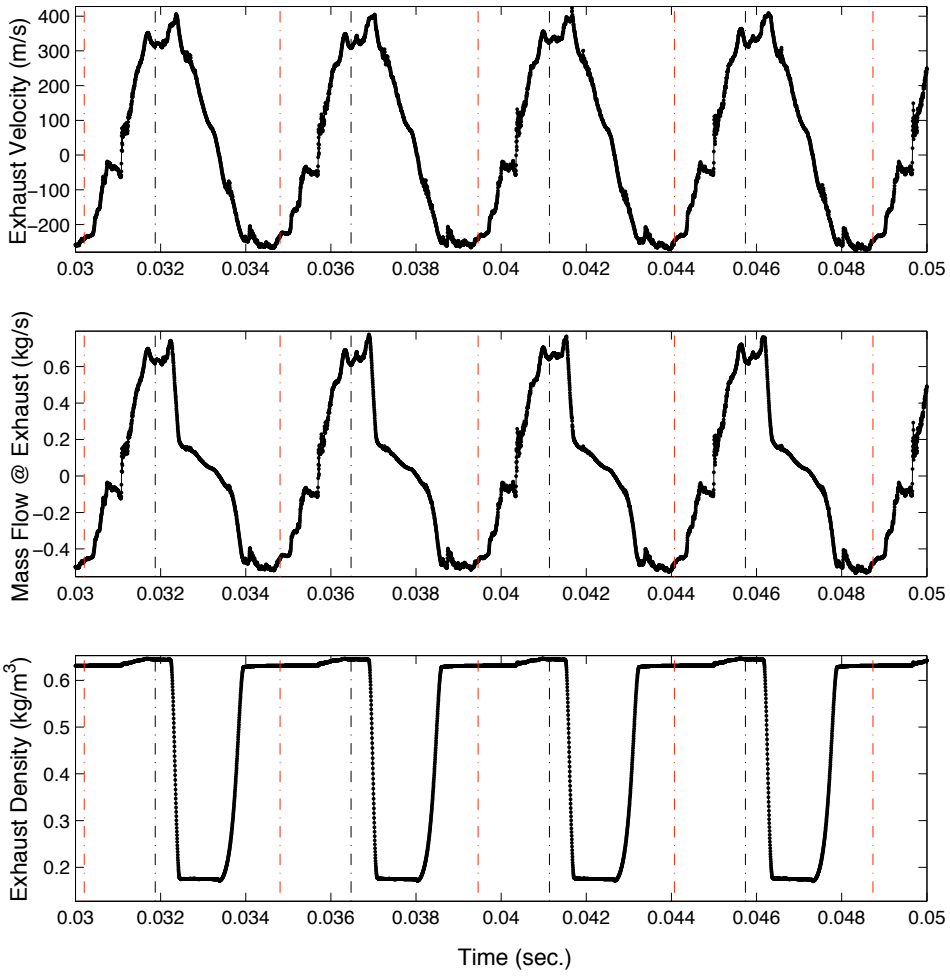

Figure 45: Typical exhaust conditions in terms of velocity, mass flow, and density. Backflow temperature for this case was 550K.

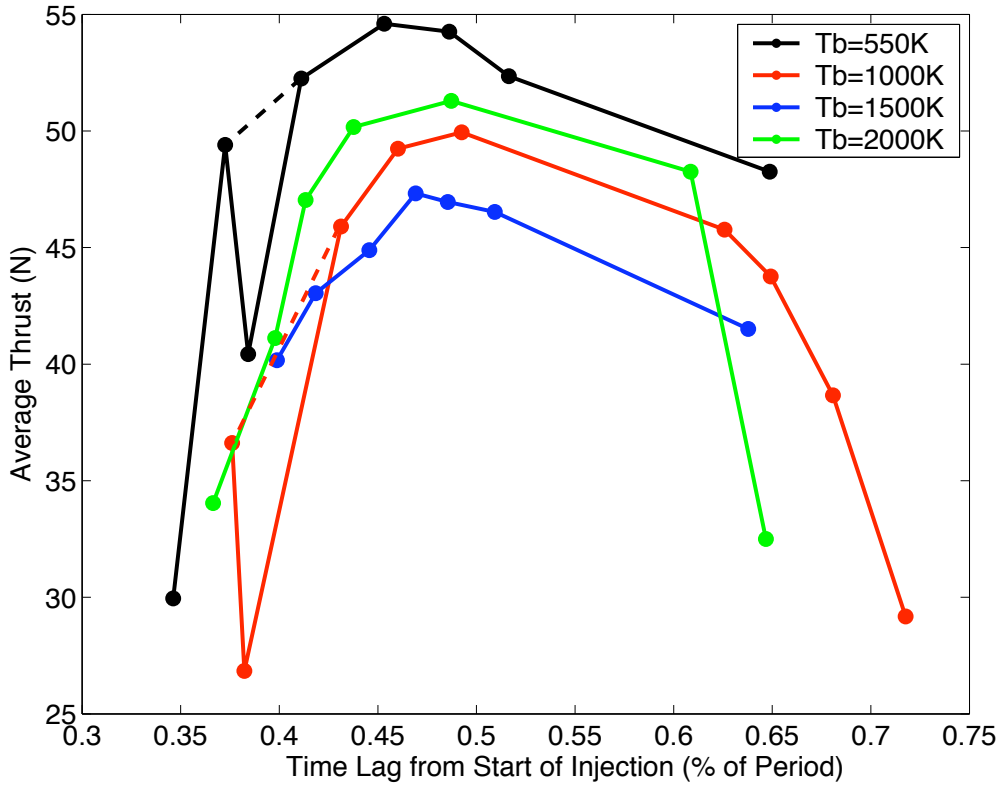

Figure 46: Timing sweeps for different backflow temperatures.

The initial pressure disturbance and flow conditions used to start the engine were the same for all the simulations presented in Fig. 46, and multiple stable limit cycle solutions may exist for certain time lags in this range for these engine conditions. Although not presented in this thesis, a sensitivity study of the amplitude of the initial pressure disturbance and initial temperature was performed for a backflow temperature of 650K, and the results of this study concluded limit cycle performance of the engine to be independent of starting conditions. Nonetheless, the dotted lines represent the more continuous thrust variation with time lag, and these lines are included only for comparison with the other backflow temperature cases. The decrease in thrust output was isolated to these cases and does not occur for the remaining results presented in this thesis. Therefore, while the root cause for this apparent bifurcation may be of interest for future studies, it is not a major concern in this investigation.

Considering only the wave engine performance at the optimal timing, Fig. 47 presents

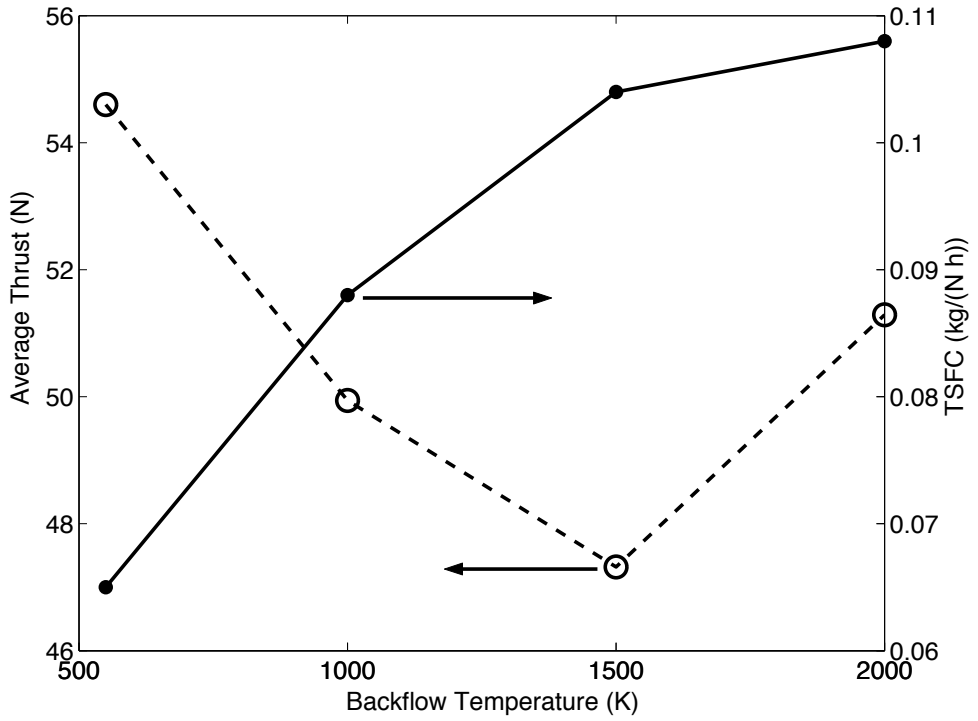

Figure 47: Maximum thrust and corresponding specific fuel consumption for different bacflow temperatures.

the maximum average thrust and specific fuel consumption as a function of backflow temperature. The backflow temperature of 550K generates the largest amount of thrust of 54.6N while a backflow temperature of 1500K generates 47.3N. This is approximately a 15% difference in thrust, thus suggesting that although small errors in the estimation of backflow temperature may not affect thrust levels sugnificantly, it would be useful to study exhaust plume dynamics when optimizing wave engine performance. Furthermore, it is interesting to note that although the thrust appears to have a minimum somewhere between a backflow temperature of 1000K and 2000K, the specific fuel consumption increases steadily with backflow temperature, and the difference between the specific fuel consumption at a backflow temperature of 550K and 2000K is approximately 60%.

Exhaust flow control techniques can be used to tailor the backflow temperature while minimizing any effects these design changes may have on other aspects of performance. For

example, as Fig. 47 suggests, decreasing the backflow temperature can significantly lower the specific fuel consumption, thus requiring less fuel to generate a given amount of thrust. If a primary design constraint of a certain application of wave engine is the minimization of SFC, such as a loitering UAV that can stay airborne for extended periods of time, then techniques for reducing backflow temperature should be explored in the design process. In order to reduce the backflow temperature, it is necessary to re-ingest as little of the hot combustion products as possible. With minimal design alterations, this can be achieved in at least two ways. First, as the mixing between exhaust products and ambient air increases, the overall temperature of the gas mixture decreases. Hence, one way to decrease the backflow temperature is to increase mixing, possibly through the use of chevron nozzles, tabs, or micro-actuators at the exhaust. Second, instead of concentrating on mixing, which may be difficult to control, the other option is to eliminate combustion products from the backflow as much as possible by ingesting air from ports around the circumference of the engine near the exhaust, so that any backflow coming in from these ports will be pure ambient air.

CHAPTER V

WAVE ENGINE PERFORMANCE AS A FUNCTION OF INLET VALVE RESISTANCE AND MIXING CHARACTERISTICS

The previous chapters and sections of this thesis provide an explanation of the motivation behind the development of a quasi one-dimensional unsteady modeling tool capable of simulating the important physical processes in the operation of the wave engine. In addition to the ability to model effects of gas dynamic nonlinearities on driven longitudinal oscillations within ducts, this modeling tool also includes a mixing model capable of qualitatively describing the multiple length scale mixing processes encountered in many pulse combustion systems and wave engines. In addition, this investigation has presented heat release rate and pressure waveform predictions that compare favorably to the unsteady heat release rates and combustion chamber pressures measured in a laboratory pulse combustor. The remaining portion of this investigation uses this modeling tool in parametric investigations of the interdependencies between several important physical processes that strongly influence wave engine performance.

To obtain meaningful results from this portion of the investigation, this tool must be used within the applicable limits based on the assumptions of the individual sub-models. For example, a detailed investigation into the ideal inlet valve design is clearly not feasible with a reduced order quasi one-dimensional model, but an investigation into how the resistance of the valves to mass flow into the engine influences performance is within the capability of this tool. The simulation of large scale coherent fluid structures provides another illustrative example. While this model is incapable of capturing details on the geometry or formation of large coherent structures and their realistic breakdown and dissipation, the influence of the size of large coherent structures on overall performance can be examined with this reduced

order model. Finally, since the dynamics of wave engine performance are dominated by low frequency longitudinal oscillations, the influence of engine shape on wave engine performance can be examined as long as the engine shape is not altered dramatically from one case to the next, so as to change the overall mixing characteristics or create regions where multi-dimensional flow fields influence performance (i.e. recirculation zones at dump planes, etc.). With the previous limitations under consideration, the following parametric investigation described in the remainder of this section concentrate on two main physical aspects of wave engine operation; first, bulk mixing properties and thus, unsteady heat release rates, and second, variations in wave engine shape.

5.1 Inlet Valve Resistance

In the wave engine model development, the mechanical flapper valves on the inlet are modeled by two separate boundary conditions corresponding to when the valves are closed and open. When the valves are closed, a zero velocity boundary condition is assumed, and when the valves are open, the reactant inflow velocity is determined by the pressure difference across the valves. The velocity is then calculated by treating the flow through the valves as flow through an orifice, where the valves are assumed to create a resistance to the flow that is nominally related to the ratio of open valve area to total cross-sectional area at the inlet. The purpose of this portion of the investigation is to examine the influence of this inlet valve resistance on overall wave engine performance. This resistance to inflow is characterized by the parameter ξ, see Eq. 40, and smaller values of ξ lead to larger inflow velocities for a given pressure difference across the valves. For this study, three values of ξ were investigated; namely, 300, 550, and 1000. The numerical values of ξ are not physically correlated with any specific engine parameter or operating regime. These inlet valve resistance values all lead to stable operating conditions at static, sea-level conditions yet still provide a nearly 200% difference in total mass flow rate through the wave engine. Furthermore, the simulated engine for this portion of the investigation is a 0.5m long straight duct, the large scale mixing event size is held constant throughout all simulations, and the small scale rms velocity is assumed to be thirty percent of the maximum inlet velocity.

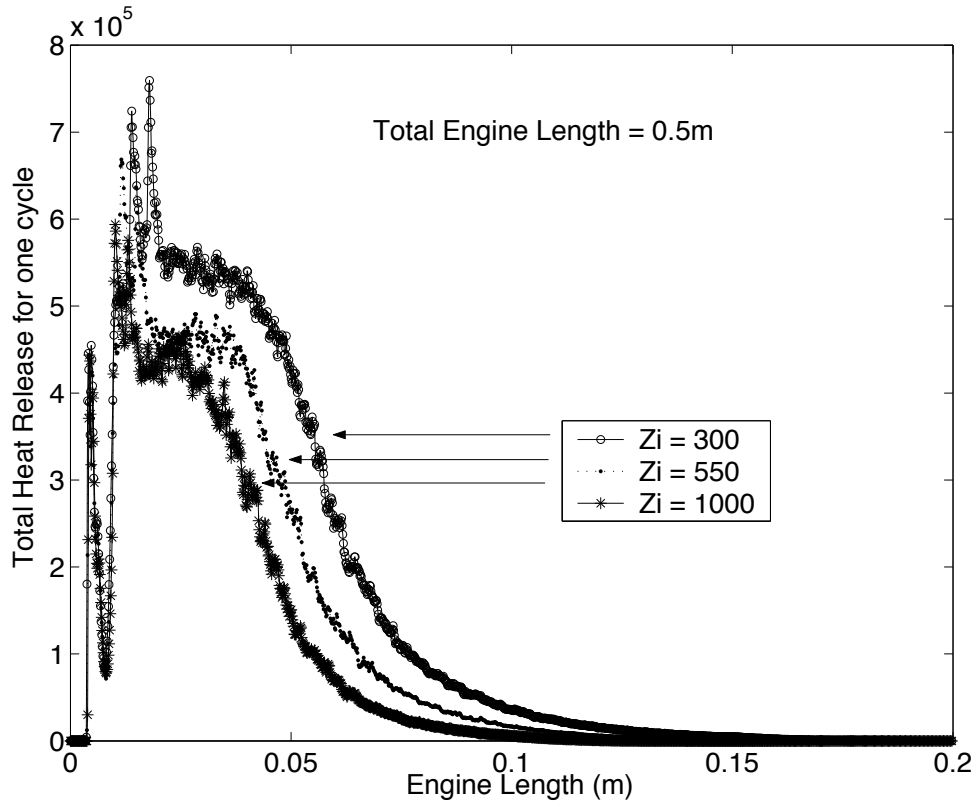

Figure 48: Spatial distribution of heat release for three inflow resistance parameters.

The primary and most obvious effect that increased inflow resistance has on the wave engine is a decrease in the total mass flow through the engine, as shown in Table 2. As reactant mass flow rate increases, the total heat release, shown in Fig 48, also increases. In addition to the total increase in heat release, the spatial distribution of heat release shifts further downstream as the inflow resistance decreases, and this occurs because the increased time needed to burn a larger mass of reactants allows for more extensive turbulent convection of reactants downstream.

Figures 49 and 50 describe the predicted dependence of average thrust and SFC on time lag from the start of injection to the tart of mixing for three inflow resistance values. As the results presented in Table 2 and Figs. 49 and 50 show, the time lag for maximum average thrust is not dependent on the inflow resistance. Second, as expected, there is an increase

Table 2: Summary of engine performance as a function of inflow resistance in terms of maximum average thrust. The time lag refers to the start of mixing in terms of the fraction of a period after the start of injection of reactants (i.e. the opening of the inlet valves).

ξ	300	550	1000
flow rate (g/s)	28.3	20.27	15.03
max Thrust (N)	117.5	111.9	104.1
time lag	0.5073	0.5091	0.5058

in thrust as inflow resistance decreases, yet not nearly as obvious, these simulations predict that this increase in thrust is largest near the optimal time lag. For example, there is an approximately 13% increase in thrust at the optimal time lag between the smallest and largest inflow resistance, but this increase drops to only 5.7% as the time lag decreases from the optimal of around 0.50 to 0.44.

Figure 50 describes the dependence of average SFC on time lag for different inflow resistance values, and much like the backflow temperature study results, the dependence of the SFC on time lag is stronger than that of the average thrust. These results show that the SFC improves (decreases) as the inflow resistance is increased. At the optimal timing, there is a 65% decrease in SFC as the inflow resistance parameter increases. Hence, there is a tradeoff between the maximum attainable average thrust and the lowest possible SFC. For wave engine applications where maximum thrust generation is most important, the inflow resistance should be decreased to maximize thrust output. On the other hand, for long range flight applications where large thrust generation is not of primary importance, and total weight is more of a design constraint, the SFC is more important in terms of overall performance. For this application, Fig. 50 suggests that inflow resistance should be increased to improve performance. In closing, since the large scale mixing event size and small scale rms velocity were held constant, these simulations inherently assume that variations in the inflow resistance do not influence the characteristics of mixing between injected reactants and combustion products from the previous cycle. It is definitely possible to for two flapper valve configurations to produce similar mixing characteristics for different inlet mass flow rates. Nonetheless, it is also probable that inlet valves designed primarily to attain a specific

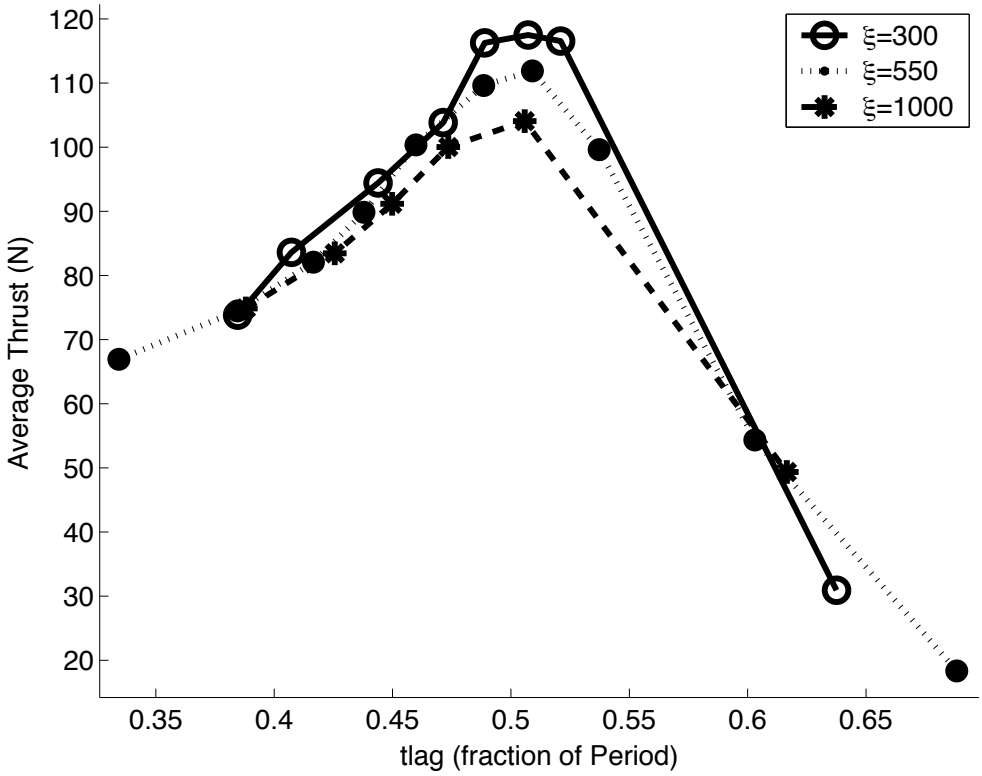

Figure 49: Dependence of average thrust on time lag for three inflow resistance values.

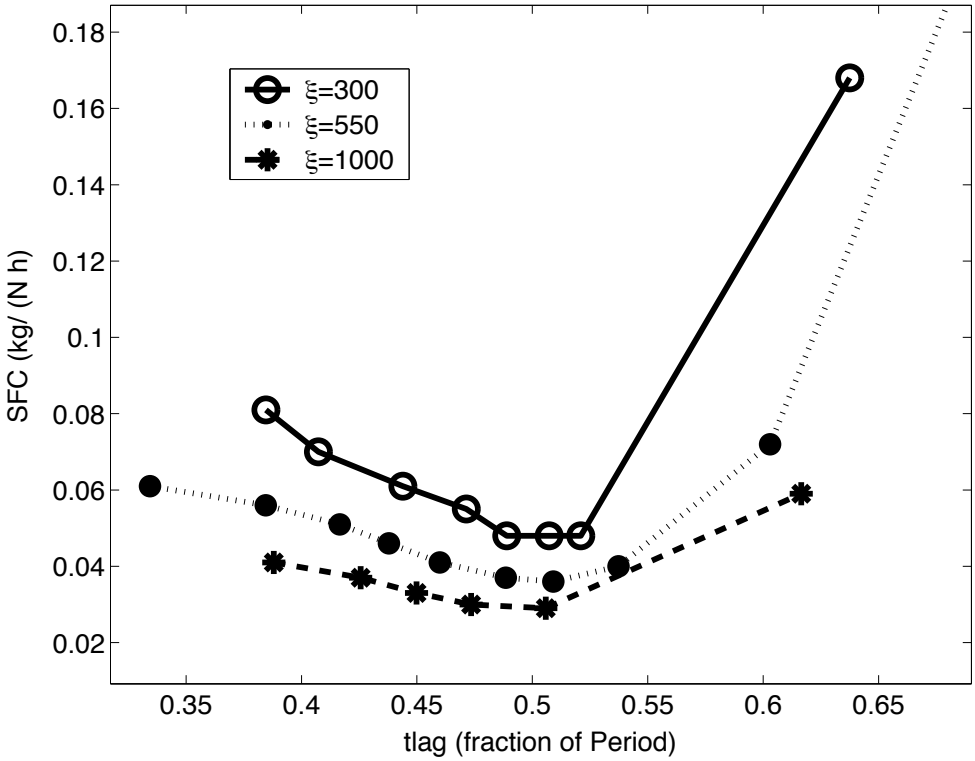

Figure 50: Dependence of average SFC on time lag for three inflow resistance values.

inlet resistance may indeed produce significantly different mixing characteristics.

5.2 Mixing and Unsteady Heat Release Rates

As discussed earlier, the unsteady heat release rates in the wave engine depend primarily on the mixing processes between the impulsively injected reactants and the combustion products leftover from previous cycles. The current mixing model, based on the separation of coherent vortices and turbulence, was motivated by qualitative experimental observations from previous pulse combustor investigations. To date, no detailed mixing studies have been performed to provide additional support for this model. Therefore, due to the lack of experimental data on the characteristics of mixing in wave engines, the present investigation is not based on a specific engine design. Consequently, the mixing model parameters used in this study are based on characteristics of the wave engine such as combustion chamber diameter, flapper valve geometry and inflow velocities. Without detailed measurements of the characteristics of mixing in wave engines, the mixing sub-model used in this study inherently introduces uncertainty in the predicted performance. To address this uncertainty, a parametric investigation of the mixing characteristics was performed to determine the sensitivity of this modeling technique to mixing model parameters. This investigation also provides a first order analysis of the influence of mixing characteristics on overall wave engine performance, thus providing a starting point for the design of injections systems (flapper valves or valveless inlets) and combustion chambers.

Excluding the timing of the large scale mixing event and subsequent small scale mixing, the developed LEM model contains three parameters that dictate the characteristics of mixing. The first parameter is the size of the large scale mixing event. This size corresponds to the size of the vortical structure formed from the impulsive injection of reactants at the inlet. More specifically, this vortex structure and size is determined largely by the injection area, such as opening valve area of the flapper valve arrangement, the combustion chamber area, and the momentum of the injected reactants. For example, reactant injection through the open flapper valves in a wave engine can be reasonably idealized as the impulsive injection of fluid through a number of orifices. This injection can create flow structures

Figure 51: Experimental visualization of a vortex ring created by the impulsive injection of water from a tube. Taken from [16].

such as vortex rings [See Fig. 51]. Vortex rings have been the focus of a variety of studies examining such topics as the disposal of chimney waste and the propulsive methods of certain aquatic creatures [36, 17, 16], and the size of these vortex rings would determine the size of the large scale event in the LEM model.

The second LEM model parameter is the root mean squared (rms) velocity of the small scaling mixing processes. The rms velocity is related to the intensity of the small scale mixing. In the LEM model, the rms velocity partially determines the number of small scale mixing events that take place per unit time. For example, given one size of small eddy in the LEM model, increasing the rms velocity increases the number of events per unit time, so overall mixing increases. The final LEM model parameter is the size of the small scale mixing events, which corresponds to the average size of small scale eddies. For a given rms velocity, this parameter influences both the modeled eddy size as well as the number of events per unit time. Since the rms velocity corresponds to the total amount of energy available for mixing, then an increase in the size of a small eddy is accompanied by a decrease in the total number of small scale mixing events. As discussed previously, a single small scale eddy size has been shown to reasonably model mixing processes for wave engine like conditions and engineering applications, but the size of this small scale eddy is not yet known.

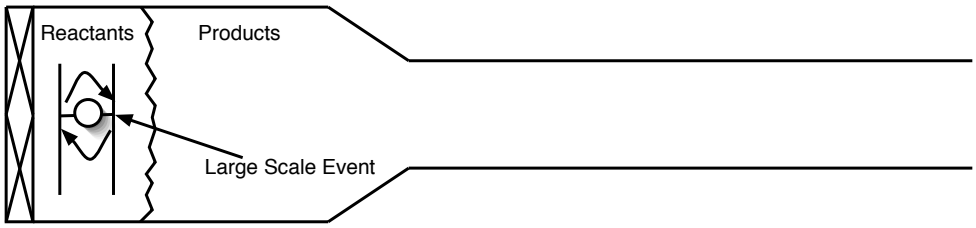

Figure 52: Wave engine schematic with ineffective large scale mixing event location.

5.2.1 Large Scale Mixing Event Size

The primary purpose of the large scale coherent structures is to provide bulk mixing of reactants and products on a length scale much larger than the turbulent length scales. Since small scale mixing occurs randomly in space and time and transports mass over small distances, large scale mixing is the most important factor in determining the overall distribution of heat release in the combustion chamber. As Fig. 23 shows, effective large scale mixing in a one dimensional formulation requires that the axial location of the large scale event contain significant amounts of both reactants and products. The location of the center of the large mixing event in previous wave engine simulations was determined by tracking the interface between the injected reactants and the combustion products. Interface tracking was necessary to position the large scale mixing event at the interface between freshly injected reactants and combustion products from the previous cycle. For example, given the location of reactants at the start of mixing depicted in Fig. 52, the size and location of the illustrated large scale event produces no mixing of reactants and products. On the other hand, for this study, the total penetration of reactants into the engine is not greater than half of the large scale mixing event size, so the upstream side of the large scale event is held constant while maintaining adequate mixing of reactants and products.

For the following simulations, three large scale events of different sizes are assumed for a 0.5m long wave engine with a straight combustion chamber comprising 30% of the total

length. The cross sectional area of the tailpipe is 20% smaller than the combustion chamber area. Additionally, the small scale event size is 10% of the large scale event size and the rms velocity of the small scale turbulence is 10% of the maximum injected velocity at the inlet. The large scale event sizes are expressed as a percentage of the combustion chamber diameter and range from approximately 34% to 118%. Figure 53 displays the engine geometry and the spatial distribution of heat release for the three different large scale events. As the large scale event size increases, the spatial distribution of heat release moves downstream because the larger mixing event transports reactants further away from the inlet. The spatial distribution of heat release in the wave engine is an important physical characteristic of the engine since the driving of oscillations in the engine is nominally related to the local energy addition as well as the local oscillation amplitude. Also, Fig. 53 qualitatively shows that the overall heat release for these cases does not change appreciably, showing that the total amount of injected reactants each cycle is nearly the same for the three cases.

One would expect however, that for a wave engine operating at the quarter wave mode, acoustic energy addition is controlled by Rayleigh's criterion; therefore, a shift of the unsteady heat release further from the pressure antinode (i.e. the inlet) should decrease the total acoustic driving, thus decreasing the thrust output of the engine. Contrary to this hypothesis, Fig. 54 predicts a ten percent increase in average thrust between the largest large scale event and the smallest, with a similar relative decrease in SFC between the two cases. From the perspective of determining the sensitivity of the model predictions to large scale event size, the results in Fig. 54 suggest that a factor of three difference in the large scale event size amounts to only a ten percent difference in maximum predicted thrust. This suggests that the calculated thrust does not depend strongly on the large scale mixing characteristics, therefore exact knowledge of large scale mixing event properties is not necessary to reasonably predict wave engine performance. The results in Fig. 54 also reveal a shift in the optimal timing as a function of the large scale event size. Both average thrust and SFC calculations show that the optimal timing as a fraction of the oscillation period increases as the large scale event size increases.

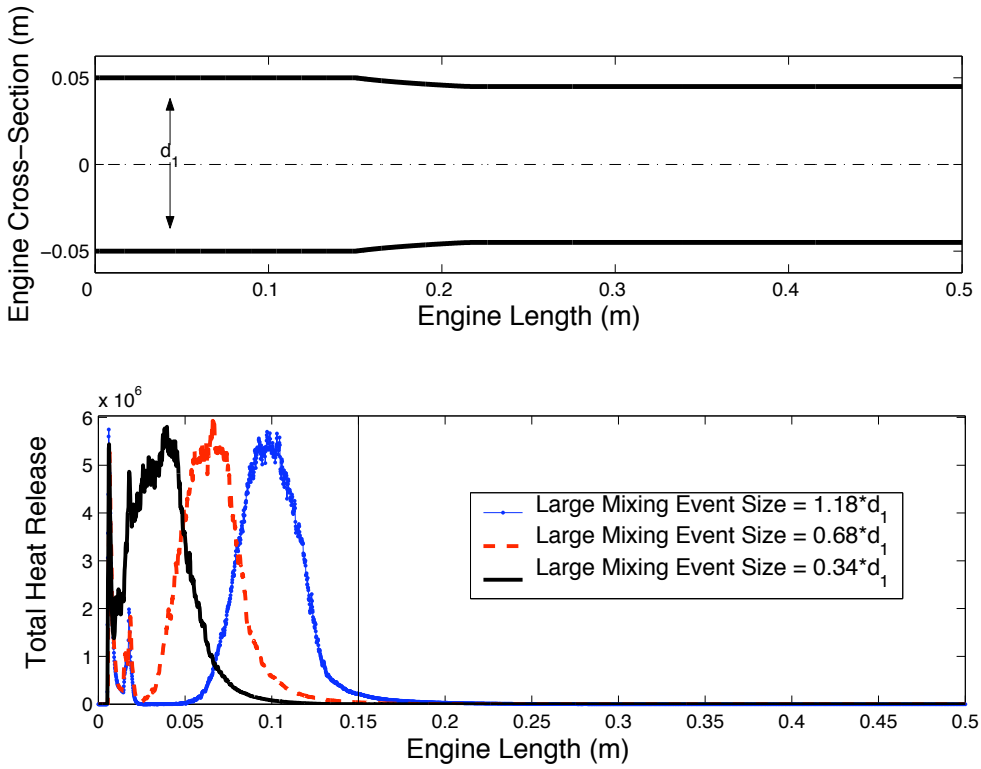

Figure 53: Engine geometry and spatial distribution of heat release for different large scale event sizes.

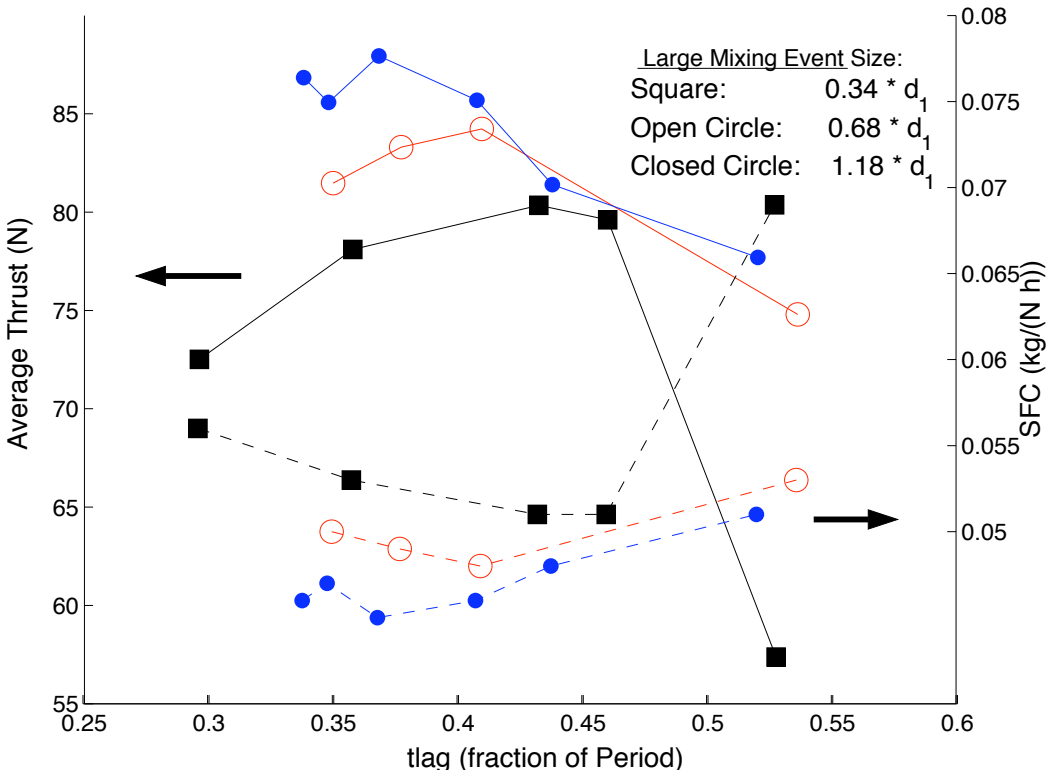

Figure 54: Average thrust and SFC vs. time lag from start of injection to start of mixing for three large scale mixing event sizes. Solid lines represent thrust calculations, with scale on the left axis and dashed lines represent SFC, with scale on the right axis.

5.2.2 Small Scale Mixing RMS velocity

The rms velocity of the small scale turbulent mixing is the parameter that determines the mixing intensity, which plays an important role in determining the time dependence of the unsteady heat release rate each cycle. Consequently, the small scale mixing intensity influences the overall performance of the wave engine by controlling the relationship of the phase difference between pressure oscillations and the unsteady heat release rate. Physically, the small scale mixing intensity is determined by a combination of factors including the breakdown of large coherent structures into small scale turbulence as well as small scale turbulence introduced directly by the inlet valve system. Furthermore, the characteristics of the turbulent mixing field could be controlled with additional hardware such as flow field obstruction devices or acoustic forcing. The use of additional hardware could, however, adversely affect the engine's thrust/weight ratio and/or engine complexity. Hence, possible ancillary performance losses must be considered along with the additional benefit of increased control over mixing processes.

For this investigation, the rms velocity has been assumed to be directly related to the maximum inlet velocity, allowing the parametric variation of rms velocity to be expressed in terms of the fraction of the maximum inlet velocity. In this study, the large scale event size is 35% of the combustion chamber diameter and the small scale event size is 10% of the large scale event size. The total engine length is 0.5m and the combustion chamber occupies 30% of the total engine length. Furthermore, the ratio of the combustion chamber diameter to tailpipe diameter is 1.1 and the valve parameter ξ is 550.0.

The three rms velocities chosen for this investigation were 10, 20, and 30 percent of the maximum inlet velocity. Figure 55 displays the engine geometry chosen for this study and the spatial distribution of heat release within the combustion chamber for the three rms velocities. The heat release profiles show that an increase in small scale mixing intensity shifts the heat release slightly downstream due to an increase in turbulent convection. More importantly, variation of the rms velocity of the small scale mixing does not affect the spatial distribution of heat release nearly as much as variations in the size of the large scale mixing events. Table 3 presents a summary of engine performance as a function of the rms velocity

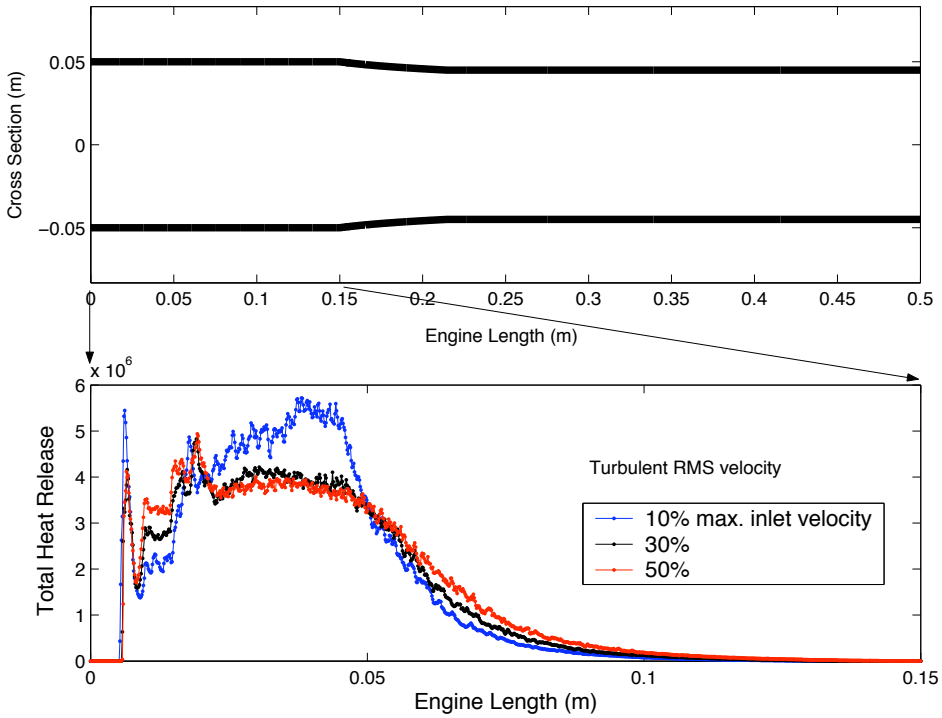

Figure 55: Engine geometry and spatial distribution of heat release within the combustion chamber for three small scale turbulent mixing intensities.

of the turbulent mixing, and these tabulated results show that the increase in rms velocity from 10% to 50% has very little influence on the average mass flow rate or the operating frequency.

The time dependence (normalized by the oscillation period) of the total heat release within the combustion chamber is displayed in Figure 56 for the maximum average thrust cases of each turbulent rms velocity. The results in Fig. 56 show that the largest turbulent rms velocity case has the largest peak and shortest duration of heat release, confirming that larger turbulent rms velocities (i.e. higher intensity mixing) cause more rapid burning of reactants. Figure 56 also shows that the qualitative difference in the temporal profiles of heat release is greater between the 10% and 30% cases than the 30% and 50% cases even though the change in mixing intensity is almost the same between the three cases. As the turbulent rms velocity increases, the turbulent time scale decreases and eventually approaches the chemical kinetic and/or ignition/pre-heating time scales for the reactants in

Table 3: Summary of engine performance as a function of rms velocity of small scale mixing in terms of maximum average thrust. The time lag refers to the start of mixing in terms of the fraction of a period after the start of injection of reactants (i.e. the opening of the inlet valves).

rms Velocity frac. of $max(u_{inl})$	Ave Mass Flow Rate (g/s)	Time Lag	Operating Freq. (Hz)	# of events per cycle
0.1	20.54	0.4324	315.7	790
0.3	21.2	0.4974	319.7	2385
0.5	21.0	0.4895	316.6	3975

the engine. The previous qualitative observation shows that as mixing intensity increases, and the turbulent time scale decreases, the maximum rate of heat release for this wave engine is no longer mixing rate limited but rather limited by either chemical kinetic or ignition/pre-heating time scales.

Figure 57 shows that the oscillation waveform is similar for the different rms velocities, although the lower small scale mixing intensity leads to lower maximum inlet pressure amplitudes. Additionally, Fig. 57 shows that while the unsteady heat release is governed largely by the mixing processes, and thus, is not sinusoidal, the operating frequency of the engine is very close to the fundamental natural acoustic frequency of the duct, resulting in nearly sinusoidal pressure oscillations.

Figure 58 describes the time dependence of axial velocity in the middle of the combustion chamber (a) along with the corresponding windowed FFT of each trace (b). The FFT of the velocity traces show that while the pressure oscillations are nearly sinusoidal, as shown in Fig. 57, the velocity contains significant harmonic content. Furthermore, the velocity traces in the combustion chamber contain much more noise due to turbulence, and the turbulent fluctuations increase as the rms velocity increases. It is important to note that the predicted velocity characteristics significantly differ from the combustion chamber pressure. One reason for this is the inlet boundary condition. The switching of the inlet boundary condition from a closed wall when the valves are closed to an analogous porous plate as reactants are injected into the engine significantly alters the local velocity field in the combustion chamber but does not impact the pressure field nearly as much.

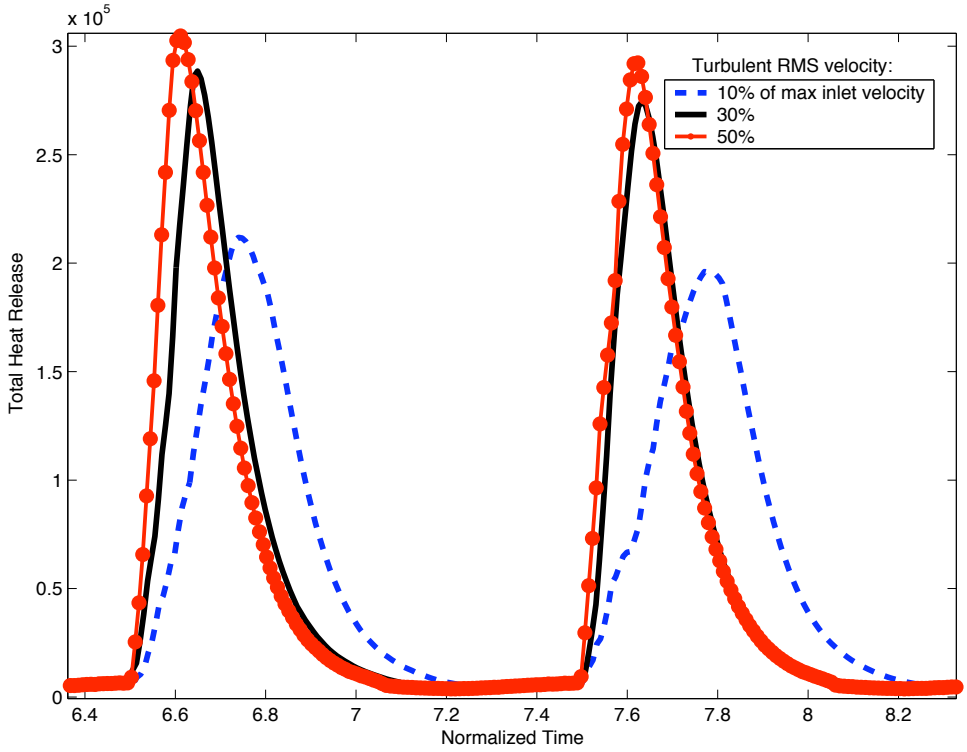

Figure 56: Time dependence of total heat release for turbulent rms velocities of 10, 20, and 30 percent of the maximum inlet velocity.

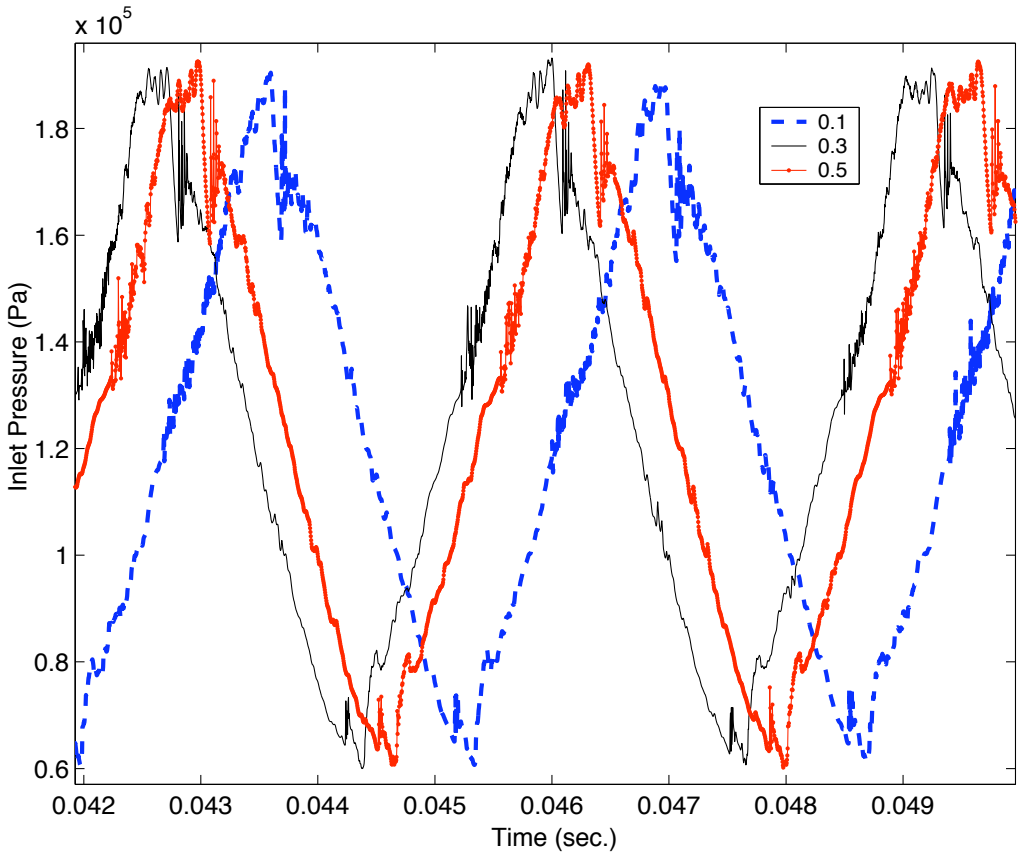

Figure 57: Inlet pressure vs. time for rms velocity of 10, 20, and 30 percent of maximum inlet velocity.

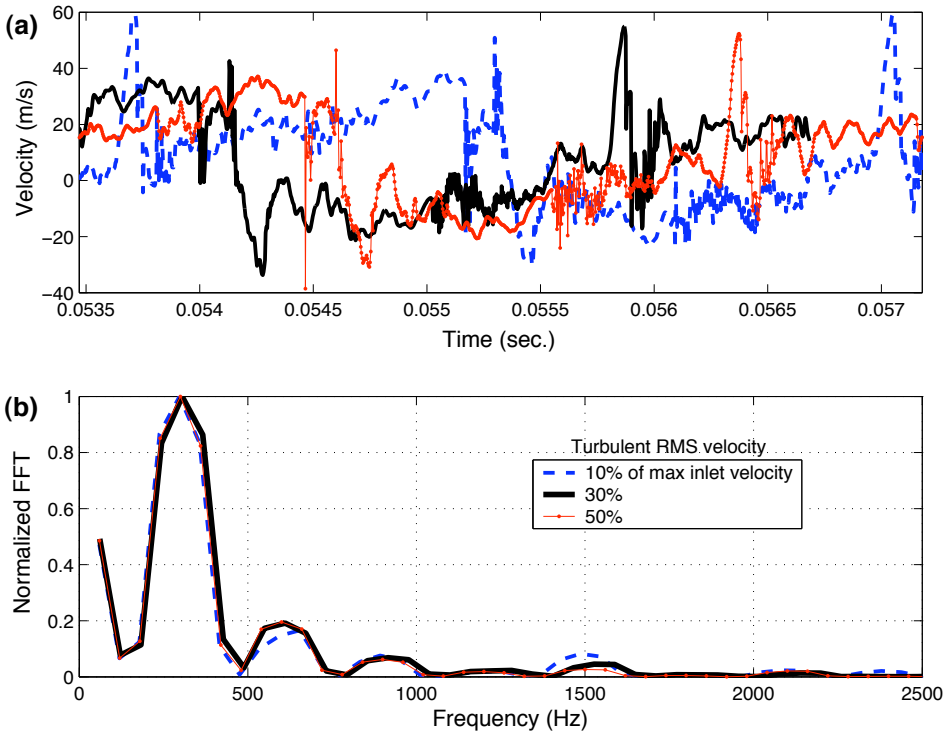

Figure 58: (a) Velocity in middle of the combustion chamber vs. time for rms velocities of 10, 30, and 50 percent of maximum inlet velocity. (b) Windowed FFT of velocity traces in (a)

The dependence of the average thrust and SFC on time lag for the three rms velocities are described in Figs. 59 and 60, respectively. Figure 59 shows the time lag at which the maximum average thrust occurs depends upon the turbulent rms velocity, increasing in magnitude as the rms velocity increases. Figure 59 also shows that the maximum thrust generation is smallest for the lowest rms velocity and that the sensitivity of thrust to time lag decreases as rms velocity decreases. The result of this decreased sensitivity is that the average thrust generated for the least intense mixing actually surpasses those produced by more intense mixing for time lags smaller than the optimal value. This behavior introduces a trade-off where the maximum attainable thrust levels decreases for the case of less intense mixing, but the range of time lags that produce acceptable performance increases. Given that the timing between unsteady heat release and flow field oscillations may be one of the most difficult things to control in the wave engine, it may be desirable for wave engine designs to sacrifice maximum attainable performance for a larger acceptable operating regime.

The previous observations that both the optimal time lag and the sensitivity of average thrust to time lag decrease as the turbulent rms velocity decreases can be explained by considering the driving of the flow field oscillations by unsteady heat release. As an example, consider a spatially homogeneous volume with a temporal flow field oscillation, $s(t)$, where s represents pressure:

$$s(t) = sin(t + \phi). \tag{67}$$

Additionally, assume the presence of a spatially uniform unsteady heat addition in this volume with the following time dependence

$$q(t) = \frac{e^{-(ln(t)^2/(2\sigma^2))}}{t\sigma\sqrt{2\pi}}. \tag{68}$$

This heat addition process is described by a log normal distribution function because of it's resemblance with temporal heat release profiles shown in Fig. 56. The parameter σ is inversely related to the mixing intensity, and the heat addition remains constant for all values of σ since the log normal distribution function always integrates to one. For the purpose of this explanation, the driving of flow field oscillations is quantified by the

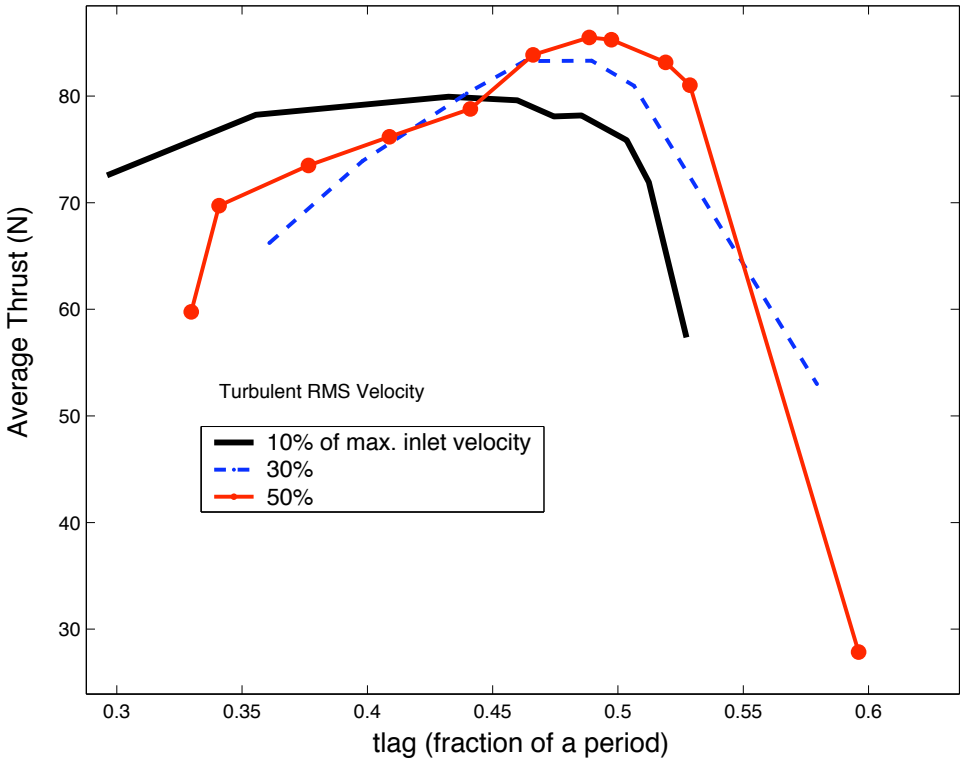

Figure 59: Average thrust vs. time lag from the start of injection to the start of mixing.

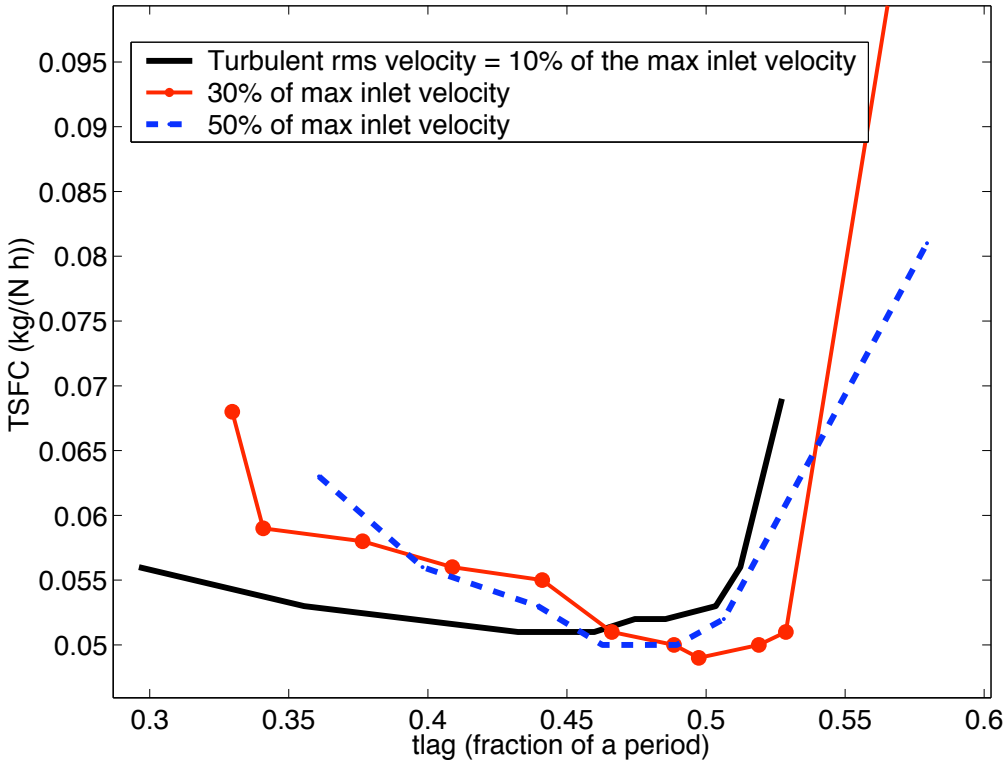

Figure 60: Specific fuel consumption vs. time lag from the start of injection to the start of mixing.

Rayleigh integral, described by

$$R = \int_0^T s'q'dt, \tag{69}$$

where T is the period of the oscillations and a positive or negative R value implies that the heat release process drives or damps flow field oscillations, respectively. In order to relate the computed value of R to the predictions from the wave engine simulations, the time lag is represented as the phase between s and q. Figure 61 illustrates the phase relationship between flow field oscillations and two heat addition functions with σ values of 0.1 and 0.25, corresponding to the cases of more and less. Figure 62 shows the dependence of the Rayleigh integral on the phase between the flow field oscillation and the heat addition for the two heat addition functions shown in Fig. 61. Interestingly, the trends exhibited in Fig. 62 capture several characteristics of the predictions of the wave engine simulations, thus suggesting that the coupling between unsteady heat release and flow field oscillations can be used to explain the dependence of the wave engine performance for different mixing intensities. First, Fig. 62 shows that the maximum Rayleigh integral for $\sigma = 0.1$ is larger than that for $\sigma = 0.25$, just as the 30% rms velocity case predicted larger average thrust generation than the 10% rms velocity case shown in Fig. 59. Second, Fig. 62 predicts that the maximum Rayleigh integral for $\sigma = 0.1$, which qualitatively corresponds to the 30% turbulent rms velocity case, occurs at a longer phase difference than for $\sigma = 0.25$, which is corresponds to the 10% rms velocity. For $\sigma = 0.25$, the majority of the heat release occurs slightly later in cycle, therefore the optimal time lag occurs slightly before the optimal time lag for $\sigma = 0.1$. Finally, Fig. 62 shows that the Rayleigh integral for $\sigma = 0.1$ drops off more significantly away from the maximum than for $\sigma = 0.25$, thus following trends od predicted wave engine performance. Qualitatively, this behavior can be explained by noting that as σ decreases, the heat release occurs over a shorter period of time, and thus, a smaller portion of the flow field oscillation. Therefore, the Rayleigh integral is more sensitive to differences in phase between the flow field oscillation and the heat addition processes.

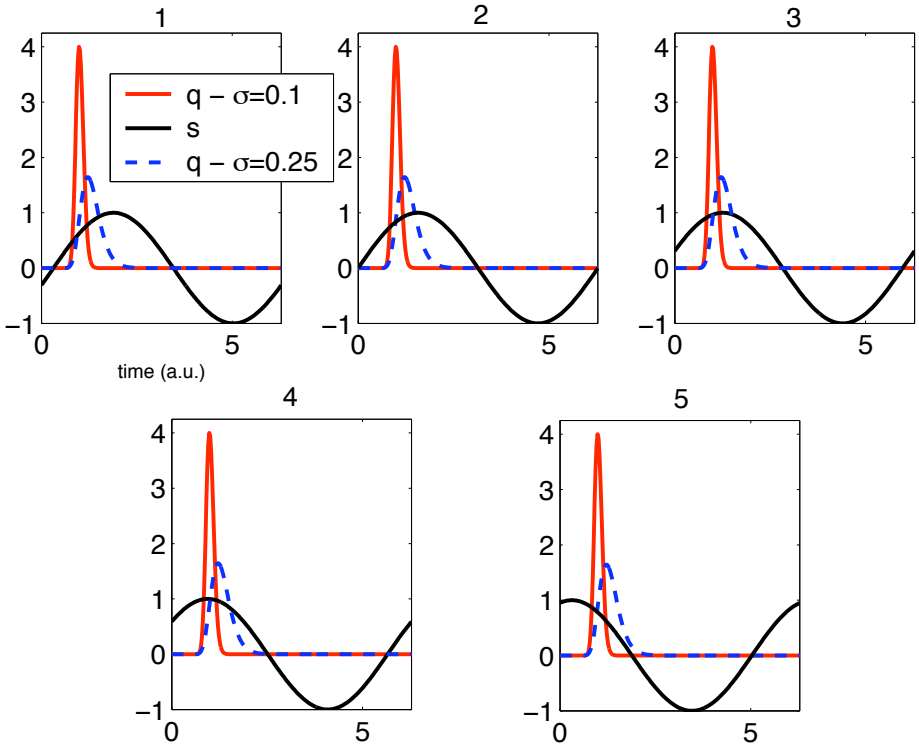

Figure 61: Sinusoidal flow field oscillation and two heat addition functions with $\sigma = 0.1$ and $\sigma = 0.25$ for five phase values.

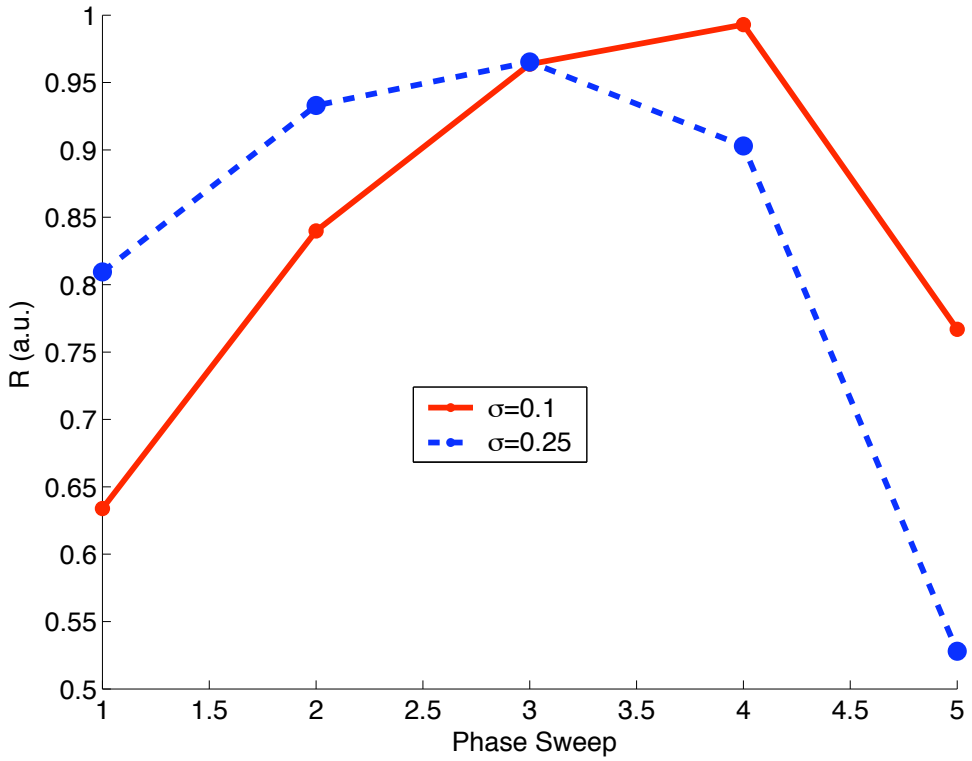

Figure 62: Dependence of Rayleigh integral on phase between heat addition and flow field oscillation for two log normal heat addition functions, $\sigma = 0.1$ and $\sigma = 0.25$.

5.2.3 Turbulent Mixing Event Size

For the investigation of the turbulent eddy size, the rms velocity is 5.0m/s and large scale mixing event size is 35% of the combustion chamber diameter. The total engine length is 0.5m and the combustion chamber occupies thirty percent of the total engine length. Furthermore, the ratio of the combustion chamber diameter to tailpipe diameter is 1.6. Finally, the small scale eddy size is varied from five% to 25% of the size of the large scale mixing event size.

Figure 63 shows the dependence of the average thrust on the time lag and and the small scale eddy size. Figure 63 shows that the predicted average thrust maximum average thrust dependds weakly on time lag, but more importantly, for all but the largest small scale eddy size, the predicted thrust does not change substantially. Furthermore, for a given mixing intensity, an increase in the turbulent eddy size from 15% to 25% leads to substantially lower thrust output. This result is reasonable, since a small scale eddy size of 25% of the largest mixing scale in the engine is unrealistically large. For this unrealistically large small scale eddy size, the reactants were not burned completely during one cycle, resulting in a significant thrust reduction. Figure 63 shows that when the largest small scale eddy size is excluded, small scale eddy size increased in size by a factor of three the remaining data shows that the maximum thrust predicted changes by only 2%. The results in Fig. 63 thus indicate that if the small eddy size is not unrealistically large, small scale eddy size changes do not have a large impact on the predicted overall performance of the engine. Figure 64 shows the corresponding SFC for the cases described in Fig. 63. It shows that the SFC is most favorable at the highest predicted thrust levels, and that the SFC increases dramatically as the large turbulent mixing event size increases unrealistically from 15% to 25%.

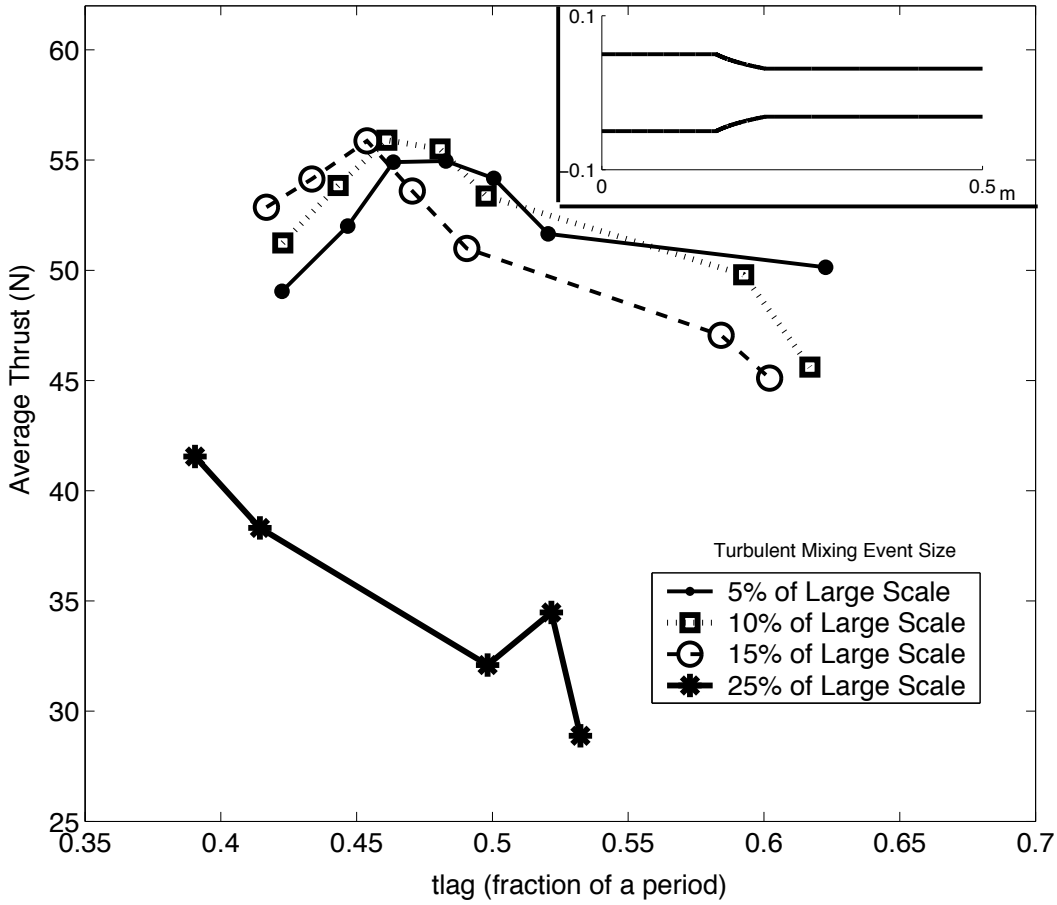

Figure 63: Average thrust as a function of timing for small scale eddy sizes ranging from five to twenty five percent of the large scale event size. Engine geometry shown in upper right corner(all units meters).

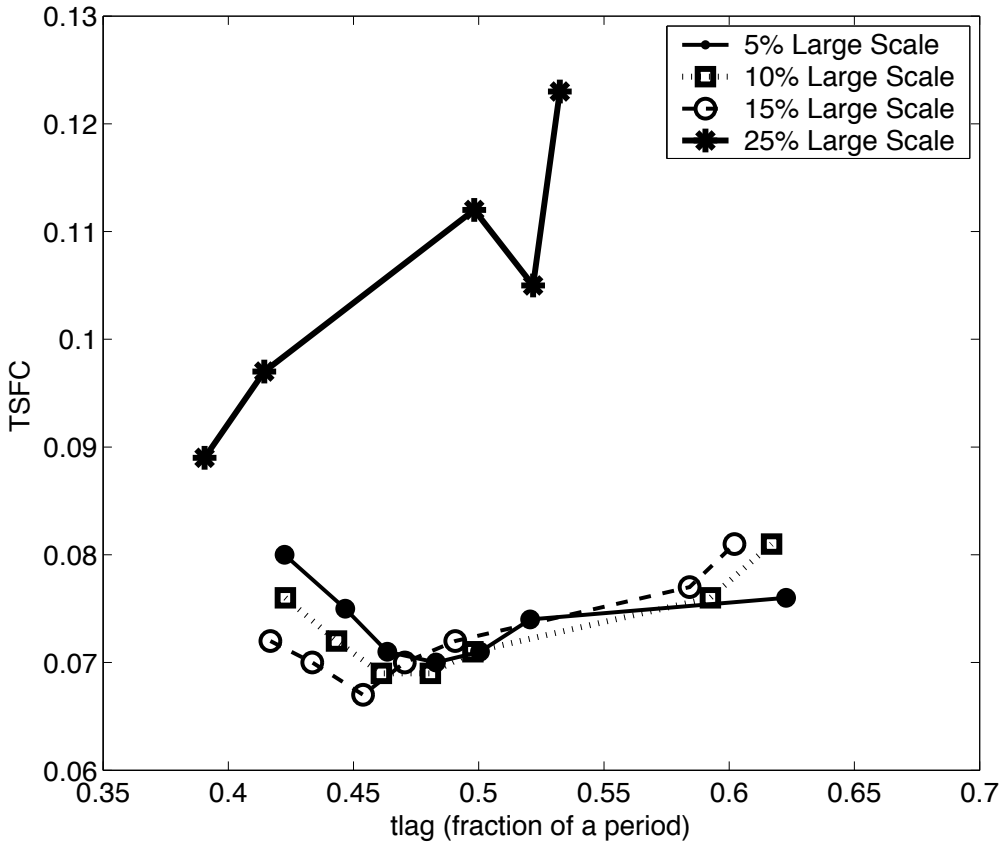

Figure 64: Dependence of SFC on time lag for turbulent mixing event sizes of 5-20% of the large scale mixing event size.

CHAPTER VI

WAVE ENGINE PERFORMANCE AS A FUNCTION OF ENGINE SHAPE

The parametric studies presented in the previous chapter investigated the influence of inlet conditions and mixing characteristics on the overall performance of one wave engine geometry. The previous investigation of the model parameters of the dual length scale mixing model demonstrated that large and small scale mixing characteristics significantly influence wave engine performance through their effect on unsteady heat release rates. From a design perspective, this investigation also established that mixing characteristics and thus, unsteady heat release rates, must be well understood in order to optimize wave engine performance. Furthermore, this investigation of the influence of unsteady heat release rates on performance concentrated on one specific wave engine shape, thus requiring that the acoustic properties of the engine essentially remained constant. As discussed previously, since the wave engine operates as a self-excited acoustic system, the unsteady heat release rate is directly coupled to other characteristics of the wave engine that influence the acoustic properties of the engine, such as engine shape and mean property gradients. The purpose of the following investigation is to examine the influence of the acoustic properties of the engine on overall performance while the mixing characteristics remain constant. The primary acoustic property of interest for this study is the relationship between the natural acoustic mode frequencies of the engine. Just as in the previous investigation of acoustic resonators, the distribution of natural acoustic mode frequencies will be modified by changing the engine shape.

Equation 21, which describes the natural acoustic wave numbers for the exponential horn duct used in the forced acoustic resonator study, showed that relatively small changes in the duct shape (controlled by the flare constant, α) can significantly shift the distribution of natural acoustic mode frequencies. Therefore, to minimize the impact of modifications

of the engine shape on mixing processes in order to isolate the influence of engine shape on the distribution of natural acoustic mode frequencies, this study concentrates on small modifications to engine shape. The first portion of this study varies tailpipe diameter while the combustion chamber dimensions remain constant. The second portion of this study investigated the influence of the addition of exhaust nozzles and flare on the overall performance.

6.1 Tailpipe Diameter

Figure 65 shows the three wave engines studied in this portion of the investigation. These wave engines are all 0.5m long and the combustion chamber occupies 30% of the total engine length. The tailpipe diameters range from slightly smaller than the combustion chamber diameter to a straight engine to slightly larger than the combustion chamber diameter. For the smaller tailpipe diameter described by Fig. 65 a), the tailpipe diameter is 90% of the combustion chamber diameter, hence the cross sectional area of the tailpipe is approximately 20% smaller than the combustion chamber. The larger tailpipe diameter engine, Fig. 65 c), is 10% larger than the combustion chamber diameter, thus the cross sectional area of this tailpipe is approximately 20% larger than the combustion chamber. Static, sea level conditions were assumed for all simulations, the inflow resistance parameter, ξ, is 550, and the assumed backflow temperature was 650K.

Figure 66 describes the average thrust as a function of the time lag from the start of injection to the start of large and small scale mixing. It shows that the straight duct engine produces the largest maximum average thrust of the three engines, and the wave engine with the smaller tailpipe generates the smallest maximum average thrust. Figure 66 also shows that a 20% decrease in tailpipe area reduces the maximum average thrust by approximately 32% and that a 20% increase in tailpipe area reduces the maximum thrust by approximately 7%. Figure 66 also shows that the dependence of average thrust on the time lag between the start of injection and the start of mixing is qualitatively similar for the straight engine and the larger tailpipe diameter engine. On the other hand, the average thrust for the smaller tailpipe wave engine is less dependent upon the time lag than the other two engines. This

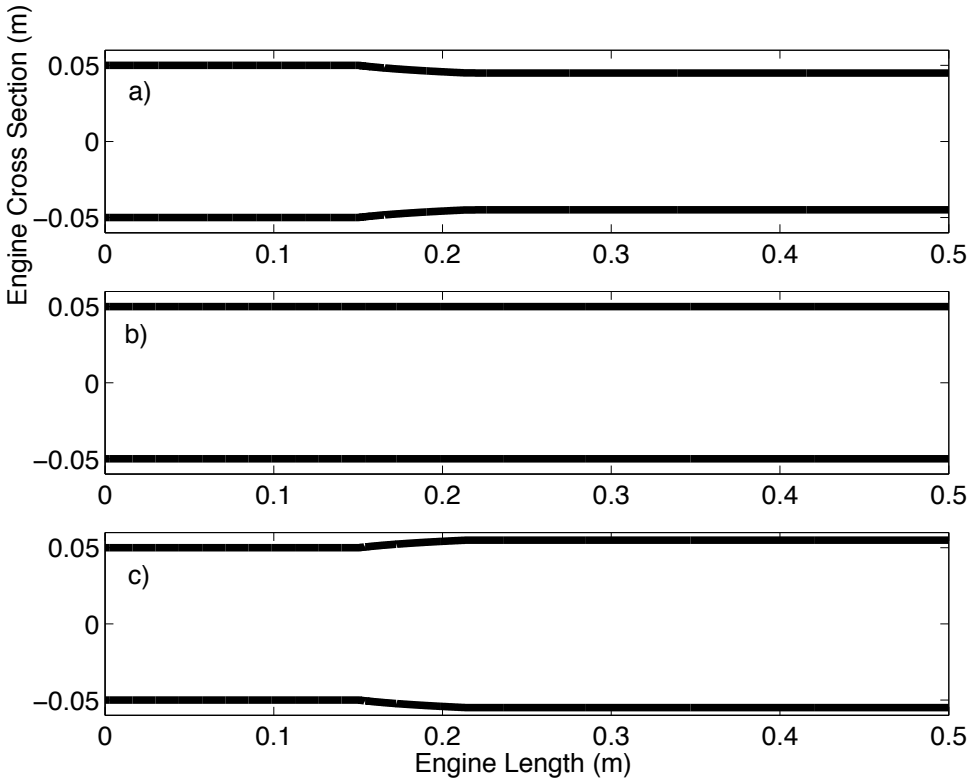

Figure 65: Configurations of the three investigated wave engines having different tailpipe diameters. Tailpipe cross sectional area of a) is approximately 20% less than combustion chamber, b) is a straight duct, and c) is approximately 20% greater than combustion chamber.

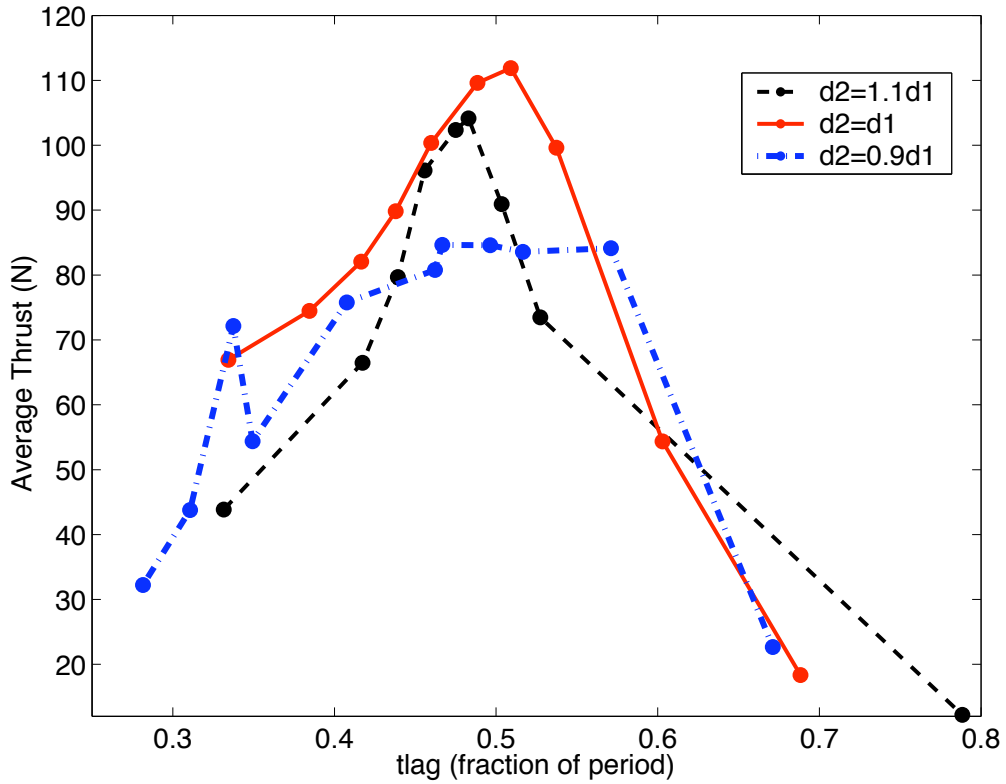

Figure 66: Average thrust vs. time lag for three engine shapes featuring different tailpipe diameters.

qualitative difference in the dependence of average thrust on time lag suggests that different physical processes may control the maximum thrust generation for this wave engine, and a more detailed investigation into the physical processes responsible for these trends is necessary to elucidate these performance differences. Figure 67 describes the dependence of average SFC on time lag for the three wave engines. Given that the straight engine produces the smallest average SFC, and the trends in average SFC for different engine shapes are similar to the inverse of the average thrust predictions, it is concluded that the mass flow of reactants into the engines is not strongly dependent on tailpipe diameter.

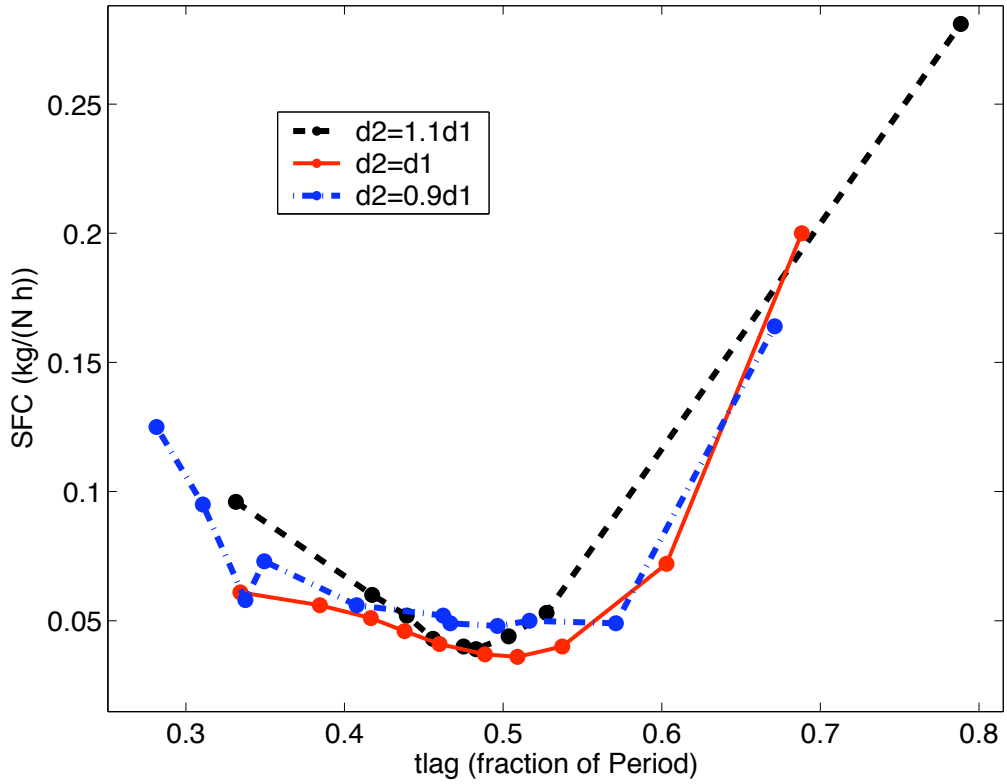

Figure 67: Average SFC vs. time lag for three engine shapes featuring different tailpipe diameters.

6.1.1 Harmonic Content of Unsteady Heat Release Rates and Wave Engine Oscillations

One primary distinction between the forced acoustic resonators presented earlier and wave engines is the method of energy addition that excited oscillations. For the acoustic resonators, forcing occurred at the boundaries at a single frequency near that of the the fundamental natural acoustic frequency of the resonator. Since the acoustic resonator was forced at a single frequency and at a relatively small amplitude, the overall properties of the driven oscillations were strongly influenced by the gas dynamic nonlinearities that transferred acoustic energy out of the driven mode and into higher harmonics. In contrast with acoustic resonators, the self-excited driving due to unsteady heat release in the wave engine is far more energetic than the small amplitude resonator forcing and is not purely sinusoidal. Therefore, the unsteady heat release effectively forces oscillations at multiple frequencies. Figure 68 presents the time dependence of heat release at one location in the combustion chamber for the maximum average thrust case of the straight engine. As shown earlier, the unsteady heat release rate is governed by the mixing processes, and the FFT of the unsteady heat release rate in Fig. 68 shows significant harmonic content. Figure 69 presents the time dependence and frequency content of the pressure oscillations in the combustion chamber for both the straight engine and the smaller tailpipe diameter engine. For the forced acoustic resonator, the presence of acoustic energy in higher harmonics was purely a function of gas dynamic nonlinearities, since the system was driven only at the fundamental natural acoustic mode frequency. On the other hand, the presence of acoustic energy in harmonics of the fundamental mode in wave engine oscillations is due to a combination of both gas dynamic nonlinearities and the direct excitation by the harmonic component of the unsteady heat release rate. As noted in the previous resonator study, engine/resonator shapes that differ from the straight duct shift the natural acoustic frequencies to non-harmonic values. Therefore, for the smaller diameter tailpipe engine, the energy of the unsteady heat release contained in the harmonics drives the system at non-resonant frequencies. As shown by the frequency sweeps in the resonator study, see Fig. 16, driving oscillations off-resonance leads to significantly lower oscillation amplitude,

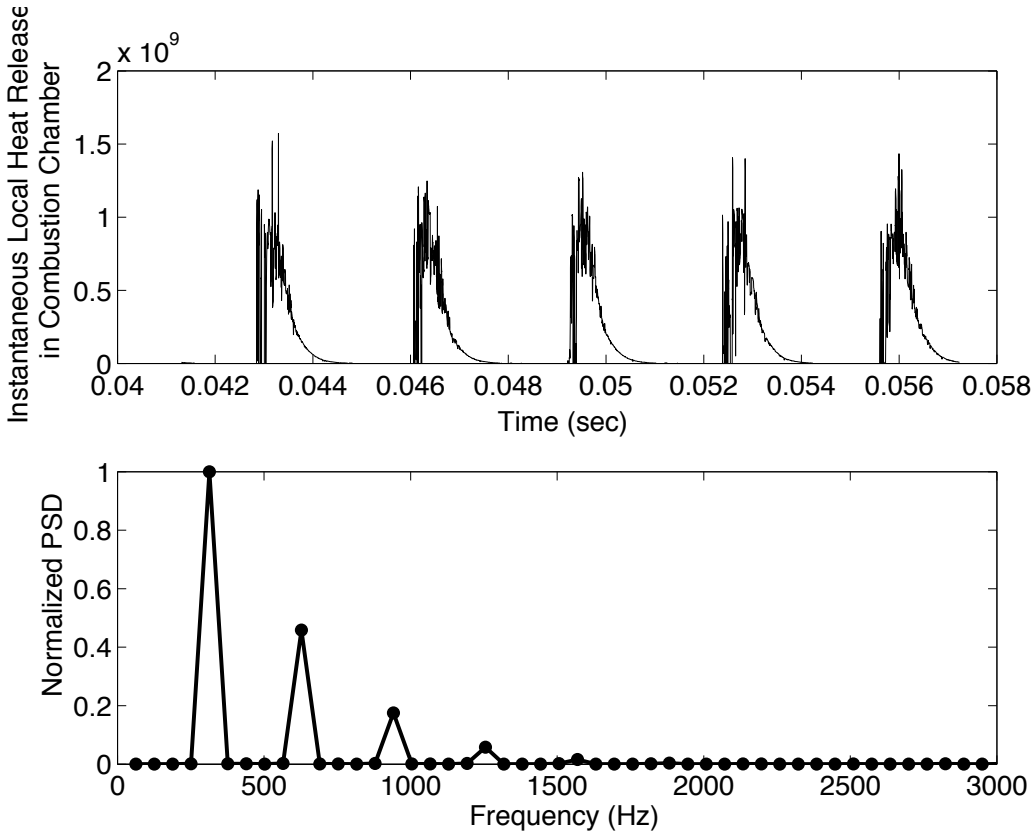

Figure 68: Time dependence of heat release and corresponding FFT at one location in combustion chamber.

and this behavior is evident in the FFT's in Fig. 69. The result is that the thrust output for the smaller diameter tailpipe engine is less than the straight duct engine because the total driving due to unsteady heat release is smaller for the smaller tailpipe diameter engine.

This observation can be clearly illustrated with a simplified model problem. This model is based on a linear, zero dimensional time dependent system that models the linear acoustic response of a wave engine. The simplifications introduced with this formulation neglect gas dynamic nonlinearities that couple the fundamental mode and harmonics with one another as well as spatial non-uniformities while still capturing the dynamics associated with the linear response of a wave engine to forcing at multiple harmonic frequencies. This model problem also assumes that the acoustic response of this simplified wave engine can

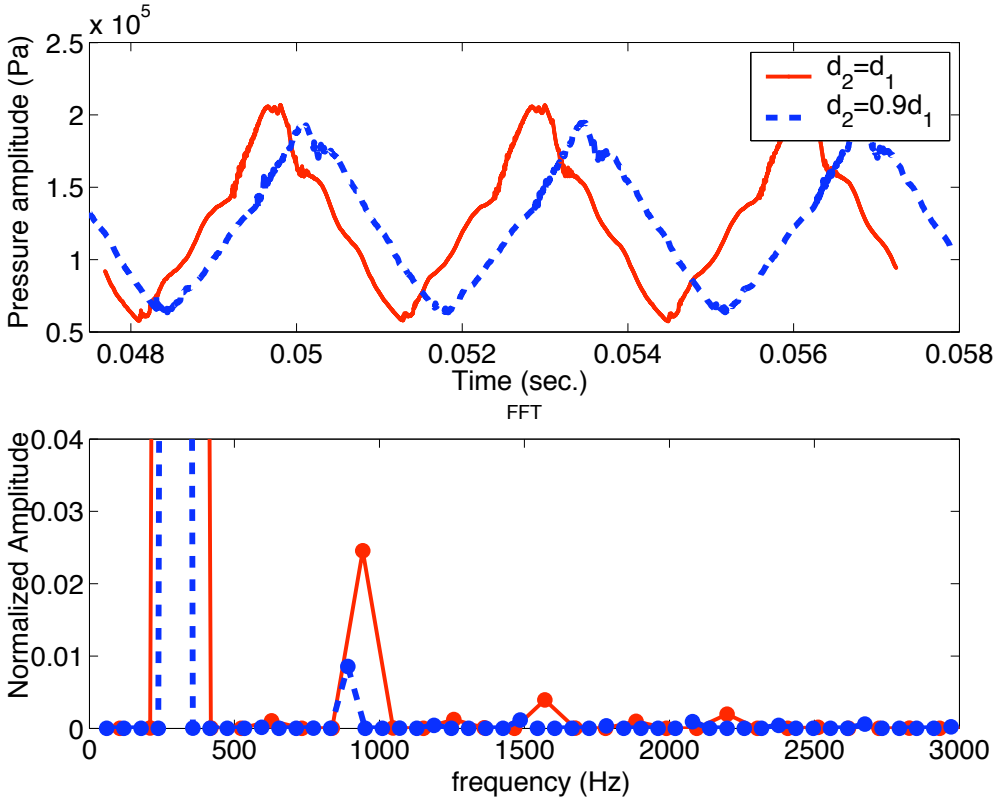

Figure 69: Time dependence of pressure and corresponding FFT at one location in the combustion for the straight duct and smaller diameter tailpipe wave engine. The FFT amplitude has been normalized by the amplitude of the fundamental natural acoustic mode, and the vertical axis is truncated in order to improve resolution of harmonic energy content.

be modeled as a system of five linear, second order time dependent ordinary differential equations of the following form:

$$\sum_{m=1}^{5} \ddot{y}_m + 2\mathfrak{l}_m(m\Upsilon_m\omega_1)\dot{y}_m + (m\Upsilon_m\omega_1)^2 y(m) = \mathfrak{K}_0 q(t), \tag{70}$$

where y_m represents the time dependent response of natural acoustic mode m oscillating a frequency $m\Upsilon_m\omega_1$. The factor Υ_m in Eq. 70 is the de-tuning factor that shifts higher modes away from integer multiples of the fundamental natural acoustic frequency ω_1. For this formulation, Υ_1 is always set to 1, and the remaining de-tuning factors determine the distribution of the other natural acoustic mode frequencies. As an example, consider an isothermal, closed, straight duct with no mean flow that contains higher acoustic modes that are all integer multiples of the fundamental. For this duct, $\Upsilon_i = 1.0$ for all modes higher than the fundamental. On the other hand, for a typical wave engine, with mean flow, temperature gradients, and variations in engine shape with axial distance, $\Upsilon_i \neq 1.0$ for i ¿ 1 because higher natural acoustic mode frequencies are not integer multiples of the fundamental. Returning to Eq. 70, $\mathfrak{l}_m \ll 1$ represents a small loss factor for each mode, and $\mathfrak{K}_0$ is a forcing factor of each natural acoustic mode. The frequency response of the system described by Eq. 70 is given by the following transfer function:

$$H(i\omega) = \sum_{m=1}^{5} \frac{\mathfrak{K}_0/(m\Upsilon_m\omega_1)^2}{[1-(\omega/m\Upsilon_m\omega_1)^2] + i(2\mathfrak{l}_m\omega/m\Upsilon_m\omega_1)}, \tag{71}$$

whose magnitude and phase are given by

$$|H(i\omega)| = \sum_{m=1}^{5} \frac{\mathfrak{K}_0/(m\Upsilon_m\omega_1)^2}{\sqrt{[1-(\omega/m\Upsilon_m\omega_1)^2]^2 + [i(2\mathfrak{l}_m\omega/m\Upsilon_m\omega_1)]^2}}, \tag{72}$$

$$\angle H(i\omega) = \sum_{m=1}^{5} \tan^{-1}\left(\frac{2\mathfrak{l}_m\omega/m\Upsilon_m\omega_1}{1-(\omega/m\Upsilon_m\omega_1)^2}\right). \tag{73}$$

The forcing function in this example was described by the following periodic log normal heat addition function that closely approximates the unsteady heat release in the previous wave engine simulations:

$$q(t) = \frac{e^{-(ln(t)^2/(2\varepsilon^2))}}{t\varepsilon\sqrt{2\pi}}, \tag{74}$$

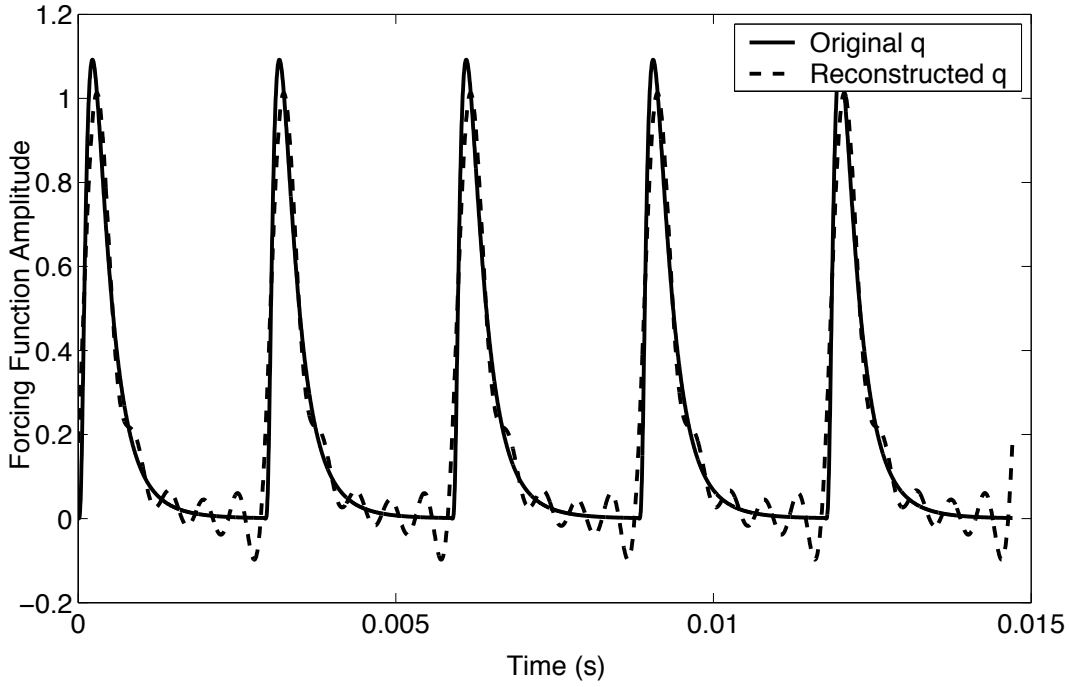

Figure 70: Comparison of the log normal energy addition function and the Fourier reconstruction of this function using five modes.

where $q(t + n/(2\pi\omega)t) = q(t)$. To compute the response of this simplified system to this forcing function, the heat addition function must be expressed in terms of a finite Fourier series. This is accomplished by taking a discrete Fourier transform of the forcing function, calculating the real magnitude and phase coefficients, and reconstructing the function with these coefficients:

$$q_{recon}(t) = \frac{1}{2}a_0 + \sum_{m=1}^{5} |Q_m| sin(m\omega(1)t + \angle(Q_m)), \tag{75}$$

Table 4 contains the coefficients for the first five modes of a log normal energy addition with fundamental frequency of 340Hz (2136 radians), and the comparison between the log normal heat addition function and the Fourier reconstruction is shown in Fig. 70.

The solution of the linear second order system represented by Eqns. 70 is the linear response of an acoustic system described by the transfer function in Eq. 71. Therefore, the output of this system is the input signal multiplied by the system transfer function, $H(i\omega)$,

Table 4: Amplitudes and phase coefficients for the Fourier reconstruction of the log normal energy addition function using five modes.

Mode	Amplitude	Phase
1	0.3022	0.6847
2	0.2130	0.0571
3	0.1500	-0.4196
4	0.1077	-0.8051
5	0.0790	-1.1296

and is given by:

$$y(t) = \frac{1}{2}a_0 H(i0) + \sum_{m=1}^{5} |Q_m||H(im\omega_1)|sin(m\omega(1)t + \angle(Q_m) + \angle(H(im\omega_1))). \qquad (76)$$

Figure 71 shows the frequency response of a harmonic and anharmonic system with fundamental frequency of 340Hz. The de-tuning factors, Υ_i, for the higher natural acoustic mode frequencies in the anharmonic system represented by Fig. 71 b) are all 1.5. In addition to the frequency response of the harmonic and anharmonic models, the vertical dashed lines represent the frequencies of forcing of the reconstructed energy addition function. The output described by Eq. 76 is presented in Fig. 72 a) and b) for the harmonic and anharmonic models described by Fig. 71. The system outputs displayed in Fig. 72 a) and b) qualitatively show that the harmonic model generates larger amplitude output. A quantitative comparison of the total output power, defined as the time integral of the square of the output signal, for the harmonic and anharmonic models shows that the total power output for the harmonic model is thirty one percent larger than the anharmonic model.

The previous example showed that an acoustic system with harmonic natural acoustic modes forced with multiple harmonic frequencies responds with a larger gain than a similar acoustic system with anharmonic natural acoustic modes. The general conclusion from this simplified model problem supports the hypothesis that the predicted decrease in average thrust for the smaller tailpipe wave engine compared with the straight engine is due to a larger mismatch between the higher harmonic components of the unsteady heat release rate and the natural acoustic modes of the engine. Similar to Fig. 69, Figure 73 compares combustion chamber pressure oscillations for the straight wave engine and the larger tailpipe

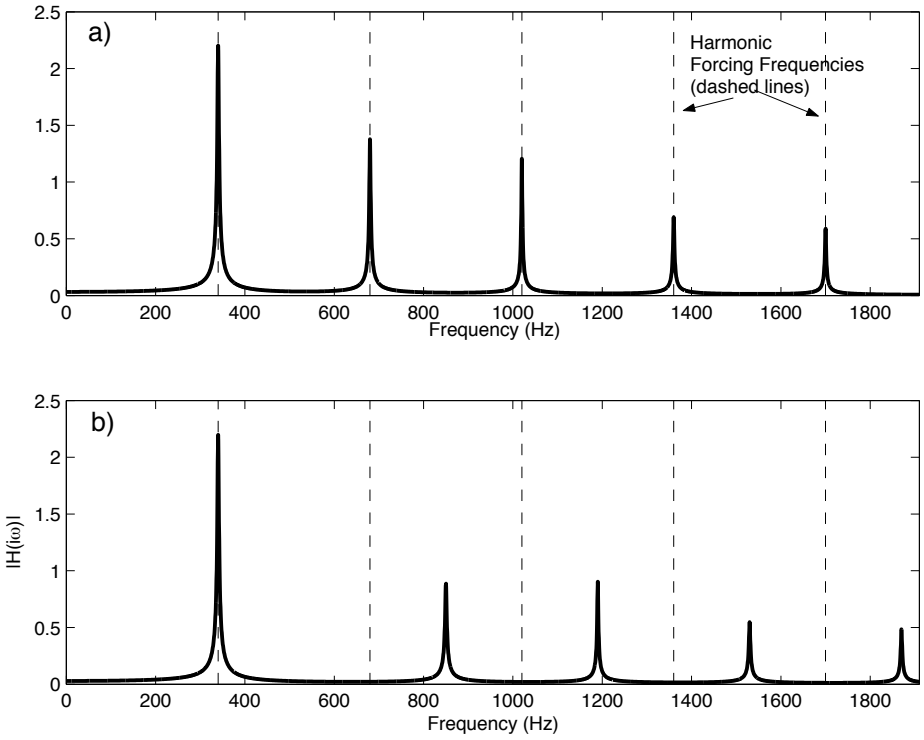

Figure 71: Frequency response of harmonic (a) and anharmonic (b) systems. De-tuning factor, Υ_m, is 1.0 for all modes of harmonic system, and 1.5 for all modes of anharmonic system

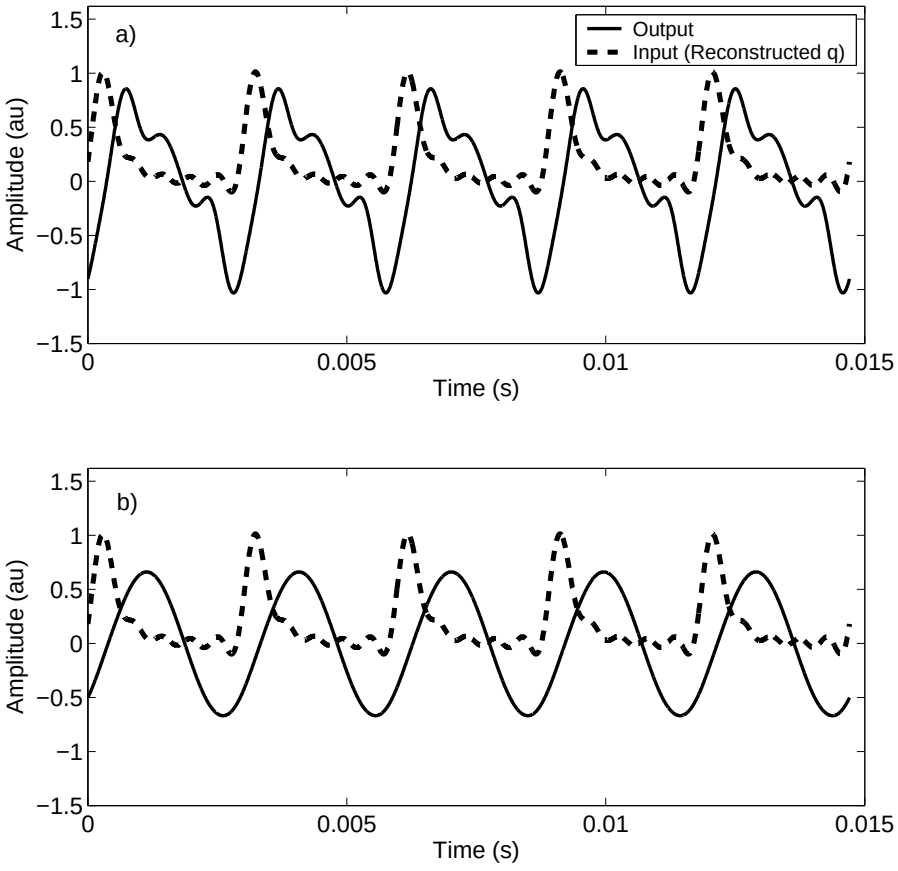

Figure 72: Time dependent output of harmonic (a) and anharmonic (b) systems.

diameter wave engine. The FFT of the combustion chamber pressure oscillations in Fig. 73 shows that the larger tailpipe diameter engine actually contains a larger portion of acoustic energy in the second harmonic than the straight duct engine, even though the predicted average thrust for the larger tailpipe diameter engine is smaller than the straight engine. According to the previous hypothesis, this result suggests that the natural acoustic mode frequencies of the larger diameter tailpipe wave engine are more closely aligned with the harmonics of the fundamental acoustic mode frequency. This clearly contradicts the previous notion that non-straight duct geometries shift natural acoustic mode frequencies away from harmonic values, but several important properties of the flow field in the wave engine were ignored in the previous analysis. The previous simplified model problem, as well as the acoustic resonator studies, considered only the influence of duct shape on natural acoustic frequencies, while ignoring the gradients of mean flow and temperature, which also influence the frequency distribution of natural acoustic frequencies in wave engines. To examine the influence of mean flow and mean temperature gradients on longitudinal natural acoustic frequencies, an eigenvalue solver for a linear one dimensional wave equation including mean flow and mean temperature variations is used. Given the extremely broad application of eigenvalue solvers ranging from pure linear algebra to quantum mechanics to acoustics and control problems, numerous eigenvalue solvers are available both in the public domain (i.e. MATLAB, FEMLAB, LAPACK, etc.) and the literature. For this wave engine application, a simple sectored representation of the wave engine is used, and acoustic matching conditions are applied between sectors.

To show the influence of mean flow and mean temperature gradients, the real part of the first four eigenvalues, representing the first four natural acoustic mode frequencies of the sectored wave engine with a constant, 2100K mean temperature field, are presented in Table 5 for the three wave engine geometries. The zero mean flow values in Table 5 show that the straight engine indeed does have higher mode frequencies which are integer multiples of the fundamental. Further, the natural acoustic frequencies for the mean flow cases show only minor deviations from the zero mean flow cases, and this occurs because although the unsteady velocities in this wave engine can be quite large, the mean flow through the engine

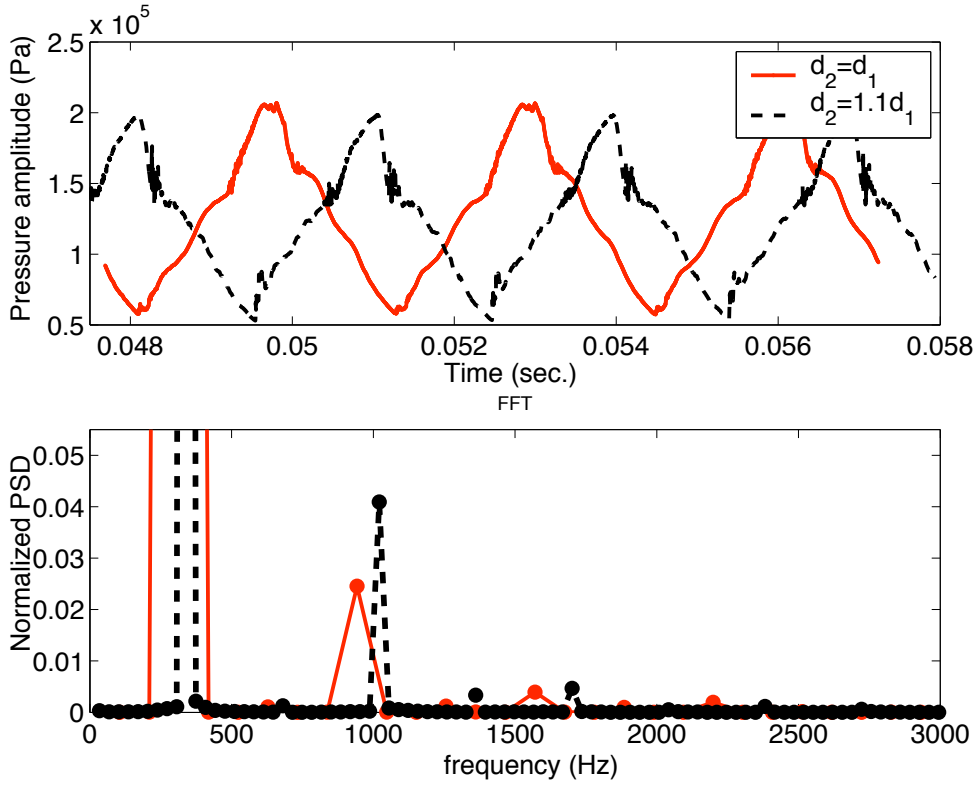

Figure 73: Time dependence of pressure and corresponding FFT at one location in the combustion for the straight duct and larger diameter tailpipe wave engine. The FFT amplitude has been normalized by the amplitude of the fundamental natural acoustic mode, and the vertical axis is truncated in order to improve resolution of harmonic energy content.

Table 5: Natural acoustic mode frequencies for the investigated wave engines with spatially uniform mean temperature of 2100K.

	$d_2 = 0.9d_1$	$d_2 = 0.9d_1$	$d_2 = d_1$	$d_2 = d_1$	$d_2 = 1.1d_1$	$d_2 = 1.1d_1$
Mode #	$\dot{m} = 0$	$\dot{m} = 20g/s$	$\dot{m} = 0$	$\dot{m} = 20g/s$	$\dot{m} = 0$	$\dot{m} = 20g/s$
1	422.1	421.9	449.1	449.0	473.2	473.2
2	1356.0	1355.5	1347.4	1347.0	1342.0	1341.7
3	2253.4	2252.6	2245.6	2245.0	2237.8	2237.3
4	3140.1	3138.5	3143.8	3143.0	3148.0	3147.3

is relatively small for these operating conditions.

Figure 74 shows a sectored representation of a wave engine with a typical mean temperature distribution where red represents higher temperatures (2100K) and blue lower ($\tilde{4}$00K). The temperature distribution shown in Figure 74 follows the predicted mean temperature field shown in Fig. 75 for the three wave engines. Figure 75 shows lower mean temperatures near the inlet and exhaust planes, due to the injection of cold reactants at the inlet and the influence of backflow.

Table 6 shows the natural acoustic frequencies for the same engine shapes as Table 5, but with the mean temperature gradient shown in Fig. 74. In contrast with the previous results computed for a spatially uniform mean temperature field, Table 6 shows that a non-uniform mean temperature gradient significantly shifts the natural acoustic mode frequencies away from harmonic values of the fundamental. In addition, the shift in natural acoustic frequencies from harmonics of the fundamental varies considerably depending on the engine shape. Not only are the higher mode natural acoustic frequencies for the straight duct engine no longer integer multiples of the fundamental, Table 7 also shows that the frequency shift of the higher modes from harmonic values is smaller for the larger diameter tailpipe engine than for the straight duct. This observation explains why the larger diameter tailpipe engine contains more acoustic energy in higher harmonics than the straight engine.

One final issue requires resolution: If the natural acoustic mode frequencies of the larger diameter tailpipe engine are more closely aligned with the harmonics of the unsteady heat release rate, why is the thrust output larger for the straight duct engine? The resolution of this apparent inconsistency is not contained in the analysis of the unsteady heat release in

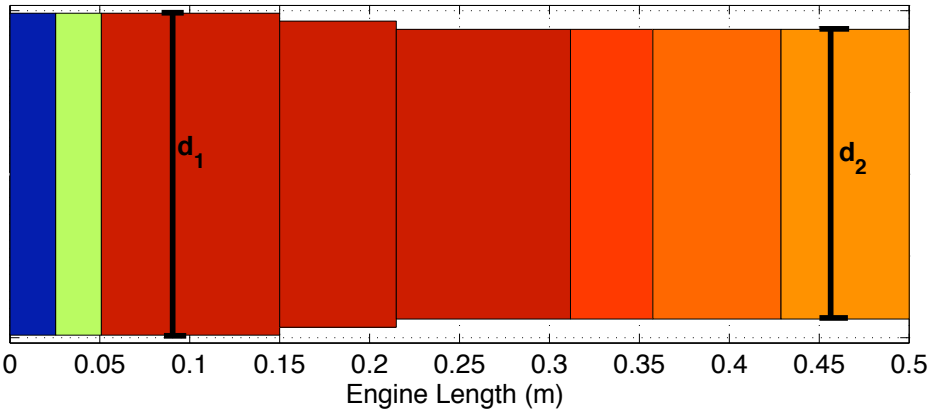

Figure 74: Sectored representation of wave engine. Axial temperature gradients represented by colored sectors; red - hot ($\tilde{2}$000K) through blue - cold($\tilde{3}$00K).

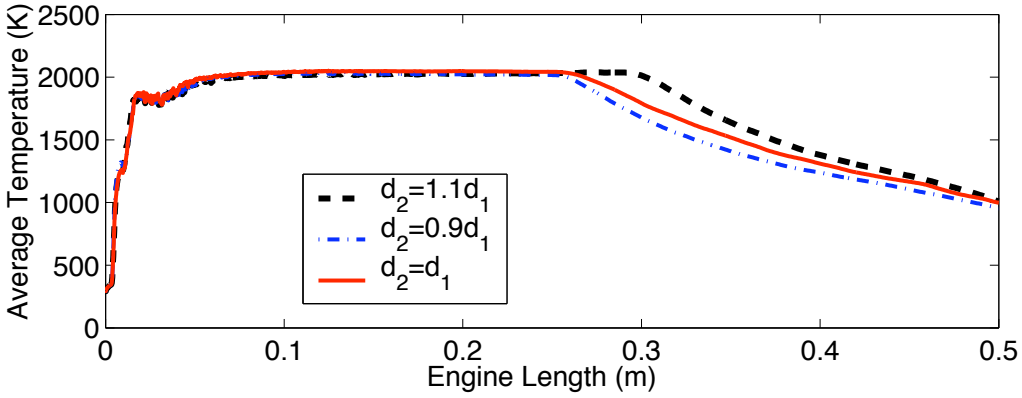

Figure 75: Axial mean temperature profile for three engine shapes.

Table 6: Natural acoustic mode frequencies for the investigated engine geometries with a mean flow of 20 g/s and a non-uniform mean temperature field.

Mode #	$d_2 = 0.9d_1$	$d_2 = d_1$	$d_2 = 1.1d_1$
1	321.9	348.9	366.7
2	1117.0	1088.2	1080.6
3	1908.9	1920.0	1936.7
4	2786.7	2780.5	2805.7

Table 7: Shift of natural acoustic mode frequencies away from harmonics of fundamental corresponding to values in Table 6.

Freq. Shift	$d_2 = 0.9d_1$	$d_2 = d_1$	$d_2 = 1.1d_1$
$\lvert f_2 - 3f_1 \rvert$	151.3	41.46	19.5
$\lvert f_3 - 5f_1 \rvert$	299.4	175.5	103.2
$\lvert f_4 - 7f_1 \rvert$	533.4	337.7	238.8

the combustion chamber, but rather in an analysis of the influence of engine shape on the cross-sectional area of the exhaust plane. Equation 66 showed that the thrust generated by the positive exhaust flow is linearly proportional to the exhaust plane area and quadratically proportional to the exhaust velocity. Additionally, the conservation of mass dictates that area and velocity are inversely proportional for the same density. Therefore, increasing the area at the exhaust decreases the velocity, as shown in Fig. 76. This results in an overall decrease in the total thrust output since thrust depends more strongly on velocity than area. In conclusion, although the driving of oscillations is slightly more effective for the larger diameter tailpipe engine than the straight engine, the average thrust generated for the larger diameter tailpipe engine is lower due to the increased cross sectional area at the exhaust plane.

6.2 Exhaust Nozzle/Flare Study

For steady thrust producing devices like rocket motors and jet engines, it is clear that the addition of an exhaust nozzle can improve thrust performance by increasing the total kinetic energy of the exhaust flow. For unsteady thrust producing devices, the impact of an exhaust nozzle or flare on overall performance is not clear due to the additional influence

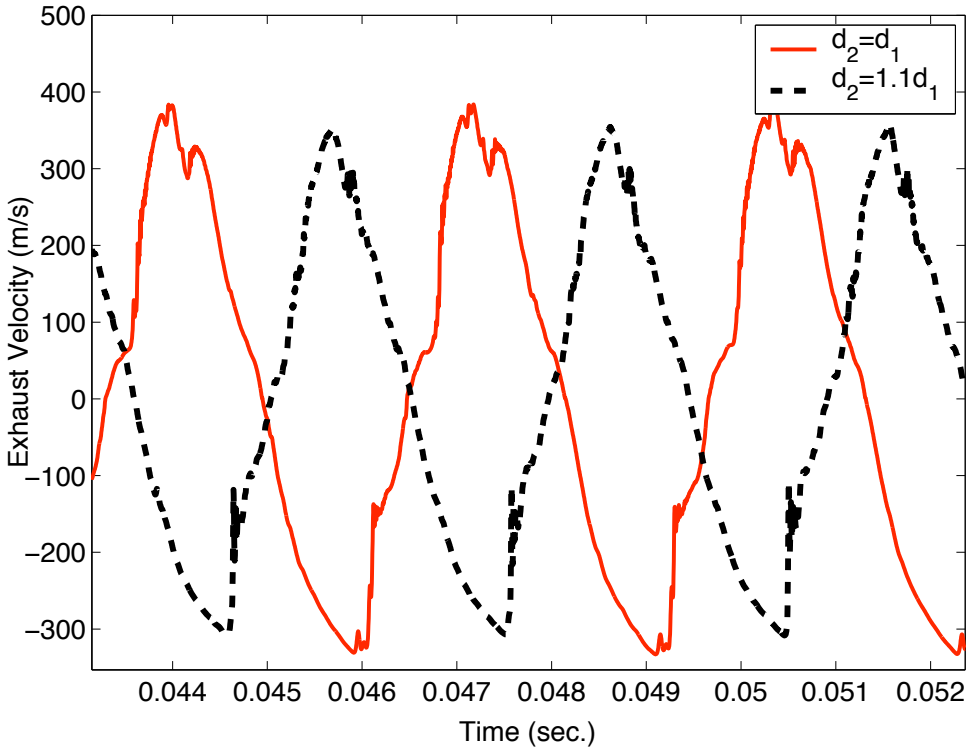

Figure 76: Exhaust velocity vs. time for straight engine and larger tailpipe diameter engine.

of a nozzle or flare on the acoustic characteristics of the engine. Therefore, the influence of a nozzle and a tail flare on overall performance was examined for a stationary wave engine with a fully subsonic flow field (to avoid choking the flow which would dramatically alter the acoustic boundary conditions). To investigate the influence of a nozzle and a flare, a straight duct wave engine with the addition of a 0.1m extension of three different shapes shown in Fig. 77 was used. The extension on engine A) is a linear flare with a total increase in cross sectional area of 40%, engine B) is a straight extension, and the extension on engine C) is a linear nozzle with a total decrease in cross sectional area of 40%. Additionally, for all simulations performed in this portion of the investigation, the inflow resistance parameter is 550 and the backflow temperature is 650K. The same mixing characteristics are used for all simulations, with the rms velocity set to twenty percent of the maximum inlet velocity and the size of small scale events set to ten percent of the large scale event size, or thirty five percent of the combustion chamber diameter.

Figure 78 shows the average thrust as a function of the time lag between the start of injection and the start of large and small scale mixing for engines A), B), and C). Once again, the straight duct engine produces the largest average thrust. The linear flare engine, engine A), produces only slightly more than 65% of the thrust of the straight engine, and engine C) produces around 30% of the thrust of the straight engine. Figure 78 also shows the average thrust values for engine C) changes very little with time lag, suggesting that this engine is not operating at any resonance. Figure 79 shows that the dependence of average SFC on time lag is qualitatively similar to the inverse of the average thrust. It should be pointed out that there is the possibility that certain other assumptions about operating characteristics of the engine are no longer accurate enough to form quantitative conclusions on the influence of nozzles and flares for subsonic, unchoked wave engines. For example, results in the previous section showed that for relatively small changes in tailpipe diameter significantly alter the acoustic characteristics of the engine, thus waveforms and operating frequencies vary considerably for different engine shapes. When conditions such as operating frequency change considerably, the assumption that mixing characteristics of the reactant injection remain constant may be incorrect. The formulation of the mixing model in this investigation

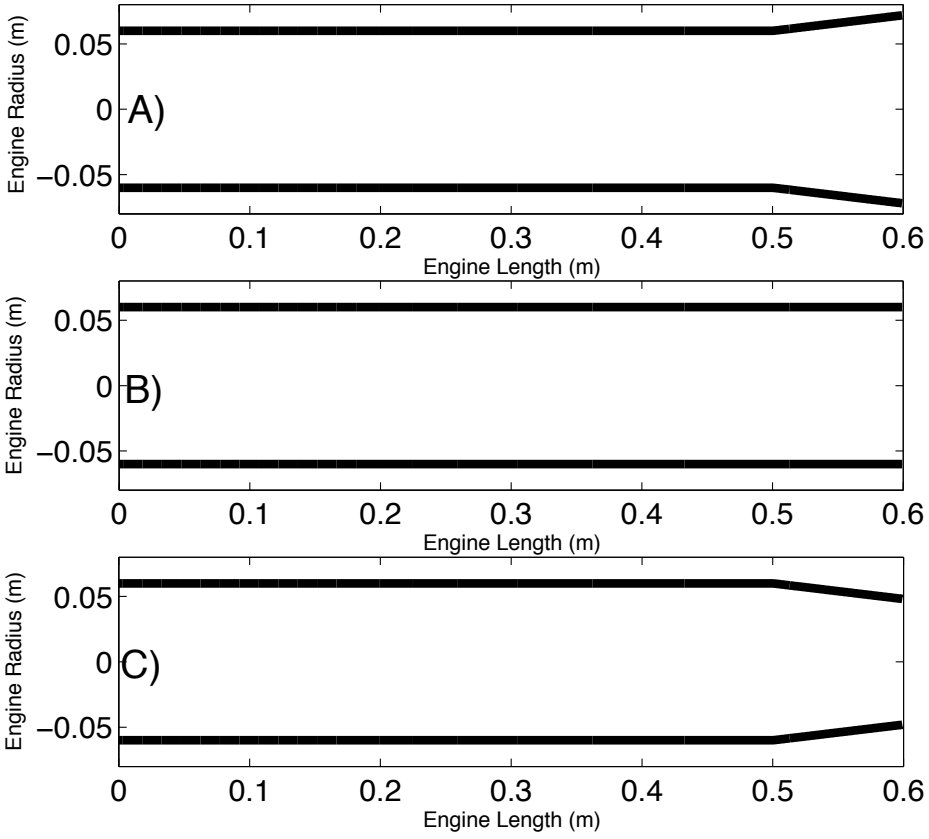

Figure 77: Engine shape with metric dimensions for exhaust nozzle and flare investigation.

does not explicitly account for the influence of changes in operating conditions on mixing characteristics, therefore additional information about the mixing processes is necessary to accurately model significantly different engine geometries. The results presented in Figs. 78 and 79 provide an example of the limits of this modeling technique rather than a quantitative assessment of wave engine performance, but one important conclusion is apparent from these results. Design considerations that appear attractive for nearly steady flow systems must be thoughtfully considered before applying them to unsteady wave engine designs. The addition of a nozzle to increase mean exhaust velocity as a means of increasing thrust is logical from a steady flow perspective, yet the influence of a nozzle on the acoustic characteristics of the wave engine may negate any performance benefits from increasing exhaust velocities.

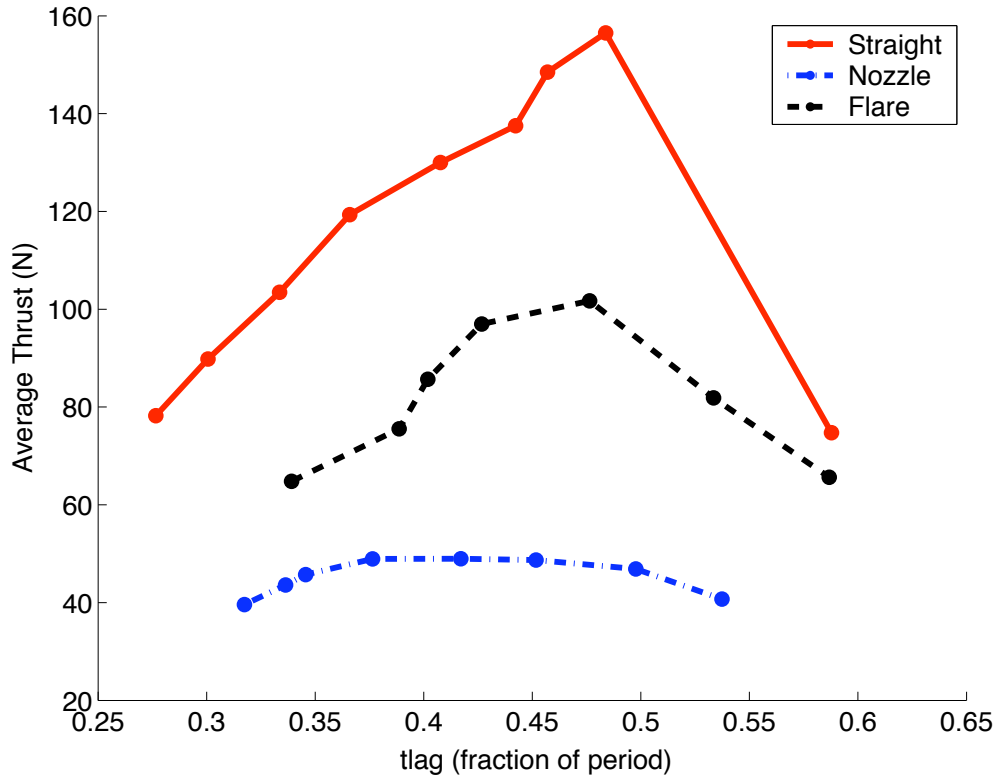

Figure 78: Dependence of average thrust of the wave engines upon the time lag for three engine shapes featuring a linear flare, straight extension, and linear nozzle shown in Fig. 77.

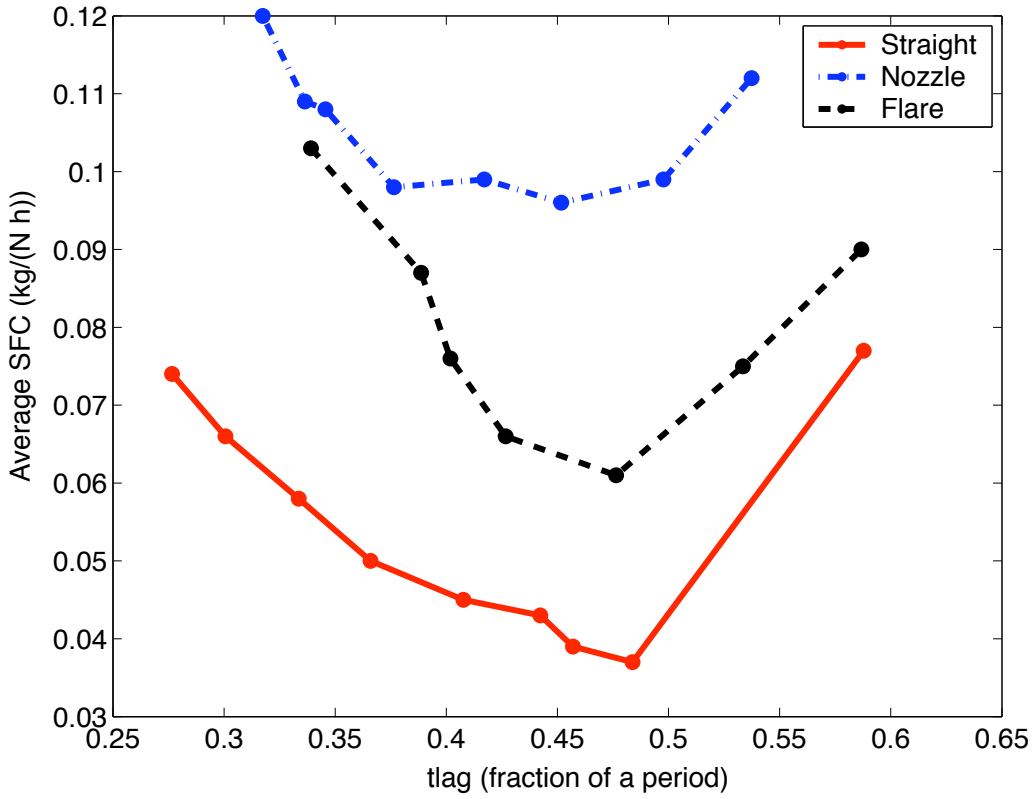

Figure 79: Dependence of average SFC of the wave engines upon the time lag for three engine shapes featuring a linear flare, straight extension, and linear nozzle shown in Fig. 77.

CHAPTER VII

CONCLUSIONS AND RECOMMENDATIONS FOR FUTURE STUDIES

7.1 Conclusions

The primary objective of this thesis was to determine how specific characteristics of unsteady heat release and engine shape influence overall wave engine performance. In general, the results of the parametric wave engine simulations in this investigation have shown that the relationship between unsteady heat release rates and the characteristics of the natural acoustic modes and frequencies of a wave engine significantly influence overall engine performance. These results suggest that portions of the wave engine design process involving these physical processes, such as inlet/valve design and engine shape, should account for the details of this relationship. More specifically, results from this investigation showed that a degradation in overall wave engine performance results from large differences between the natural acoustic mode frequencies of the engine and the frequency content of the unsteady heat release driving oscillations in the engine.

The first investigation, concentrating on a simplified physical system, modeled finite amplitude driven oscillations in acoustic resonators. This investigation assumed single frequency forcing at the closed ends of shaped acoustic resonators, thus eliminating mean flow, mean temperature gradients, and excitation by heat release. The Galerkin method was applied to a quasi one-dimensional nonlinear wave equation to model driven oscillations in various shaped acoustic resonators. The results from the application of the Galerkin method to this model problem concluded that resonator shape influences the characteristics of driven oscillations by shifting natural acoustic mode frequencies away from harmonics of the fundamental. Specifically, the shift in natural acoustic mode frequencies away from harmonics of the driven frequency decreases the transfer of acoustic energy from the driven frequency

resulting from gas dynamic nonlinearities. While results from previous experimental and numerical studies have supported this conclusion, results obtained in this investigation for a exponential horn resonators quantified the influence of shifting individual natural acoustic frequencies on driven oscillation properties. This investigation also parametrically examined the influence of the flare constant on compression ratio and showed that the maximum compression ratio occurs for a normalized flare constant of 5.75.

While Galerkin method techniques have distinct advantages, such as rapid turnaround simulation time and the inherent ability to reveal physical insight into nonlinear oscillations, the solution approach is not well-suited for wave engine simulations that include more complex boundary conditions and the physical processes not present in acoustic compression devices. Therefore, an alternate modeling approach based on the explicit finite differencing of the quasi one-dimensional conservation equations was developed. Additionally, this model includes the ability to realistically simulate flapper valve behavior as well as unsteady mixing processes between injected reactants and combustion products from previous cycles. The advantage of this formulation is that given the quasi one-dimensional assumption along with the ability to model both mixing processes and large amplitude wave propagation, this model is capable of performing parametric studies over a wide range of operating conditions without requiring prohibitively large computational time.

The parametric studies concerning mixing and unsteady heat release rates had two objectives. The first objective involved assessing the sensitivity of wave engine performance to the mixing model parameters. Since no experimental data on the mixing characteristics of wave engines was found, this application of the LEM model could not be calibrated. Therefore, it was necessary to show how inaccurate assumptions about the mixing processes would influence the prediction of overall wave engine performance. For example, results from a parametric study of the size of large scale mixing events show that a factor of three difference in large scale event size results in only a ten percent difference in maximum average thrust. Additionally, results from the parametric study of the size of small scale mixing events conclude that as long as the small scale eddy size is not unrealistically large, small scale eddy size does not have a large impact on the predicted overall performance.

The second objective of the parametric studies concerning mixing and unsteady heat release rates was to determine the influence of the characteristics of unsteady heat release rates on wave engine performance. Results from the parametric study of small scale mixing intensity predicted that more intense small scale mixing leads to a more rapid rise in heat release after the start of injection(i.e. faster burning). A comparison of the predicted average thrust for different turbulent mixing intensities showed that the largest average thrust occurred for a turbulent rms velocity of 30% of the maximum inlet velocity, and that increasing the turbulent mixing intensity to a turbulent rms velocity of 50% of the maximum inlet velocity actually decreases the maximum thrust generation. Additionally, these parametric simulations predicted that the average thrust decreases more rapidly as the time lag between the start of injection and the start of mixing is decreased from the optimal time lag for more intense turbulent mixing. Hence, decreasing the turbulent rms velocity from 30% of the maximum inlet velocity to 10% leads to a lower maximum average thrust, but the average thrust for the 10% case is greater than the 30% case for time lags away from the optimal time lag. From a design perspective, this conclusion identifies a trade-off between maximum average thrust and a larger operating regime in terms of the timing of mixing events.

Based on the results presented in the preliminary investigation involving acoustic resonators, it was hypothesized that shaped wave engines would generate more thrust than straight wave engines due to the fact that engine shaping would suppress energy transfer out of the fundamental, driven acoustic mode by gas dynamic nonlinearities. On the contrary, results from the parametric studies of engine tailpipe diameter predicted a larger average thrust and a lower SFC for the straight duct engine than either the smaller or larger tailpipe diameter wave engines. Further analysis of these results showed that physical processes in addition to gas dynamic nonlinearities significantly influence overall engine performance. The first part of this analysis recognized one important difference between the energy addition in the wave engine and the acoustic compressor. The acoustic resonator forced oscillations at one frequency while the frequency content of the heat release rate in the wave engine contained significant harmonic content due to the impulsive injection of

reactants and the characteristics of mixing between the reactants and combustion products from previous cycles. Results from the acoustic resonator study showed that in the absence of mean flow and mean temperature gradients, the higher natural acoustic mode frequencies are harmonics of the fundamental for straight ducts and anharmonic for shaped ducts. Additionally, it was shown that while the mean flow rates for the wave engines examined in this study had minimal effect on the natural acoustic mode frequencies, the mean temperature gradient, created by heat release, the injection of cold reactants, and the backflow of cooler air from the exhaust significantly shifted natural acoustic mode frequencies away from harmonics of the fundamental. Hence, the fraction of energy contained in the harmonics of the heat release rate excite much lower amplitude acoustic oscillations due to off-resonance conditions, resulting in a dramatic decrease in driving effectiveness. The overall result of this mismatch between the frequency content of the heat release rate and the natural acoustic mode frequencies of the wave engine is a significant decrease in the predicted maximum average thrust. This conclusion suggests that inlet configurations, such as flapper valve design, which strongly influence mixing characteristics and therefore unsteady heat release rates, and engine shape, should be designed concurrently in order to maximize overall performance.

7.2 Recommendations for Future Studies

The absence of detailed experimental measurements of wave engine flow fields precluded a detailed validation case of model predictions. Furthermore, given the number of model assumptions included in order to create a tool capable of parametric studies, this investigation provides only a first step towards a useful analysis of wave engines. The following recommendations concentrate on the considerable improvements to the modeling tool necessary to gain more confidence in simulation results as well as possible direction of future studies aimed at developing a more thorough understanding of wave engine processes.

7.2.1 Model Improvements

Ideally, highly resolved experimental data on the formation of large coherent structures formed during the impulsive injection of reactants into the chamber are necessary to validate

the LEM model applied in wave engine simulations. Unfortunately, this data does not exist for the wave engines examined in this study, so one other possibility is that data from detailed two dimensional large eddy simulations (LES) be used as an alternative. The ability of LES to capture unsteady behavior such as vortex formation makes it an attractive choice. Given the moderate Reynolds numbers associated with this problem and the small overall simulation time (1 Period $\sim$ 1/100th sec.), parallel LES simulations could provide a reasonable means of obtaining useful data. Results based on data obtained from higher dimensional simulations will also aid in the refinement of the large scale mixing event model. Currently, given the lack of information regarding the specifics of large vortex formation, large scale events occur instantaneously in the region of the interface between reactants and products. While for smaller eddies with much smaller characteristic turnover times this idealization may be adequate, the validity for coherent structures on the order of the integral scale is questionable and should be examined.

In addition to improvements to the mixing model, more realistic boundary conditions could also increase the accuracy of the model significantly. As shown in the heat release validation study, boundary conditions play a crucial role in determining the acoustic properties of the wave engine. Therefore, a more physically accurate treatment of wave reflections, possibly through the use of impedance boundary conditions, could allow the inclusion of effects such as phase shifting and damping in a more physically realistic manner. Additionally, for this investigation, flapper valves responded instantaneously, when in reality a finite time is associated with the opening and closing of valves. While this study modeled the boundaries in a consistent and somewhat ideal manner, finite valve opening times and a more realistic acoustic loss model at the exhaust could have an important influence on overall performance.

Results presented in this investigation focused primarily on sea level static conditions, essentially to provide a baseline set of results and conclusions. Given the one dimensionality of this modeling tool, the incorporation of inlet and exhaust boundary conditions to account for specific flight conditions would not be difficult, and the wave engines could be simulated in conditions from stationary up to nearly sonic flight speeds and a wide range

of altitudes. Furthermore, literature on combustion instabilities found in jet engine augmentors clearly shows that flight conditions have a profound influence on the nature of instabilities. Hence, the opportunity and possible benefits of investigating the influence of different flight conditions on wave engine performance are clear.

Results from this study suggest that the most significant direction for future research lies in a more detailed investigation into unsteady heat release rate tailoring for given engine designs. This investigation concentrated on a generic two length scale mixing process that resulted in unsteady heat release rates that contained harmonic frequencies of the driven mode. The determination of the characteristics of mixing that could be used to control the frequency content of the unsteady heat release rate would be very valuable in the design of future wave engines. Similarly, the same approach could also be used to determine engine characteristics that control the natural acoustic modes and frequencies for a given wave engine design. For example, it was shown that the mean temperature profile significantly influences natural acoustic mode frequencies, so it is possible that the addition of cooling air or the design of the engine exhaust could be used to tailor the mean temperature profile of the engine, thus providing some level of control over the natural acoustic frequencies of the engine.

One important assumption in the analysis of the wave engine behavior presented in this investigation is that the unsteady heat release has no effect on the natural acoustic frequencies and the stability characteristics of the engine. In general this is not a valid assumption, due to the fact that unsteady heat release, especially of the magnitude that occur in normal wave engine operation, can alter the stability of individual eigenmodes of an engine. The influence of unsteady heat release rates can be included in the analysis, although the calculation of eigenmodes and natural acoustic frequencies becomes somewhat more difficult.

Finally, this investigation did not account for changes in the aerodynamic characteristics resulting from engine shape changes. This is not an important consideration for static conditions or if the wave engine is contained within a larger airframe, such as a cruise missile. Yet, if the wave engine is wing mounted, possibly on a UAV, engine characteristics

like frontal area can contribute to overall aircraft drag. An addition to this model that incorporates the influence of engine shape on aerodynamic characteristics could provide one more design constraint that must be considered to more accurately optimize future wave engine designs.

REFERENCES

[1] "Project squid conference on wave engines and pulsejets," tech. rep., Office of Naval Research, Princeton University, Nov 1954.

[2] Anderson, D., Tannehill, J., and Pletcher, R., *Computational Fluid Mechanics and Heat Transfer*. New York: Hemisphere Publishing, 1984.

[3] Arunajatesan, S. and Menon, S., "An engineering model for designing compact toxic waste incinerators," *Combustion, Science and Technology*, vol. 139, pp. 293–328, 1998.

[4] Benelli, G., De Michele, G., Cossalter, V., Da Lio, M., and Rossi, G., "Simulation of large non-linear thermo-acoustic vibrations in a pulsating combustor," *Proceedings of the 24th Symposium (International) on Combustion*, pp. 1307–1313, 1992.

[5] Bertin, J., Paris, F., and LeFoll, J., "The snecma escopette pulse-jet," *Inter Avia*, vol. 8, no. 6, pp. 343–347, 1953.

[6] Bertin, J., "United states patent number 2834183," 1958.

[7] Burnley, V. and Culick, F., "On the energy transfer between transverse acoustic modes in a cylindrical combustion chamber," *Combustion Science and Technology*, 1999.

[8] Chester, W., "Resonant oscillations in closed tubes," *Journal of Fluid Mechanics*, vol. 18, pp. 44–64, 1964.

[9] Chun, Y. and Kim, Y., "Numerical analysis for nonlinear resonant oscillations of gas in axisymmetric closed tubes," *Journal of the Acoustical Society of America*, vol. 108, pp. 2765–2774, 2000.

[10] Clayton, R., Rogero, R., and Sotter, J., "An experimental description of destructive liquid rocket resonant combustion," *AIAA Journal*, vol. 6, no. 7, pp. 1252–1259, 1968.

[11] Cruikshank, D., "Experimental investigation of finite-amplitude acoustic oscillations in a closed tube," *Journal of the Acoustical Society of America*, vol. 52, pp. 1024–1036, 1972.

[12] Culick, F., "Some recent results for nonlinear acoustics in combustion chambers," *AIAA Journal*, vol. 32, pp. 146–169, 1994.

[13] Edelman, L., "The pulsating jet engine - its evolution and prospects," *SAE Quarterly Transactions*, vol. 1, no. 2, 1947.

[14] Finlayson, B., *The Method of Weighted Residuals and Variational Principles*. New York: Academic Press, 1972.

[15] Foa, J. V., *Elements of Flight Propulsion*. New York: John Wiley and Sons, 1960.

[16] Gharib, M., Rambod, E., and Shariff, K., "A universal time scale for vortex ring formation," *Journal of Fluid Mechanics*, vol. 360, 1998.

[17] Glezer, A. and Coles, D., "An experimental study of a turbulent vortex ring," *Journal of Fluid Mechanics*, vol. 211, 1990.

[18] Gosslau, F., "Development of the v-1 pulsejet," *AGARDograph*, no. 2, pp. 400–418, 1957.

[19] Hamilton, M., Ilinski, Y., and Zabolotskaya, E., "Linear and nonlinear frequency shifts in acoustical resonators with varying cross sections," *Journal of the Acoustical Society of America*, vol. 110, no. 1, 2001.

[20] Heywood, J., *Internal Combustion Engine Fundamentals*. New York: McGraw Hill, 1988.

[21] Il'inskii, Y., Lipkens, B., Lucas, T., Van Doren, T., and Zabolotskaya, E., "Non-linear standing waves in an acoustical resonator," *J. Acoust. Soc. of Am.*, vol. 104, 1998.

[22] Kailasanath, K., Gardner, J., Oran, E., and Boris, J., "Numerical simulations of unsteady reactive flows in a combustion chamber," *Combustion and Flame*, vol. 86, 1991.

[23] Kee, R., Miller, J., and Jefferson, T., "Chemkin: A general-purpose, problem independent, transportable, fortran chemical kinetics code package," Tech. Rep. SAND80-8003, Sandia Nat. Lab., 1980.

[24] Keller, J. and Barr, P., "Premixed combustion in an oscillating/resonant flowfield. an investigation of the fine-scale velocity fluctuations," *Proceedings of the International Symposium on Pulsating Combustion*, 1991.

[25] Keller, J., Barr, P., and Bramlette, T., "Pulse combustion: Demonstration of the characteristic mixing time in a commercial burner," *Combustion, Science and Technology*, vol. 66, pp. 127–137, 1989.

[26] Keller, J., Eibeck, P., Bramlette, T., and Barr, P., "Pulse combustion: Tail pipe exit jet characteristics," *Proceedings of Int'l Symposium on Pulsating Combustion*, Aug 1991.

[27] Kentfield, J., Rehman, A., and Cronje, J., "Performance of pressure-gain combustors without moving parts," *Journal of Energy*, vol. 4, no. 2, 1980.

[28] Kerstein, A., "A linear eddy model of turbulent scalar transport and mixing.," *Combustion Science and Technology*, vol. 60, pp. 391–421, 1988.

[29] Kerstein, A. R., "Linear-eddy modeling of turbulent transport. part 4. structure of diffusion-flames," *Combustion Science and Technology*, vol. 81, pp. 75–86, 1992.

[30] Kinsler, L., Frey, A., Coppens, A., and Sanders, J., *Fundamentals of Acoustics*. John Wiley and Sons, 1982.

[31] Lawrenson, C., Lipkins, B., Lucas, T., Perkins, D., and Van Doren, W., "Measurements of macrosonic standing waves in oscillating closed cavities," *Journal of the Acoustical Soceity of America*, vol. 104, pp. 623–636, 1998.

[32] Lockwood, R., "United states patent number 3206926," 1965.

[33] Lockwood, R., Bennett, E., and Graber, D., "United states patent number 3462955," 1969.

[34] Logan, J., "Valveless pulsejet investigations part i: Tests of small scale models," *Technical Memorandum No. CAL-27 [Project Squid]*, May 1949.

[35] Lucas, T., "United states patent number 5,319,938," 1994.

[36] Maxworthy, T., "Turbulent vortex rings," *Journal of Fluid Mechanics*, vol. 64, 1974.

[37] Menon, S., McMurty, P., Kerstein, A., and Chen, J.-Y., "Prediction of nox production in a turbulent hydrogen-air jet flame," *Journal of Propulsion and Power*, vol. 10, Mar-Apr 1994.

[38] Nalim, M. and Paxson, D., "A numerical investigation of premixed combustion in wave rotors," *Journal of Engineering for Gas Turbines and Power*, vol. 119, pp. 668–675, July 1997.

[39] Oppenheim, A., "Research and development of impulsive ducts in germany," tech. rep., British Intelligence Objectives Sub-Committee, 1949.

[40] Packzo, G., Lefdal, P., and Peters, N., "Reduced reaction schemes for methane, methanol and propane flames," *Proceedings of the 21st Symposium (International) on Combustion*, pp. 739–48, 1986.

[41] Poinsot, T. and Lele, S., "Boundary conditions for direct simulations of compressible viscous flows," *Journal of Computational Physics*, vol. 101, pp. 104–129, 1992.

[42] Poinsot, T., Trouve, A., Veynante, D., Candel, S., and Esposito, E., "Vortex-driven acoustically coupled combustion instabilities," *Journal of Fluid Mechanics*, vol. 177, pp. 265–292, 1987.

[43] Rayleigh, J., "The explanation of certain acoustical phenomena," *Nature*, vol. 18, pp. 319–321, 1878.

[44] Reynst, F., *PulsatingCombustion: The Collected Works of F.H. Reynst.* Pergamom Press, 1961.

[45] Sankaran, V. and Menon, S., "Structure of premixed turbulent flames in thin-reaction-zones regime," *Proceedings of the Combustion Institute*, vol. 28, pp. 203–209, 2000.

[46] Schmidt, P., "German patent number 523655," 1930.

[47] Shultz-Grunow, F., "Gas dynamic investigations of the pulse jet tube," Technical Memorandum 1181, National Advisory Committee Aeronautics, 1947.

[48] Smith, T. and Menon, S., "Model simulations of freely propagating turbulent premixed flames," *Proceedings of the 26th Symposium (International) on Combustion*, pp. 299–306, 1996.

[49] White, F., *Viscous Fluid Flow*. McGraw-Hill, 2nd ed., 1991.

[50] Yu, K., Trouve, A., and Daily, J., "Low-frequency pressure oscillations in a model ramjet combustor," *Journal of Fluid Mechanics*, vol. 232, pp. 47–72, 1991.

[51] Zinn, B. and Powell, E., "Nonlinear combustion instability in liquid propellant rocket engines," *Proceedings of the 13th International Symposium on Combustion*, pp. 491–503, 1971.

VITA

Robert Rudolph Erickson was born in Morristown, New Jersey on December 23, 1976, the youngest son of Richard and Cynthia Erickson. In 1998, he received his BE in mechanical engineering from Vanderbilt University located in Nashville, TN. He entered the aerospace engineering graduate studies program at the Georgia Institute of Technology in Fall 1998 and received his Master of Science degree in 2001.